Chair of Mechanics

Doctoral Thesis

Thermodynamic and kinetic modelling of solid-liquid phase transformations in multi-component slag systems

Dipl.-Ing. Daniel Marian Ogris, BSc

July 2023

MONTANUNIVERSITÄT LEOBEN
www.unileoben.ac.at

EIDESSTATTLICHE ERKLÄRUNG

Ich erkläre an Eides statt, dass ich diese Arbeit selbständig verfasst, andere als die angegebenen Quellen und Hilfsmittel nicht benutzt, und mich auch sonst keiner unerlaubten Hilfsmittel bedient habe.

Ich erkläre, dass ich die Richtlinien des Senats der Montanuniversität Leoben zu "Gute wissenschaftliche Praxis" gelesen, verstanden und befolgt habe.

Weiters erkläre ich, dass die elektronische und gedruckte Version der eingereichten wissenschaftlichen Abschlussarbeit formal und inhaltlich identisch sind.

Datum 25.07.2023

Unterschrift Verfasser/in
Daniel Marian Ogris

ABSTRACT

In the course of this thesis, solid/liquid phase transformations in metallurgical slag systems are investigated. A thermodynamic software package is developed that can be used together with a thermodynamic database to calculate thermochemical equilibrium conditions and simulate the kinetics of solid-liquid phase transformations in multi-component, multi-phase systems. In order to gain a better understanding of the rate-determining processes, key experiments using High-Temperature Confocal Scanning Laser Microscopy (HT-CSLM) are performed. The experimental observations are complemented and interpreted by numerical modelling. The dissolution kinetics of various oxide particles in multi-component slags is predicted for the case that the interdiffusivity matrix is known. The combination of thermodynamic modelling and key experiments reveals the physical processes limiting the kinetics of the solid/liquid phase transformations. The kinetics of the dissolution of solid particles in multi-component slags appears to be diffusion controlled, where convection is considered by a decreased boundary layer thickness.

ZUSAMMENFASSUNG

In dieser Arbeit werden Fest/Flüssig-Phasenumwandlungen in metallurgischen Schlackensystemen untersucht. Es wird ein Softwarepaket entwickelt, das zusammen mit einer thermodynamischen Datenbank verwendet werden kann, um thermochemische Gleichgewichte in mehrkomponentigen, mehrphasigen Systemen zu berechnen und die Kinetik von Fest-Flüssig-Phasenumwandlungen zu simulieren. Um ein tieferes Verständnis für die ratenbestimmenden, dissipativen Prozesse zu erlangen, werden experimentelle Untersuchungen mittels High-Temperature Confocal Scanning Laser Microscopy (HT-CSLM) durchgeführt. Die experimentellen Beobachtungen werden durch numerische Modellierung ergänzt und interpretiert. Die Kinetik von Auflösungsprozessen verschiedener Oxidpartikel in mehrkomponentigen Schlacken kann bei bekannter Interdiffusivitätsmatrix vorhergesagt werden. Durch die Kombination aus thermodynamischer Modellierung und Schlüsselexperimenten können die physikalischen Prozesse enthüllt werden, welche die Kinetik der Fest/Flüssig-Phasenumwandlungen limitieren. Die Auflösungskinetik von Oxidpartikeln in mehrkomponentigen Schlackensystemen weist einen diffusionskontrollierten Charakter auf, wobei konvektive Beiträge zum Massetransport durch eine verringerte Grenzschichtdicke berücksichtigt werden.

Dedicated to my family.

ACKNOWLEDGMENTS

I would like to express my sincere gratitude to several individuals who have played a pivotal role in the completion of this thesis.

First and foremost, I would like to express my heartfelt appreciation to my parents. Their unconditional love, constant encouragement, and belief in my abilities have been the driving force behind my success. Their unwavering support, example and sacrifices throughout my life have been instrumental in shaping me into the person I am today. I am forever grateful for their presence in my life.

I am deeply indebted to my supervisor, Ernst Gamsjäger, for his invaluable guidance throughout this endeavor. His expertise, insightful feedback, and constant availability have been instrumental in shaping the direction of this work. I am grateful for his encouragement, precious time and belief in my potential.

Additionally, I would like to extend my deepest appreciation to my mentor, Johannes Schenk. I have greatly benefited from his remarkable enthusiasm, expertise, and unwavering support throughout my studies. His mentorship, constructive criticism, and challenging questions have enriched this work and its outcomes. I am grateful for the trust he placed in me and for the effort he dedicated to my development.

Lastly, I am grateful to all my friends and colleagues who provided encouragement,

support, and stimulating discussions throughout this journey. Their camaraderie and willingness to share their perspectives have been of immense value in shaping my ideas and pushing me to explore new horizons.

TABLE OF CONTENTS

LIST OF TABLES

LIST OF FIGURES

1 | Introduction

Steel is a fundamental pillar of modern society. The knowledge and ability to produce, shape and manipulate the properties of steel has been considered essential in order to accumulate wealth and prosperity throughout the beginning of the Iron Age. Still, great efforts are undertaken to develop steels with enhanced properties and to improve steelmaking processes.

1.1 Oxygen steelmaking

As of today, the oxygen steelmaking route is the dominating way of producing steel. More than 70% of annually produced steel is currently produced via oxygen steelmaking processes [1] in a refractory-lined furnace, i.e. the basic oxygen furnace (BOF) or the LD-converter[‡]. Basically, pure oxygen is blown at high pressures (12-15 bar) onto the surface of a liquid iron bath (hot metal), refining the metal and producing liquid steel. A large number of chemical components and phases are involved in oxygen steelmaking, and their interactions with each other must be considered for an accurate understanding of the process:

- The **gas phase** consisting mainly of CO ($\approx$ 90% in terms of total gas volume) and also CO_2 (their exact proportion is dependent on the processing temperature) as a product of the carbon oxidation during the blow.
- **Liquid iron** produced in the blast furnace typically containing (in relation to the total mass of the phase) 4.0-4.5% C, 0.05-0.12% P, 0.03-0.06% S, 0.5-1.0% Si, 1.0-6.0% Mn and potentially other impurities when entering the BOF. It is the main source of iron and energy in BOF steelmaking [2]. During the refining process, the amount of carbon and other impurities in the hot metal decreases due to exothermic reactions with oxygen penetrating the liquid bath. Due to these reactions, the temperature in the vessel rises rapidly and must be controlled by cooling agents, such as steel scrap, lime, magnesia, dolomite

[‡]LD usually refers to the initials of the steel plants Linz and Donawitz

and iron ores. In addition to their use as a cooling agent, scrap, i.e. recycled steel, and iron ores are added to the process to provide a source of iron, dilute impurities, and act as an alloying source, ultimately improving the process's efficiency and cost-effectiveness. Lime, magnesia and dolime are also involved in various other metallurgical tasks, which will be briefly discussed below.

- BOF **slags** are multi-phase mixtures of (partially) molten oxides. On a structural basis, molten slags consist of positively charged ions (cations) and negatively charged silicate, aluminate and phosphate complexes that are able to form three-dimensional polymerized network structures [2].

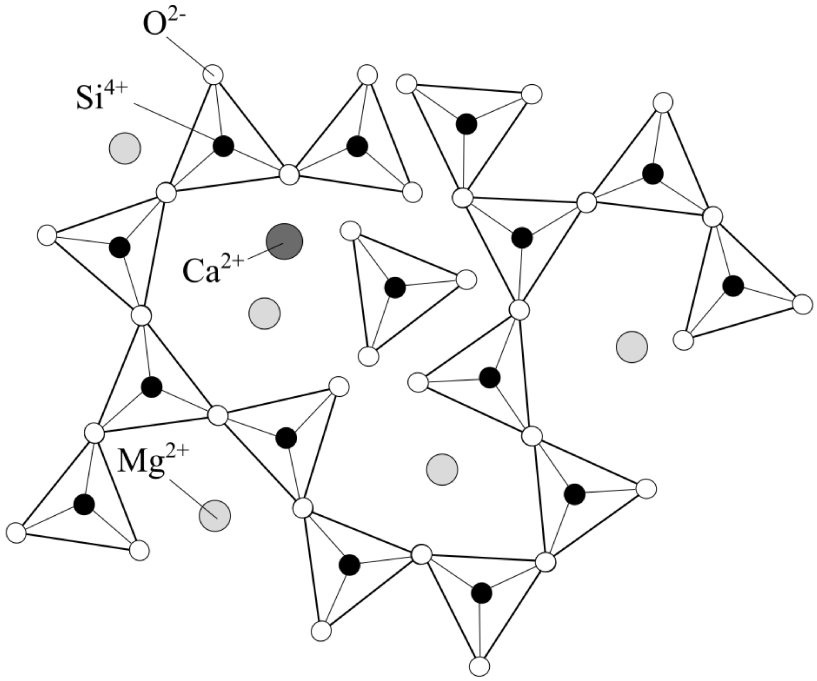

Figure 1.1: Representation of silica networks determining the physical properties of molten slags.

BOF slags contain significant amounts of silica; thus, their physical structure is determined by networks of SiO_4^{4-} tetrahedra, see Fig 1.1; each tetrahedron consists of a centered Si^{4+}-ion surrounded by four O^{2-}-ions positioned at the corners of the tetrahedron. The presence of cations such as Ca^{2+}, Mg^{2+} and Fe^{2+} results in a break down (depolymerization) of the silicate network [3]. Species that modify the silicate network by depolymerization are commonly referred to as network modifiers. Other species might be incorporated in the silicate network, e.g. PO_4^{3-}, these species are generally called network formers.

Although the ionic nature of liquid slags is generally accepted, their constitution is often represented formally by means of their comprising oxides, e.g. CaO, MgO, MnO, SiO_2 and FeO_x. In metallurgical practice slags are typically classified by means of numerical values expressing the relation of network breaking (or basic) oxides and network building (or acidic) oxides in the slag mixture. This so called "slag basicity" is often defined as

$$B_1 = \frac{w_{\mathrm{CaO}}}{w_{\mathrm{SiO_2}}} \,, \tag{1.1}$$

or

$$B_2 = \frac{w_{\mathrm{CaO}} + w_{\mathrm{MgO}}}{w_{\mathrm{SiO_2}}} \,, \tag{1.2}$$

where w_{CaO}, w_{MgO} and $w_{\mathrm{SiO_2}}$ are the mass fractions of CaO, MgO and SiO_2 in the liquid slag, respectively [4]. Although these simple ratios are often used, they cannot completely reflect the actual constitution and properties of complex phase mixtures. The representation of slag basicities in weight fractions is common in metallurgical practice, but is unfavorable from a thermodynamic point of view and does not directly allow a deeper insight into the relations of the individual species to each other. Rather, a detailed study of the equilibrium states at steelmaking conditions is required to capture the complex behavior of multi-component slag systems and their interactions with the other substances (fluxing agents, refractories, liquid iron, gases) present in the LD converter.
Slags perform a number of important tasks in metallurgical operations including the following [5]:

  - Slags are essential for the absorption of elements and non-metallic inclusions that are removed from the liquid iron.
  - They shield the metal bath from unwanted elements present in the atmosphere, such as sulfur, hydrogen or nitrogen.
  - They protect the liquid metal against heat losses by serving as a thermal insulation layer.
  - BOF slags might furthermore serve as a valuable resource after use in the metallurgical aggregate. The valorization of steelmaking slags is a very active research topic, see e.g. [6–14]

- **Refractories** shield the steel vessel from high temperatures (>1600°C) and corrosive substances (especially the liquid slag) that occur in oxygen steelmaking. Thus, a careful selection of the refractory material is mandatory in terms of safety and economic efficiency. LD-converters are almost exclusively lined with magnesia-carbon building materials of different qualities depending on the zone

of operation in the vessel. In the slag line area pitch-bonded MgO-C bricks containing additional antioxidants (Al, Si) are used [15]. During operation, the refractory material is exposed to corrosive slag attack and dissolves partially into the BOF slag. The dissolution of magnesia-based refractories can be minimized by feeding MgO-containing fluxing agents into the vessel during the oxygen blow and thus, saturating the liquid slag.

The main operational steps in oxygen steelmaking are schematically depicted in Figure 1.2 and are shortly recapitulated in the following.

1. **Charging scrap** is usually the first operational step in oxygen steelmaking. Scrap acts as a coolant and is charged before the hot metal to avoid splashing. To that aim the converter is tilted by about 45° and scrap is charged by means of a scrap carrier box manipulated by a charging crane.

2. **Charging of hot metal** is done by pouring the liquid metal from a transfer ladle onto the scrap.

3. Before the start of the oxygen **blow**, the converter is tilted back into an upright position with the mouth of the vessel being parallel to the floor. Then, oxygen is blown through a water-cooled lance with supersonic speed and violently reacts with the liquid metal bath via exothermic reactions. Thereby, carbon and other unwanted impurities are removed from the metal and form oxides that leave the converter in the form of gas (CO) or contribute to the formation of metallurgical slag that stays in contact with the liquid metal.

4. After the blow, the converter is tilted again to enable **sampling**, where temperature and chemistry of the metal are tested.

5. Once the target temperature and steel composition are reached, the converter is tilted in a way to allow the liquid metal to flow through the tap hole. This step is referred to as **tapping**.

6. **Slagging** is the last step in the oxygen steelmaking process. The remaining slag is removed from the converter by dumping it into a slag pot and also slag splashing is an option.

The intricacies of the individual steps will not be further elaborated and reference is made to the related literature for further reading, e.g. [1, 2, 5, 16]. Nevertheless, some key elements in terms of slag formation during the oxygen blow will be highlighted in the following in order to establish the context for the research undertaken in this work.

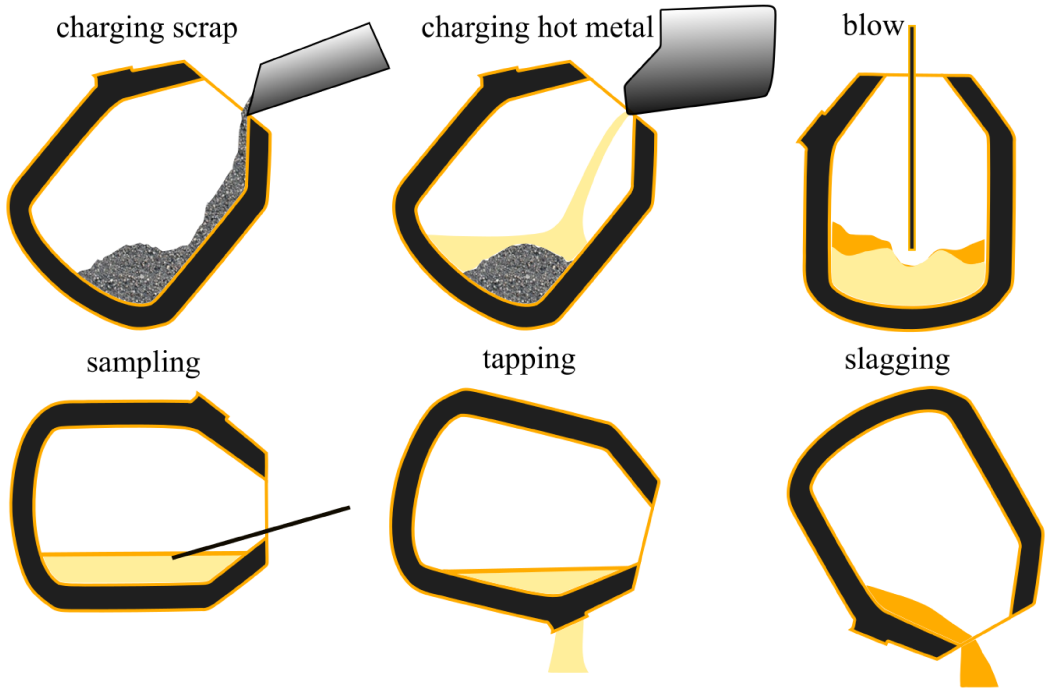

Figure 1.2: Schematic representation of the operational steps in the oxygen steelmaking process.

1.2 Some aspects of slag formation during oxygen steelmaking

The constitution of the LD slag is highly important for the steelmaking process as it affects crucially the metallurgical reactions taking place. Moreover, the basicity of the slag must be controlled during the steelmaking process. Thereby, the loss of refractory material is minimized and the ability of the slag to absorb impurities from the metal is optimized. In order to tune the chemistry of metallurgical slags during the blow CaO- and MgO-containing fluxing agents in the form of burned lime (CaO) or dolime ((Ca,Mg)O) are fed into the vessel. However, burnt lime - with a melting point of 2613°C [17] - needs to dissolve to contribute to the formation of a slag with the desired chemical and physical properties. This dissolution process can be promoted to a large extend by manipulating the position of the oxygen lance with respect to the hot metal surface. At the beginning of the blow, the lance is kept at a relatively large distance above the liquid metal. Hence, the penetration depth of the oxygen jet into the metal bath at the hot spot is only small and the oxidation of [Si][‡], [Mn], [C] and [Fe] in the oxygen-enriched regions beneath the hot spot is favoured. At the same time, the transport of thermodynamically oxidizable elements

[‡]The square brackets indicate that the element is dissolved in iron

to the hot spot is limited due to the insufficient mixing of the metal bath. Thus, large amounts of Fe are oxidized, which is available in large quantities near the hot spot. The formed iron oxides are flushed into the slag area in the converter; they react with the fluxing agents to form a basic slag by enabling the dissolution of the CaO- and MgO-containing additives. Rapid dissolution of fluxing agents such as lime or dolime contributes significantly to the productivity of the converter process. A precise understanding of the dissolution kinetics of the fluxing additives is required to adjust the constitution of converter slags according to metallurgical requirements. Key physical properties of BOF slags are their rheological behaviour, their liquid range in the temperature-composition space; moreover, the amounts and constitutions of potentially present solid phases, e.g. lime, tricalcium silicate (C3S) or dicalcium silicate (C2S). Furthermore, slags must be able to take part in metallurgical reactions, such as dephosphorization and desulfurization. In general, those thermodynamic states (chemical activities and stable phases) that promote the absorption of non-metallic inclusions and undesirable elements from the liquid metal are preferred. In order to meet these requirements, the properties of slags must be adjusted through thermodynamically-informed control of temperature and composition during processing.

1.3 Inclusion control during steelmaking

A second example, where the dissolution of oxide particles in steelmaking slags is of paramount importance is inclusion control and steel cleanliness. In this regard, the introduction and continuous improvement of ladle and tundish metallurgy have significantly contributed to the development of high quality steels with minimum amount of unwanted inclusions. The process of inclusion removal from the steel usually happens in the ladle furnace, the tundish or even the continuous casting mold and can be divided into the following three steps [18]:

1. The transport (flotation) of the inclusion to the slag-steel interface.
2. The separation across the slag-steel interface.
3. The dissolution of the inclusion in the molten slag.

In this context, the dissolution of oxide inclusions in molten slags is an invaluable process in the secondary metallurgy of high quality steels, see e.g. [18–24], as a rapid dissolution of unwanted oxides in optimized slags prevents from re-entrainment of the non-metallic inclusions [24]. There is an increasing demand for thermodynamic and kinetic models [25, 26] with predictive capabilities in order to contribute to the understanding of these processes and enhance the quality of the final product.

1.4 Scientific framework and objectives of this thesis

In the light of the above, it is of great interest to be able to predict the equilibrium phases in LD slags and the kinetics of the dissolution of oxides in steelmaking slags. To address these challenges, the research of this thesis is organized into three major parts in which the thermodynamics and the kinetics of solid-liquid phase transformations in multi-component slag systems are investigated by means of numerical modelling and experimental techniques:

- A thermodynamic software-package for the calculation of equilibrium phases in BOF slags during oxygen steelmaking is developed in the first part of this thesis that can be easily coupled to a comprehensive LD-process model [27–30].
- In the second part of this thesis, a physics-based sharp-interface model is developed for simulating the kinetics of solid-liquid phase transformations in multi-component slag systems; the entanglement of equilibrium calculations with the modelling of irreversible processes is discussed. The primary focus of this part of the thesis is on modelling the reaction kinetics of oxide particles with various slag systems with applications in the dissolution of additives during oxygen steelmaking, but also with respect to inclusion control and steel cleanliness.
- Finally, the numerical results are compared to data from High Temperature Confocal Scanning Laser Microscopy (HT-CSLM) experiments and conclusions for the rate limiting steps in solid-liquid phase transformations in multi-component slag systems are drawn.

2 State of the art

Various modelling approaches for describing or even predicting the kinetics of solid-liquid reactions between (shrinking) oxide particles and molten oxides are discussed in the open literature. In this chapter, an overview of the existing modelling approaches is given starting from simple models to more and more physically meaningful models with predictive capabilities. The discussion on the existing models will eventually lead to a discussion on the requirements for a thermodynamics based multi-component model, that is developed in this work.

2.1 Simple mass transfer models

Simple mass transfer models have been proposed in the literature [31–34] for interpreting experimental data of lime and dolime dissolution under forced convection

$$-\frac{dm^{\text{solid}}}{dt} = k_{\text{CaO}} A \rho_{\text{liq}} \frac{w^{\text{sat}}_{\text{CaO}} - w_{\text{CaO}}}{w^{\text{solid}}_{\text{CaO}} - w_{\text{CaO}}} \tag{2.1}$$

where t denotes time, m^{solid} is the mass of the solid with a mass fraction $w^{\text{solid}}_{\text{CaO}}$ of CaO dissolving in the liquid slag with mass fraction w_{CaO}. The solubility limit of CaO in the liquid phase is denoted $w^{\text{sat}}_{\text{CaO}}$, A is the interaction area and the mass transfer coefficient for CaO is k_{CaO}. The simplified mass transfer model is normally used only for quantitative evaluation of experimental results. It does not capture the physical reality of the occurring irreversible processes and cannot be used to predict the dissolution kinetics of oxides in liquid slags.

2.2 The classical shrinking-core model

The shrinking-core model has been applied extensively to interpret fluid-particle reactions with a focus on oxide particle dissolution in metallurgical slags in previous works, e.g., [35–40]. In the context of oxide particle dissolution, the model is often used to discuss the rate determining steps of the dissolution process. Usually, a 1D-spherical system is considered that consists of the shrinking oxide particle surrounded by a

liquid film, which in turn is encompassed by the liquid bulk. In contrast to the liquid bulk, the concentration gradients of the diffusing species in the liquid film adjacent to the particle are non-zero. A representation of the geometrical situation is shown in Fig 2.1. The rate of reaction for shrinking particles can be described by a three-step process (see e.g. [41]), were the three sub-processes occurring simultaneously on different time-scales are:

1. The diffusion of reactants from the liquid bulk to the solid-liquid interface through a so called liquid film with non-zero concentration gradients.

2. One or multiple chemical reactions at the solid-liquid interface.

3. The diffusion of the reaction products from the solid-liquid interface into the liquid bulk through the liquid film.

In general, any of these sub-processes can act as the rate-controlling mechanism for the dissolution, and it is also conceivable that all three mechanisms contribute to the reaction kinetics. In some cases, e.g. in the case of lime dissolution in silica-containing slags, a product layer might form at the solid-liquid interface. In this case, a new interface between the product layer and the shrinking particle is formed (see Fig 2.1 right) and two additional sub-processes occur:

4. The diffusion of reactants from the liquid film through the product layer to the solid-solid interface of the unreacted particle and the product layer.

5. The diffusion of reaction products from the solid-solid interface through the product layer into the liquid film.

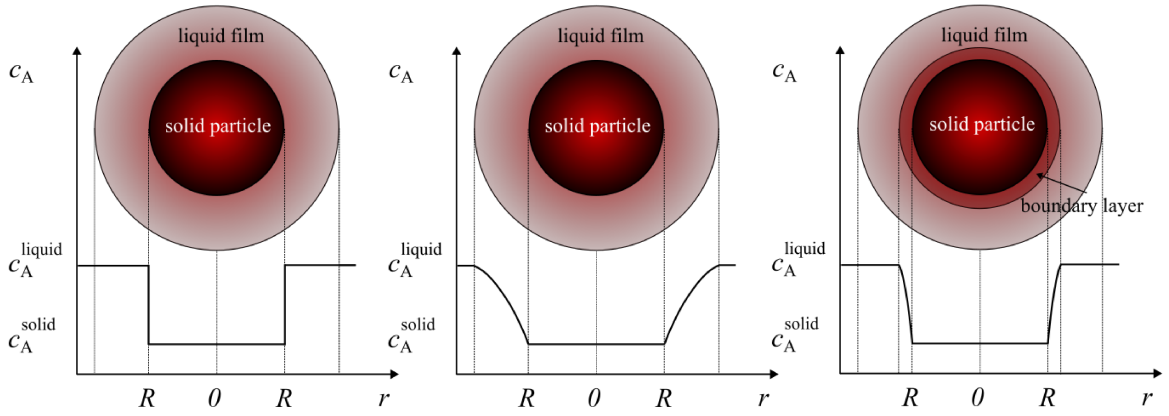

Figure 2.1: Schematics representing the geometric conditions and concentration profiles for a shrinking particle subject to (from left to right) chemical reaction control, liquid film diffusion control and boundary layer diffusion control, respectively.

The geometric conditions and concentration profiles during the dissolution of a spherical particle modelled by means of the shrinking core model are presented in Fig 2.1. The three different cases shown represent the conditions for transformation kinetics that are limited by chemical reaction, liquid-film diffusion and boundary layer diffusion, respectively. In the following, the different control modes defined in the classical shrinking-core model are discussed. The following derivations are elaborated in [41] in a similar manner. However, to avoid misunderstandings in terminology and misconceptions with regard to the use of the classical shrinking-core model these derivations are investigated here in detail to reveal significant simplifications that are often unmentioned in literature.

2.2.1 Chemical reaction control

Fluid-particle reactions can be represented by a pseudo-chemical equation of the type

$$(\mathrm{A}) + b\mathrm{B}(\mathrm{s}) \rightarrow \text{products} \ , \tag{2.2}$$

where A and B are chemical species and b is a stoichiometric coefficient. The amount n_B of species B in mol is given by

$$n_\mathrm{B} = \rho_\mathrm{B} V \ , \tag{2.3}$$

where ρ_B is the molar density (mol/m^3) of B and V is the volume of the dissolving particle. In the case where a chemical reaction determines the kinetics of the dissolution process, the rate of the shrinking particle radius is proportional to the reaction

area. Assuming the chemical reaction kinetics to be of first-order, the rate of reaction for a spherical particle can be written as

$$-\frac{dn_{\mathrm{A}}}{dt} = \underbrace{4\pi r^2}_{\text{reaction area}} \; k' c_A^{\mathrm{I}} \; , \tag{2.4}$$

where k' is the rate of reaction (in s^{-1}) for the interface reaction and c_A^{I} is the concentration of species A (in $\mathrm{mol/m}^3$) at the side of the interface averted from the core of the solid particle. Combining Eq (2.3) and Eq (2.4) gives

$$-\frac{dn_{\mathrm{B}}}{dt} = -\rho_{\mathrm{B}} \frac{dV}{dt} \; , \tag{2.5}$$

and

$$-\cancel{4\pi r^2} \rho_{\mathrm{B}} \frac{dr}{dt} = \cancel{4\pi r^2} b \, k' c_A^{\mathrm{I}} \; . \tag{2.6}$$

The integration of the variables leads to the a relation between the original radius of the particle R_0, the dissolution time $\tilde{t}$ and the current radius R :

$$-\rho_{\mathrm{B}} \int_{R_0}^{R} dr = b \, k' c_A^{\mathrm{I}} \int_{\tilde{t}_0=0}^{\tilde{t}} dt = -\rho_{\mathrm{B}} (R - R_0) = b \, k' c_A^{\mathrm{I}} \tilde{t} \; , \tag{2.7}$$

and accordingly

$$\tilde{t} = \frac{\rho_{\mathrm{B}}}{b \, c_A^{\mathrm{I}} k'} (R_0 - R) \; . \tag{2.8}$$

The total dissolution time $\tilde{t}_{\mathrm{tot}}$ is the time elapsed when $R = 0$. Normalizing the time by the total dissolution time leads to the characteristic linear equation of reaction limited dissolution kinetics:

$$\frac{\tilde{t}}{\tilde{t}_{\mathrm{tot}}} = (1 - \frac{R}{R_0}) \; . \tag{2.9}$$

The graphical representation of the evolution of the normalized radius R/R_0 with normalized time $\tilde{t}/\tilde{t}_{\mathrm{tot}}$ is called the dissolution profile and is shown in Fig 2.2. Often, rate limiting steps in solid-fluid reactions are identified by comparing experimentally derived dissolution profiles to the characteristic dissolution profiles following from the shrinking-core model, e.g. [38, 42].

2.2.2 Diffusion/mass transfer through liquid film

Although, this control mode is related to diffusion through the liquid film, the diffusion equations are not applied. The diffusion problem is transformed into a mass-transfer problem at the interface

$$-\frac{dn_{\mathrm{B}}}{dt} = 4\pi r^2 \, b \, k_{\mathrm{m}} \left(c_{\mathrm{A}}^{\mathrm{liquid}} - c_{\mathrm{A}}^{\mathrm{solid}} \right) \; , \tag{2.10}$$

where k_m is called the mass transfer coefficient and $(c_\mathrm{A}^\mathrm{liquid} - c_\mathrm{A}^\mathrm{solid})$ is the difference of the concentrations of A in the liquid bulk and in the solid. It is worth noting that formally Eq (2.10) agrees with Eq (2.4), hence actually describing the kinetics of chemical reaction control. Combining Eq (2.3) with Eq (2.10) gives

$$-\rho_\mathrm{B}\frac{dr}{dt} = b\,k_\mathrm{m}\left(c_\mathrm{A}^\mathrm{liquid} - c_\mathrm{A}^\mathrm{solid}\right) . \tag{2.11}$$

The mass transfer coefficient k_m is often related to the diffusion coefficient D and the particle radius r in the following form:

$$k_\mathrm{m} = \frac{D}{r} . \tag{2.12}$$

Substitution of Eq (2.12) into Eq (2.11) and integration gives

$$\int_{R_0}^{R} r dr = -\frac{bD\left(c_\mathrm{A}^\mathrm{liquid} - c_\mathrm{A}^\mathrm{solid}\right)}{\rho_\mathrm{B}} \int_{\tilde{t}_0=0}^{\tilde{t}} dt = R^2 - R_0^2 = -\frac{2bD\left(c_\mathrm{A}^\mathrm{liquid} - c_\mathrm{A}^\mathrm{solid}\right)}{\rho_\mathrm{B}}\tilde{t} . \tag{2.13}$$

The time $\tilde{t}$ relative to the start of the dissolution process is

$$\tilde{t} = \frac{\rho_\mathrm{B} R_0^2}{2bD\left(c_\mathrm{A}^\mathrm{liquid} - c_\mathrm{A}^\mathrm{solid}\right)}\left(1 - \left(\frac{R}{R_0}\right)^2\right) , \tag{2.14}$$

and the total dissolution time $\tilde{t}_\mathrm{tot}$ can be obtained by setting $R = 0$. The characteristic equation for mass controlled dissolution is then

$$\frac{\tilde{t}}{\tilde{t}_\mathrm{tot}} = 1 - \left(\frac{R}{R_0}\right)^2 . \tag{2.15}$$

The dissolution profile for mass transfer controlled dissolution is shown in Fig 2.2.

2.3 Diffusion through a boundary layer

If a boundary layer forms around a shrinking particle, diffusion through this layer might limit the dissolution kinetics. Strictly speaking, the boundary layer model is only valid for solid-gas reactions where the shrinkage of the particle is much slower than the flow rate of the components towards the solid-solid interface between the unreacted particle and the boundary layer [41]. The rate of n_A is determined by the diffusive flux J_A and is proportional to the reaction area

$$-\frac{dn_\mathrm{A}}{dt} = 4\pi r^2 J_\mathrm{A} , \tag{2.16}$$

with the diffusive flux of A being

$$J_{\mathrm{A}} = D\frac{dc_{\mathrm{A}}}{dr} \ , \tag{2.17}$$

resulting in

$$-\frac{dn_{\mathrm{A}}}{dt} = 4\pi r^2 D\frac{dc_{\mathrm{A}}}{dr} \ . \tag{2.18}$$

Integration across the boundary layer gives

$$-\frac{dn_{\mathrm{A}}}{dt}\int_{r=R_0}^{\tilde{R}}\frac{dr}{r^2} = 4\pi D\int_{c_{\mathrm{A}}=c_{\mathrm{A}}^{\mathrm{solid}}}^{c_{\mathrm{A}}^{\mathrm{liquid}}} dc_{\mathrm{A}} = -\frac{dn_{\mathrm{A}}}{dt}\left(\frac{1}{\tilde{R}}-\frac{1}{R_0}\right) = 4\pi D\left(c_{\mathrm{A}}^{\mathrm{liquid}}-c_{\mathrm{A}}^{\mathrm{solid}}\right) \ . \tag{2.19}$$

It can be seen from the above relation, that the rate of n_{A} is constant for constant radius $\tilde{R}$. By applying Eq (2.3) and integrating over time and radius, the change of the boundary layer thickness is considered:

$$-\rho_{\mathrm{B}}\int_{\tilde{R}=R_0}^{R}\left(\frac{1}{\tilde{R}}-\frac{1}{R_0}\right)\tilde{R}^2 d\tilde{R} = bD\left(c_{\mathrm{A}}^{\mathrm{liquid}}-c_{\mathrm{A}}^{\mathrm{solid}}\right)\int_{\tilde{t}_0=0}^{\tilde{t}} dt \tag{2.20}$$

giving

$$\tilde{t} = \frac{\rho_{\mathrm{B}}R_0^2}{6bD\left(c_{\mathrm{A}}^{\mathrm{liquid}}-c_{\mathrm{A}}^{\mathrm{solid}}\right)}\left(1-3\left(\frac{R}{R_0}\right)^2+2\left(\frac{R}{R_0}\right)^3\right) \tag{2.21}$$

and with the total time $\tilde{t}_0$ being defined at $R=0$:

$$\frac{\tilde{t}}{\tilde{t}_0} = 1-3\left(\frac{R}{R_0}\right)^2+2\left(\frac{R}{R_0}\right)^3 \tag{2.22}$$

The characteristic dissolution profile for a boundary-diffusion limited process is compared to liquid film diffusion control and chemical reaction control in Fig 2.2.

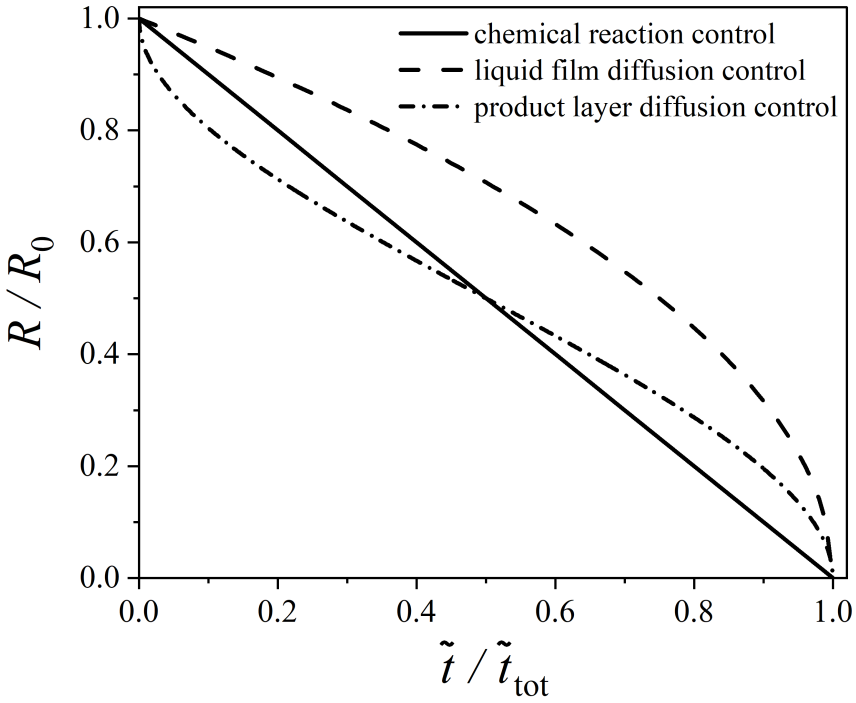

Figure 2.2: The characteristic dissolution profiles for the shrinking core model.

Recently, an extended shrinking-core model has been suggested for the dissolution of lime in steelmaking slags by Sarkar et al. [43] by assuming a mixed-mode mechanism. However, comparison with experimental data could only be achieved with several empirical parameters and relations. Strictly speaking, the shrinking-core model does only hold for binary systems. However, it is frequently used for modelling multi-component problems by means of introducing the concept of effective binary diffusion; the multi-component system is reduced to a binary system by selecting a main diffusing species and reducing all other components in the system to a fictive second component. However, significant couplings between the diffusive fluxes of the individual components and the gradients of their chemical potentials leading to non-linear diffusion paths and concentration peaks can not be studied by the effective binary approximation, see e.g. [44]. Thus, the classical shrinking-core model should be applied to ternary or higher order systems only with great care.

2.4 Diffusion limited models based on approximate solutions of the coupled diffusion-moving boundary problem

Experimental observations reveal in many cases that diffusion processes play a major role in oxide particle dissolution [36–38, 42, 45–48]. However, the classical shrinking-core model often does not compare well quantitatively or qualitatively with experimental data. To fit a mathematical model to the experimental data various approximations to the moving boundary problem have been introduced [39, 42, 48, 49], where either the position of the solid/liquid interface or the concentration profile do not change with time. For relatively small dissolution rates, the interface has only a minor influence on the concentration field [44]. The mass balance at the interface (Stefan's interface condition) is

$$[[c]]\frac{dR}{dt} = J_R = D\frac{\partial c}{\partial r}\bigg|_{r=R} \tag{2.23}$$

where, $[[c]]$ denotes the concentration jump at the interface between the spherical particle and its surrounding (liquid) matrix. The mass balance at the interface is combined with the solution of Fick's second law for spherical systems:

$$c(r,t) = c_S + (c_R - c_S)\frac{R_0}{r}\mathrm{erfc}\left(\frac{r-R_0}{\sqrt{4Dt}}\right) \ , \quad r \geq R_0 \tag{2.24}$$

where c_R and c_S are the concentrations at the liquid side of the interface and infinitely far away from the interface, respectively. Combination of Eq (2.23) and Eq (2.24) results in the "quasi-static approximation"; the velocity of the interface dR/dt is determined by Eq (2.23) and the diffusive fluxes J_R are derived from Eq (2.24), i.e. concentration field is treated as if the radius of the spherical particle remains constant. The interface velocity becomes then

$$\frac{dR}{dt} = -\frac{c_R - c_S}{[[c]]}\left(\frac{D}{R} + \sqrt{\frac{D}{\pi t}}\right) \ . \tag{2.25}$$

The quasi-static approximation fails to predict the kinetics of oxide particle dissolution in many cases and, thus, has been modified by introducing additional physically meaningless parameters to fit numerical results to experimental observations [42, 48]. However, the field of application for the quasi-static approximation could be defined by comparing it to the analytical solution of the moving boundary problem.

Analytical solutions of the moving boundary problem exist only for special cases. Such a special case is the shrinking/growing of spheres in infinitely large binary systems in the diffusion-limited case with a constant diffusion coefficient. Following

Glicksman [44], a characteristic diffusion parameter K_{sphere} is introduced relating the displacement of the spherical interface $(R(t) - R_0)$ and the time t in case of diffusion controlled transformations:

$$K_{\text{sphere}} = \frac{R(t) - R_0}{\sqrt{4Dt}} \; . \tag{2.26}$$

The characteristic diffusion parameter K_{sphere} can be related to another key parameter, the non-dimensional supersaturation Λ, representing the boundary conditions of the diffusion problem:

$$2K_{\text{sphere}}^2 \left(1 - \sqrt{\pi} K_{\text{sphere}} \exp\left(K_{\text{sphere}}^2\right) \text{erfc}(K_{\text{sphere}})\right) = \frac{c_R - c_S}{[[c]]} = \Lambda \; . \tag{2.27}$$

Thereby, the thermodynamic contact conditions at the interface, namely the jump condition $[[c]]$, influences the evolution of the radius $R(t)$ in Eq (2.27). Usually, when it comes to studying diffusion-limited growth or shrinkage of particles, the non-dimensional matrix supersaturation is chosen as the independent variable. Unfortunately, Eq (2.27) can not be inverted analytically [44] and, thus, must be inverted graphically (using Fig 2.3) or solved for K_{sphere} numerically. In Fig 2.3 the analytical solution of the moving boundary problem is compared to the quasi-static approximation. While for low values of Λ the two solutions agree well with each other, there is a increasing discrepancy as Λ rises. At $\Lambda \geq 0.1$ the results from the quasi-static approximation become significantly unreliable. A critical evaluation of approximate solutions is also given by Guo et al. [50].

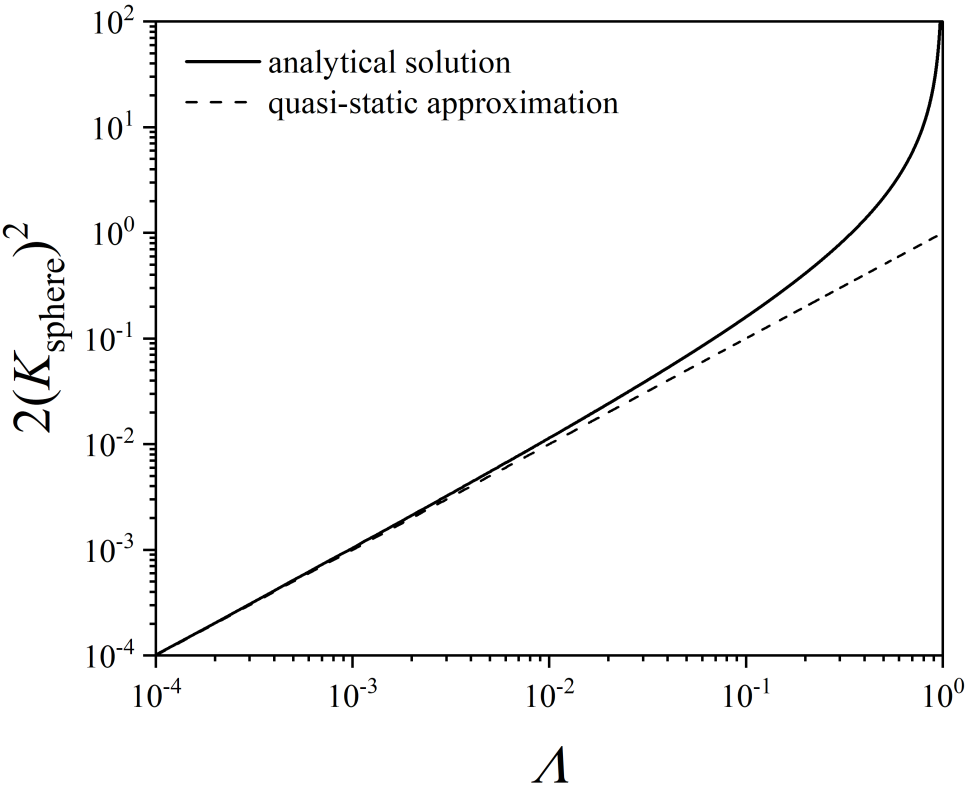

Figure 2.3: Comparison of the analytical solution of the moving boundary problem to the quasi-static approximation, see also [44].

2.5 Lattice-Boltzmann models

Verhaeghe et al. [51, 52] proposed a 2D-lattice Boltzmann model for the dissolution of solids of arbitrary shape in multi-component liquids and applied their model to the dissolution of alumina particles in CaO-Al_2O_3-SiO_2 slags [53, 54]. The lattice Boltzmann method (LBM) originates from statistical physics. It is a numerical method commonly used to solve fluid mechanics problems. The key concept is describing the current state of the system in terms of the discrete-velocity distribution function $f_d(\underline{z}, t)$, which is a function of the spatial-position $\underline{z}$ and time t, see e.g. [55]. The discrete-velocity distribution function represents the density of particles with velocity $\underline{v}_d$ and is defined on a grid discretizing space and time. From the discrete-velocity distribution function other quantities such as the mass density ρ and the momentum

density $\rho\underline{u}$ can be calculated:

$$\rho(\underline{z},\, t) = \sum_d f_d(\underline{z}, t) \tag{2.28}$$

and

$$\rho\underline{u}(\underline{z},\, t) = \sum_d \underline{v}_d f_d(\underline{z}, t)\ . \tag{2.29}$$

For each time step Δt the discrete-velocity distribution function $f_d(\underline{z}, t)$ is updated via:

$$f_d(\underline{z} + \underline{v}_d\Delta t,\, t + \Delta t) = f_d(\underline{z},\, t) + J_d(\underline{z},\, t)\ , \tag{2.30}$$

where $J_d(\underline{z},\, t)$ is the position and time dependent collision operator, which describes the interactions of particles during one time step. These collisions result in a redistribution of particles on the discretizing grid depending on the actual mathematical form of the collision operator.

For diffusion controlled dissolution of solid particles in multi-component fluids Verhaeghe et al [51] used lattice Boltzmann equations of the type:

$$f_d^j(\underline{z} + \underline{v}_d\Delta t,\, t + \Delta t) = f_d^j(\underline{z},\, t) + J_d^{jj} + J_d^{jk} \quad , \tag{2.31}$$

where f_d^j is the discrete-velocity distribution function for component j and the collision operator is split in two terms J_d^{jj} and J_d^{jk}. The first collision term J_d^{jj} represents the collision of particles of the same type. Hence, J_d^{jj} is called the self-collision operator and is given by

$$J_d^{jj} = -\frac{1}{\tau_j}(f_d^j - f_d^{j(0)})\ , \tag{2.32}$$

where τ_j is the relaxation time and $f_d^{j(0)}$ the equilibrium distribution function. The collision of unlike particles is handled via the cross-collision term J_d^{jk}:

$$J_d^{jk} = -\frac{\rho_k f_d^{j(\mathrm{eq})}}{\tau_D \rho R_j T}\,(\underline{v}_d - \underline{u}) \cdot \left(\underline{u}_j - \underline{u}_k\right)\ , \tag{2.33}$$

where ρ_k is the mass density of component $k \neq j$, $R_j = k_\mathrm{B}/m_j$ is the gas constant of component j, with k_B being the Boltzmann constant and m_j the molecular mass of component j; $\underline{u}_j$ and $\underline{u}_k$ are the flow velocities of component k and j, respectively. The relaxation time τ_D is related to the effective-binary diffusion coefficient D, see [56]. The collision operator relaxes the system towards the equilibrium distribution

$$f_d^{j(0)} = \left(1 + \frac{1}{R_d T}\,(\underline{v}_d - \underline{u}) \cdot (\underline{u}_d - \underline{u})\right) f_d^{j(\mathrm{eq})}\ , \tag{2.34}$$

with

$$f_d^{j(\mathrm{eq})} = w_d \rho_j \left(1 + \frac{\underline{v}_d \cdot \underline{u}}{R_d T} + \frac{\underline{v}_d \cdot \underline{u}}{2(R_d T)^2} - \frac{\underline{u} \cdot \underline{u}}{2 R_d T} \right) . \tag{2.35}$$

It can be seen that the equilibrium distributions $f_d^{j(0)}$ depend on the local quantities ρ and $\underline{u}$ only, which are calculated from the local values of f_d^j. The weight factors w_j introduced in Eq (2.35) depend on the choice of the discrete velocity set $\underline{v_d}$; details can be found in [55]. Usually, lattice Boltzmann equations are solved in two subsequent steps:

1. In the first step, the density ρ and the macroscopic velocity $\underline{u}$ are obtained using Eq (2.28) and Eq (2.29), respectively, to calculate the equilibrium distribution $f_d^{j(0)}$ and post-collision distribution. This step is referred to as the collision or relaxation step.

2. In the second step, the resulting distributions from the first step are subsequently streamed to all neighbouring nodes of the discretizing grid. This step is usually called the streaming step.

It can be shown that the macroscopic equations solved by this model are diffusion-convection equations of the form

$$\frac{\partial \varphi}{\partial t} + \underline{u} \cdot \nabla \varphi = \frac{1}{\rho} \nabla \cdot (D \nabla \varphi + \underline{F}) , \tag{2.36}$$

with the force term $\underline{F}$ accounting for the pressure gradient and contributions from external forces [56]; φ represents the difference of the mass fractions of components j and k and is given by

$$\varphi = \left(\frac{\rho_j - \rho_k}{\rho_j + \rho_j} \right) . \tag{2.37}$$

The details of the so-called Chapman-Enskog analysis, which deals with finding macroscopic equations from Boltzmann collision operators, will not be elaborated here. The interested reader is referred to the extensive further literature on statistical physics and the lattice Boltzmann method, e.g. [55–58].

Verhaeghe et al. [53,54] demonstrated the applicability of lattice Boltzmann models to predict the kinetics of oxide particle dissolution in metallurgical slags within several limitations: The simulations performed are based on representative binary systems for the dissolution of alumina in ternary slag systems. Effective binary diffusion coefficients have to be introduced instead of taking multi-component diffusion relations into account, thus treating the individual components as equal species. This simplification leads to the unrealistic result of straight diffusion paths in multi-component systems. For the prediction of multi-component diffusion paths, however,

local thermodynamic calculations must also be taken into account. This will be further elaborated in a later chapter. While LBM is a versatile and powerful tool, calculations based on the LBM are computationally demanding, thus they are generally not used as sub-routines in comprehensive models of metallurgical processes.

2.6 Models accounting for non-linear diffusion paths

The highly non-linear nature of diffusion paths in BOF slags during the dissolution of alumina particles is evaluated by Tripathi et al. [59] via experimental observations indicating that multi-component couplings between diffusive fluxes and their corresponding thermodynamic forces should not be neglected. However, as implied above, only few metallurgically related dissolution models presented in literature account for multi-component phenomena. A phase field model for oxide melts accounting for multi-component diffusion has been developed by Heulens et al. [60] and has been applied to simulate the dissolution of alumina particles in ternary CaO-SiO_2-Al_2O_3 slags by Liu et al. [61]. They assume multi-component diffusion in the bulk material as the rate determining process and predict non-linear diffusion paths during the transformation process. In their model they use thermodynamic computations to calculate thermodynamic factors and chemical potentials of all diffusing species. The thermodynamic approach to the kinetics of phase transformations distinguishes the phase field model at a fundamental level from the previously mentioned models, which only use thermodynamic calculations to predict solubility limits. Liu et al. [61] use the commercial thermodynamic software package ChemApp [62] from FactSage [63] as an external tool for their thermodynamic computations.
From what has been said so far, it can already be concluded that a model aiming to describe the physics of solid-liquid phase transitions in metallurgical slag systems must be capable of representing their multi-component nature in a suitable manner. Furthermore, the ability to directly calculate the thermodynamic boundary conditions might be advantageous; this aspect will be further elaborated. The calculation of thermodynamic equilibria in complex chemical systems using state of the art algorithms is part of the objectives in this work; a brief introduction to equilibrium calculations with a focus on the method of Gibbs energy minimization is discussed in the following.

2.7 Calculations of thermochemical equilibria

While metallurgical processes typically take place far from thermodynamic equilibrium, the kinetics of metallurgical reactions can be properly described only once the equilibrium state of the system is known, see [64]. Knowing the global thermodynamic equilibrium conditions is a key requirement for predicting the direction in which a

process is going to evolve. Furthermore, as will be discussed in more detail later, thermodynamics is inherently intertwined with the kinetics of irreversible processes on a fundamental level.
Equilibrium calculations are often tackled by identifying the dominant chemical reaction where a single equilibrium constant can be defined. While this procedure is best applied to very simple systems (i.e. ideal homogeneous systems), equilibrium calculations in multi-component and multi-phase systems demand numerically more sophisticated approaches.

2.7.1 The stoichiometric approach

A thermochemical system may be classified by the vector $\underline{n}_0$ containing the molar amounts n_i of the N individual species i that can possibly exist in the system. The thermochemical system can transform into an energetically more favourably state $\underline{n}$ by means of C independent chemical reactions [65]

$$\underline{n} = \underline{n}_0 + \sum_{\varkappa=1}^{C} \underline{\nu}_\varkappa \xi_\varkappa \, , \tag{2.38}$$

where $\underline{\nu}_\varkappa$ is called the stoichiometric vector and $\xi_\varkappa$ is the extent of reaction $\varkappa$. The equilibrium state of the system at constant temperature T and pressure P can be calculated by minimizing the Gibbs energy in terms of the C extents of reaction $\xi_\varkappa$

$$\left(\frac{\partial G}{\partial \xi_\varkappa}\right)_{T,P,\xi_{\kappa\neq\varkappa}} = 0 \, , \qquad \varkappa = 1, ..., C \, . \tag{2.39}$$

By applying the chain rule one gets

$$\left(\frac{\partial G}{\partial \xi_\varkappa}\right)_{T,P,\xi_{\kappa\neq\varkappa}} = \sum_{i=1}^{N} \left(\frac{\partial G}{\partial n_i}\right)_{T,P,n_{k\neq 1}} \left(\frac{\partial n_i}{\partial \xi_\varkappa}\right)_{\xi_{\kappa\neq\varkappa}} \, , \qquad \varkappa = 1, ..., C \, . \tag{2.40}$$

The chemical potential μ_i of a species i is defined as

$$\left(\frac{\partial G}{\partial n_i}\right)_{T,P,n_{k\neq i}} = \mu_i \, . \tag{2.41}$$

Moreover, the change of the molar amounts n_i with the progression of the chemical reactions can be related to the stoichiometric vector via

$$\left(\frac{\partial n_i}{\partial \xi_\varkappa}\right)_{\xi_{\kappa\neq\varkappa}} = \nu_{i,\varkappa} \, . \tag{2.42}$$

By combining Eqs (2.39), (2.41) and (2.42) the equilibrium conditions are given by C equations of the form

$$\sum_{i=1}^{N} \nu_{i,\varkappa} \mu_i = 0 \ , \qquad \varkappa = 1, ..., C \ . \tag{2.43}$$

The equilibrium values of the elements of $\underline{n}$ are obtained by solving the set of equations of the form (2.43). Usually, Eq (2.43) is solved by introducing $\varkappa$ equilibrium constants $K_\varkappa$. For the definition of the equilibrium constant, the chemical potentials are written in the form

$$\mu_i = \mu_i^\circ + RT \ln a_i \ , \tag{2.44}$$

where μ_i° is the reference value of the chemical potential of species i, a_i is the chemical activity of species i in a solution phase (for stoichiometric phases $a_i = 1$) and R is the ideal gas constant. Combining Eqs (2.43) and (2.44) the equilibrium condition becomes

$$\sum_{i=1}^{N} \nu_{i,\varkappa} \mu_i^\circ + RT \sum_{i=1}^{N} \nu_{i,\varkappa} \ln a_i = 0 \ . \tag{2.45}$$

The first term is called the standard Gibbs free energy change $\Delta G_\varkappa^\circ$ of reaction $\varkappa$

$$\Delta G_\varkappa^\circ = \sum_{i=1}^{N} \nu_{i,\varkappa} \mu_i^\circ \tag{2.46}$$

Eventually, the equilibrium constant $K_\varkappa$ is defined by means of combining Eqs (2.45) and (2.46)

$$-\frac{\Delta G_\varkappa^\circ}{RT} = \ln \left(\prod_{i=1}^{N} a_i^{\nu_{i,\varkappa}} \right) = \ln K_\varkappa \ , \tag{2.47}$$

where $\ln K_\varkappa$ is only dependent on temperature T and pressure P. The equilibrium constant method is widely used for calculating thermochemical equilibria in simple systems [66]. Eq (2.47) relates the activities a_i of the products and reactants of the chemical reaction; however, in general, the equilibrium amounts n_i can not simply be obtained from the activities a_i.

A simple iterative algorithm based on the stoichiometric equilibrium condition Eq (2.43) is suggested by Naphtali [67, 68]. Here, the equilibrium constants $K_\varkappa$ are not used; nontheless, the computability of the chemical potentials μ_i is required. At each iteration $\aleph$ the extents of chemical reactions $\xi_\varkappa^\aleph$ are updated by $\Delta\xi_\varkappa^\aleph$ using

$$\Delta\xi_\varkappa^\aleph = \left(\frac{\partial G}{\partial \xi_\varkappa} \right)^\aleph = -\Delta G_\varkappa^\aleph = -\sum_{i=1}^{N} \nu_{i,\varkappa} \mu_i^\aleph \ , \qquad \varkappa = 1, ..., C \ . \tag{2.48}$$

The molar amounts n_i are updated by

$$n_i^{\aleph+1} = n_i^{\aleph} + \Delta n_i^{\aleph} \ , \tag{2.49}$$

with

$$\Delta n_i^{\aleph} = \sum_{\varkappa=1}^{C} \nu_{i,\varkappa} \Delta \xi_{\varkappa}^{\aleph} \ , \qquad i = 1, ..., N \ . \tag{2.50}$$

Although Napthtali's algorithm is straight-forward and easy to implement, it is rarely used, due to its bad convergence properties; however, there exist various generally applicable numerical algorithms (see e.g. [65, 69–74]) based on the stoichiometric equilibrium condition (2.43).

2.7.2 The non-stoichiometric approach

While the stoichiometric approach is physically justified, it requires that all independent chemical reactions between the species in the system are known [64]. Typically, in pyro-metallurgical processes a large number of chemical reactions occur simultaneously in a multi-component, multi-phase system. Thus, for metallurgical applications the non-stoichiometric formulation is often preferred, where the equilibrium state is found by minimization of the Gibbs energy subject to mass balance (and possibly other) constraints. Mathematically speaking, Gibbs energy minimization (GEM) is a constrained non-convex optimization problem and can be formulated as

$$\text{minimize} \ \ G = \sum_{i}^{N} n_i \mu_i, \tag{2.51a}$$

$$\text{subject to (s.t.)} \ \ \sum_{i=1}^{N} A_{ij} n_i = b_j \ , \qquad j = 1, ..., M \tag{2.51b}$$

$$n_i \geq 0 \qquad i = 1, ..., N. \tag{2.51c}$$

Here, A_{ij} is the stoichiometric coefficient of a species i containing component j and b_j is the amount of component j in the system. The difficulty of solving non-convex optimization problems arises from the following characteristics of non-convex problems:

- The possible existence of multiple local minima in the solution space.
- The existence of saddle points.

- Flat regions that make it hard to identify distinct local search directions.

The minimization problem is usually approached using the method of Lagrange multipliers a technique used to find the extreme values of a function - the Lagrangian $\mathscr{L}$ - subject to various constraints. The Lagrangian to be minimized considering the mass balance is

$$\mathscr{L}(\underline{n}, \underline{\chi}) = \sum_{i}^{N} n_i \mu_i + \sum_{j=1}^{M} \chi_j \left(b_j - \sum_{i=1}^{N} A_{ij} n_i \right) , \tag{2.52}$$

where $\underline{\chi}$ is the set of unknown Lagrangian multipliers χ_j. The Lagrange multipliers χ_j hold physical significance in that they correspond to the chemical potentials of the system's components. At equilibrium, these chemical potentials χ_j must be uniform across all stable phases for every component. This relationship becomes evident by examining the partial derivatives of the Lagrangian with respect to n_i, as is evident from Equation (2.53) below. The minimum of the Lagrangian $\mathscr{L}$ corresponds to the minimum of the Gibbs energy G and is obtained by setting the derivatives in terms of the variables n_i and χ_j to zero

$$\left(\frac{\partial \mathscr{L}}{\partial n_i} \right)_{n_{k \neq i}, \underline{\chi}} = \mu_i - \sum_{j=1}^{M} A_{ij} \chi_i = 0 , \qquad (n_i > 0) , \tag{2.53}$$

and

$$\left(\frac{\partial \mathscr{L}}{\partial \chi_j} \right)_{\underline{n}, \chi_{l \neq j}} = b_j - \sum_{i=1}^{N} A_{ij} n_i = 0 . \tag{2.54}$$

Solving the set of $N + M$ equations of the forms (2.53) and (2.54), respectively, usually requires an iterative procedure and various numerical procedures have been suggested, e.g. [75–84]. It is important to note that the chemical potentials μ_i must be computable from the intensive state variables temperature T, pressure P and molar amounts $\underline{n}$.

A selection of established commercial products is available [63, 85–87] that can be obtained together with ready-to-use thermodynamic databases for the calculation of thermochemical equilibria and even phase diagrams. The downside of commercial software products is that for the user they are black-boxes, not giving any insight into their inner workings; the same holds for the offered thermodynamic databases. As will be shown later, commercial databases might not represent the best (or latest) available assessments of a thermochemical system and because of its intransparent documentation, users might not be able to comprehend the limits of the resulting thermodynamic predictions. Furthermore, linking commercial products to other software is often troublesome if possible at all. This may be because of technical hurdles

or licensing problems.
In the following chapter, a non-stoichiometric algorithm for the calculation of thermochemical equilibria of multi-component and multi-phase systems is developed in detail that can be coupled directly to a recently developed comprehensive LD-process model [27–30].

3 | Calculation of thermochemical equilibria in multi-component and multi-phase systems

In the following, the system of multi-variable transcendental equations that need to be solved simultaneously in order to calculate the equilibrium state of a complex chemical system is derived. Additionally, a numerical routine is elaborated in detail that is used to solve this system of equations and find the equilibrium state of multi-component and multi-phase slag systems. Moreover, subroutines for calculating the driving forces for the addition of new phases and convergence criteria are outlined.

3.1 Basic Definitions

As a first step in the mathematical analysis of thermochemical equilibria, it is necessary to begin with precise definitions of the used concepts:

- A **phase** is a structurally uniform region without any discontinuous jumps in its chemical and/or physical properties.
- Chemical **species** are aggregates of chemical elements characterized by their molecular formula, the specification of the phase in which they exist and, if needed, their molecular/crystal structure [65].
- The **components** of a thermochemical system are its smallest independent building blocks. Typically the chemical elements of the periodic table are chosen as components of thermochemical systems. In some cases, however, it is beneficial to define independent molecules as system components provided that they will not disintegrate under the conditions considered.
- Following the definition given in [88], **constituents** are defined as "independent entities to represent the constitution of a phase", e.g. substitutional atoms, interstitial atoms and vacancies in a crystal or basic oxides in liquid slags.

3.2 Minimization of Gibbs energy

As mentioned above, the Gibbs energy of a thermochemical system can be expressed as

$$G = \sum_{i}^{N} n_i \mu_i \ , \tag{3.1}$$

where μ_i is the chemical potential of species i. In a closed thermochemical system the mass is always contained. The conservation of mass can be expressed as

$$\sum_{i=1}^{N} A_{ij} n_i = b_j \ , \qquad j = 1, ..., M \ , \tag{3.2}$$

where A_{ij} is the stoichiometric coefficient of a species i containing component j, n_i is the amount of species i and b_j is the number of moles of component j in the system. The number of distinguishable components and the number of distinguishable species in the system are denoted M and N, respectively.
For multi-phase systems it is convenient to express the integral Gibbs energy G by means of the constituents of the individual phases. For a Φ-phase system the Gibbs energy of the system can be written as

$$G = \sum_{\phi=1}^{\Phi} \sum_{i=1}^{I_\phi} n_{\phi i} \mu_{\phi i} \ . \tag{3.3}$$

The constitution of each individual phase ϕ is represented by its corresponding constituents i of total number I_ϕ, where I_ϕ dependents on the individual phase. The chemical potentials of the constituent can be generally defined as

$$\mu_{\phi i} = \mu^{\circ}_{\phi i} + RT \ln a_{\phi i} \ . \tag{3.4}$$

In this relation $\mu^{\circ}_{\phi i}$ describes the chemical potential of the pure substance at temperature T; $a_{\phi i}$ is the chemical activity of the constituent i in the phase ϕ. Combining Eqs (3.3) and (3.4) gives

$$G = \sum_{\phi=1}^{\Phi} \sum_{i=1}^{I_\phi} n_{\phi i} \left(\mu^{\circ}_{\phi i} + RT \ln a_{\phi i} \right) \ . \tag{3.5}$$

Calculating the equilibrium composition of a multi-component, multi-phase system at a given temperature and pressure is achieved by minimizing the Gibbs energy of the system. For closed systems the Gibbs energy is minimized subject to mass

balance constraints. Moreover, only solutions with non-negative molar quantities $n_{\phi i}$ are considered physically meaningful. For ideal phases (e.g. ideal gases) or phases without miscibility gaps, the Gibbs energy function is a convex function. In contrast, silicate-containing melts (i.e. steelmaking slags) may exhibit miscibility gaps that can only be accounted for by means of non-convex segments of the Gibbs energy function. Hence, the minimization of the Gibbs energy of multi-phase systems with non-ideal phases can be classified as a constrained non-convex optimization problem and can be reformulated as

$$\text{minimize} \quad G = \sum_{\phi=1}^{\Phi} \sum_{i=1}^{I_\phi} n_{\phi i} \mu_{\phi i} \;, \tag{3.6a}$$

$$\text{s.t.} \quad \sum_{\phi=1}^{\Phi} \sum_{i=1}^{I_\phi} A_{ij}^{\phi} n_{\phi i} = b_j \;, \qquad j = 1, ..., M \;, \tag{3.6b}$$

$$n_{\phi i} \geq 0 \qquad i = 1, ..., I_\phi \;, \qquad \phi = 1, ..., \Phi \,. \tag{3.6c}$$

It is not always known a priori which phases are stable under the given conditions. Therefore, the set of equilibrium phases must be determined from all the phases that should reasonably be taken into account when minimizing the Gibbs energy. The Gibbs energy minimization problem can be addressed by formulating the Lagrangian $\mathscr{L}$ of the following form (see e.g. [65, 75, 76, 89])

$$\mathscr{L} = \sum_{\phi=1}^{\Phi} \sum_{i=1}^{I_\phi} n_{\phi i} \left(\mu_{\phi i}^{\circ} + RT \ln a_{\phi i} \right) - \sum_{j=1}^{M} \chi_j \left(\sum_{\phi=1}^{\Phi} \sum_{i=1}^{I_\phi} A_{ij}^{\phi} n_{\phi i} - b_j \right) - \sum_{\phi \in S_{\text{neq}}} \sum_{i=1}^{I_\phi} \lambda_{\phi i} n_{\phi i} \;, \tag{3.7}$$

where χ_j and $\lambda_{\phi i}$ are Lagrange multipliers and S_{neq} is the set of indices ϕ of all phases that are not considered in the current phase assemblage [90]. The chemical composition at the minimum of the Lagrangian is equivalent to the chemical composition at equilibrium.
By defining $\overline{\mathscr{L}} = \mathscr{L}/(RT)$, $\overline{\mu}_{\phi i}^{\circ} = \mu_{\phi i}^{\circ}/(RT)$, $\overline{\chi}_j = \chi_j/(RT)$ and $\overline{\lambda}_{\phi i} = \lambda_{\phi i}/(RT)$ the Lagrangian can be converted into its dimensionless form

$$\overline{\mathscr{L}} = \sum_{\phi=1}^{\Phi} \sum_{i=1}^{I_\phi} n_{\phi i} \left(\overline{\mu}_{\phi i}^{\circ} + \ln a_{\phi i} \right) - \sum_{j=1}^{M} \overline{\chi}_j \left(\sum_{\phi=1}^{\Phi} \sum_{i=1}^{I_\phi} A_{ij}^{\phi} n_{\phi i} - b_j \right) - \sum_{\phi \in S_{\text{neq}}} \sum_{i=1}^{I_\phi} \overline{\lambda}_{\phi i} n_{\phi i} \;. \tag{3.8}$$

The minimum of $\overline{\mathscr{L}}$ can be obtained by locating the critical points of the Lagrangian [75, 76, 90]:

$$\frac{\partial \overline{\mathscr{L}}}{\partial n_{\phi i}} = \overline{\mu}^{\circ}_{\phi i} + \ln a_{\phi i} + \sum_{k=1}^{I_\phi} n_{\phi k} \frac{\partial \ln a_{\phi k}}{\partial n_{\phi i}} - \sum_{j=1}^{M} \overline{\chi}_j A^{\phi}_{ij} = 0\,, \qquad \phi \notin S_{\text{neq}}\,, \tag{3.9}$$

$$\frac{\partial \overline{\mathscr{L}}}{\partial \overline{\chi}_j} = \sum_{\phi=1}^{\Phi} \sum_{i=1}^{N} A^{\phi}_{ij} n_{\phi i} - b_j = 0\,, \qquad j = 1, ..., M\,, \tag{3.10}$$

$$\frac{\partial \overline{\mathscr{L}}}{\partial \overline{\lambda}_{\phi i}} = n_{\phi i} = 0\,, \qquad \phi \in S_{\text{neq}}\,, \tag{3.11}$$

$$\frac{\partial \overline{\mathscr{L}}}{\partial n_{\phi i}} = \overline{\mu}^{\circ}_{\phi i} + \ln a_{\phi i} + \sum_{k=1}^{I_\phi} n_{\phi k} \frac{\partial \ln a_{\phi k}}{\partial n_{\phi i}} - \sum_{j=1}^{M} \overline{\chi}_j A^{\phi}_{ij} - \overline{\lambda}_{\phi i} = 0\,, \qquad \phi \in S_{\text{neq}}\,. \tag{3.12}$$

From the Gibbs-Duhem equation it follows that

$$\sum_{k=1}^{I_\phi} n_{\phi k} \frac{\partial \ln a_{\phi k}}{\partial n_{\phi i}} = 0\,. \tag{3.13}$$

The equilibrium of the system can be obtained by solving Eqs (3.9) and (3.10) in the following rewritten form:

$$\overline{\mu}^{\circ}_{\phi i} + \ln a_{\phi i} - \sum_{j=1}^{M} \overline{\chi}_j A^{\phi}_{ij} = 0, \qquad \phi \notin S_{\text{neq}} \tag{3.14}$$

$$\sum_{\phi=1}^{\Phi} \sum_{i=1}^{I_\phi} A^{\phi}_{ij} n_{\phi i} = b_j\,, \qquad j = 1, ..., M\,, \tag{3.15}$$

for the equilibrium phases ($\phi \notin S_{\text{neq}}$) while respecting the non-negativity constraints. From Eq (3.14) it can be seen that the Langrange multipliers $\overline{\chi}_j$ correspond to the chemical potentials of the components j defining the common tangent hyperplane of the thermochemical system. The non-linear set of equations comprised of Eq (3.14) and (3.15) is solved iteratively using a variation of the Newton-Raphson method. Following [65, 75, 90], the equations for calculating a new solution $n^{\aleph+1}_{\phi i}$ and $\overline{\chi}^{\aleph+1}_{j}$ from a previous estimate are outlined in the subsequent discussion; the subscript $\aleph$ indicates the current iteration step.

First, the chemical activities are revised for the solution phases in the system by separating them into an ideal term and an excess term:

$$\ln a_{\phi i} = \underbrace{\ln \frac{n_{\phi i}}{N_\phi}}_{\text{ideal}} + \underbrace{\ln \gamma_{\phi i}}_{\text{excess}} , \tag{3.16}$$

where $\gamma_{\phi i}$ denotes the rational activity coefficient of constituent i in phase ϕ and N_ϕ denotes the sum of the amounts $n_{\phi i}$ of all constituents contributing to the constitution of phase ϕ, i.e.

$$N_\phi = \sum_{i=1}^{I_\phi} n_{\phi i} \ . \tag{3.17}$$

The separation into an ideal and a non-ideal term allows the use of an algorithm for minimizing the Gibbs energy of ideal systems [65] by formally rewriting Eq (3.4) in its dimensionless form

$$\overline{\mu}_{\phi i} = \overline{\mu}^{\circ}_{\phi i} + \ln \frac{n_{\phi i}}{N_\phi} + \ln \gamma_{\phi i} = \overline{\mu}^{\circ\star}_{\phi i} + \ln \frac{n_{\phi i}}{N_\phi} \ . \tag{3.18}$$

Thus, at each iteration $\aleph$ the values from the ideal solution can be used for approximating the derivatives of the chemical potentials, while the non-ideal values are used for the computation of the chemical potentials (see e.g. [91]). For the calculation of a new solution for $n_{\phi i}^{\aleph+1}$ and $\overline{\chi}_j^{\aleph+1}$, the logarithmic term in Eq (3.18) is reformulated as

$$\ln \frac{n_{\phi i}^{\aleph+1}}{N_\phi^{\aleph+1}} = \ln \frac{n_{\phi i}^{\aleph+1}}{n_{\phi i}^{\aleph}} - \ln \frac{N_\phi^{\aleph+1}}{N_\phi^{\aleph}} + \ln \frac{n_{\phi i}^{\aleph}}{N_\phi^{\aleph}} \ . \tag{3.19}$$

The first two terms at the right hand side of Eq (3.19) are expanded into a Taylor series about an arbitrary point in the composition space [90]

$$\begin{aligned} &\ln \frac{n_{\phi i}^{\aleph+1}}{n_{\phi i}^{\aleph}} - \ln \frac{N_\phi^{\aleph+1}}{N_\phi^{\aleph}} = \\ &= \left(\frac{n_{\phi i}^{\aleph+1}}{n_{\phi i}^{\aleph}} - \frac{N_\phi^{\aleph+1}}{N_\phi^{\aleph}} \right) + \left(\frac{n_{\phi i}^{\aleph+1}}{n_{\phi i}^{\aleph}} - \frac{N_\phi^{\aleph+1}}{N_\phi^{\aleph}} \right) \left[1 - \frac{1}{2} \left(\frac{n_{\phi i}^{\aleph+1}}{n_{\phi i}^{\aleph}} + \frac{N_\phi^{\aleph+1}}{N_\phi^{\aleph}} \right) \right] + ... \end{aligned} \tag{3.20}$$

Cancelling the Taylor expansion Eq (3.20) after the first term and combining Eqs (3.14), (3.19) and (3.20) an updated value $n_{\phi i}^{\aleph+1}$ of the constituent amounts can be calculated

$$n_{\phi i}^{\aleph+1} = -\Psi_{\phi i}^{\aleph} + n_{\phi i}^{\aleph} \left(\frac{N_\phi^{\aleph+1}}{N_\phi^{\aleph}} + \sum_{j=1}^{M} \overline{\chi}_j^{\aleph+1} A_{ij}^{\phi} \right) \ , \tag{3.21}$$

with

$$\Psi_{\phi i}^{\aleph} = \left(\overline{\mu}_{\phi i}^{\circ} + \ln \gamma_{\phi i}^{\aleph} + \ln \frac{n_{\phi i}^{\aleph}}{N_{\phi}^{\aleph}} \right) n_{\phi i}^{\aleph} \, , \tag{3.22}$$

for every constituent i in solution phase ϕ. The rational activity coefficient $\gamma_{\phi i}^{\aleph+1}$ is approximated by its value from the previous iteration, thus

$$\ln\left(\gamma_{\phi i}^{\aleph+1}\right) \approx \ln\left(\gamma_{\phi i}^{\aleph}\right) . \tag{3.23}$$

The calculation of $\ln\left(\gamma_{\phi i}^{\aleph}\right)$ is executed by means of a separate procedure and is dependent on the model for the excess Gibbs energy of the individual phase (details are discussed in section 3.3). For every solution phase ϕ summation of Eq (3.21) over all constituents i gives

$$\sum_{j=1}^{M} \overline{\chi}_{j}^{\aleph+1} \sum_{i=1}^{I_\phi} n_{\phi i}^{\aleph} A_{ij}^{\phi} = \sum_{i=1}^{I_\phi} \Psi_{\phi i}^{\aleph} \, . \tag{3.24}$$

At every iteration step the mass balance must be satisfied, hence

$$b_j^{\aleph+1} - b_j = 0 \, , \qquad j = 1, ..., M \tag{3.25}$$

must hold. Here, $b_j^{\aleph+1}$ is the calculated amount of component j at iteration step $\aleph + 1$, and b_j is the actual amount of component j in the system (i.e. the input value). Combination of Eq (3.15) together with Eqs (3.21) and (3.25) results in M equations of the form

$$b_j = -\sum_{\phi=1}^{\Phi} \sum_{i=1}^{I_\phi} A_{ij}^{\phi} \Psi_{\phi i}^{\aleph} + \sum_{\phi=1}^{\Phi} \sum_{i=1}^{I_\phi} n_{\phi i}^{\aleph} A_{ij}^{\phi} \frac{N_{\phi}^{\aleph+1}}{N_{\phi}^{\aleph}} + \sum_{l=1}^{M} \overline{\chi}_{l}^{\aleph+1} \sum_{\phi=1}^{\Phi} \sum_{i=1}^{I_\phi} n_{\phi i}^{\aleph} A_{ij}^{\phi} A_{il}^{\phi} \, , \tag{3.26}$$

which can be reformulated to a more convenient form suggested by Eriksson [75]:

$$\sum_{l=1}^{M} \overline{\chi}_{l}^{\aleph+1} \sum_{\phi=1}^{\Phi} \sum_{i=1}^{I_\phi} n_{\phi i}^{\aleph} A_{ij}^{\phi} A_{il}^{\phi} + \sum_{\phi=1}^{\Phi} \left(\frac{N_{\phi}^{\aleph+1}}{N_{\phi}^{\aleph}} - 1 \right) \sum_{i=1}^{I_\phi} n_{\phi i}^{\aleph} A_{ij}^{\phi} = \sum_{\phi=1}^{\Phi} \sum_{i=1}^{I_\phi} A_{ij}^{\phi} (\Psi_{\phi i}^{\aleph} - n_{\phi i}^{\aleph}) + b_j \, . \tag{3.27}$$

If stoichiometric phases (i.e. pure compounds) are considered in the thermochemical system, the set of equations is slightly modified. Pure compounds are phases with only one constituent, hence their activity $a_\omega = 1$ and, thus, Eq (3.16) becomes zero for every stoichiometric phase ω

$$\ln a_\omega = 0 \, . \tag{3.28}$$

Furthermore, for stoichiometric phases Eq (3.24) simplifies to

$$\sum_{j=1}^{J} \overline{\chi}_j^{\aleph+1} A_{\omega j}^{\Omega} = \overline{\mu}_{\omega}^{\circ} \ , \tag{3.29}$$

where $A_{\omega j}^{\Omega}$ are the elements of the stoichiometric matrix of the pure compounds. If Ω distinguishable stoichiometric phases are present in the current set of considered phases in the phase assemblage, then Eq (3.27) is extended to

$$\sum_{l=1}^{M} \overline{\chi}_l^{\aleph+1} \sum_{\phi=1}^{\Phi} \sum_{i=1}^{I_\phi} n_{\phi i}^{\aleph} A_{ij}^{\phi} A_{il}^{\phi} + \sum_{\phi=1}^{\Phi} \left(\frac{N_\phi^{\aleph+1}}{N_\phi^{\aleph}} - 1 \right) \sum_{i=1}^{I_\phi} n_{\phi i}^{\aleph} A_{ij}^{\phi} + \sum_{\omega=1}^{\Omega} A_{\omega j}^{\Omega} n_{\omega}^{\aleph+1}$$
$$= \sum_{\phi=1}^{\Phi} \sum_{i=1}^{I_\phi} A_{ij}^{\phi} (\Psi_{\phi i}^{\aleph} - n_{\phi i}^{\aleph}) + b_j \ . \tag{3.30}$$

The expressions (3.24), (3.29) and (3.30) comprise a set of $(\Phi+\Omega+M)$ equations in the unknowns $\overline{\chi}_j^{\aleph+1}$, $\frac{N_\phi^{\aleph+1}}{N_\phi^{\aleph}} - 1$ and $n_{\omega}^{\aleph+1}$ that can be solved using a standard algorithm, details on the numerical solver are given below in section 3.2.4.

3.2.1 Non-negativity constraints

For each iteration step $\aleph$ the molar amounts $n_{\omega}^{\aleph+1}$ of the pure compounds in the system are directly obtained from solving Eqs (3.24), (3.30) and (3.29) simultaneously. If the number of moles $n_{\omega}^{\aleph+1}$ of a stoichiometric phase becomes less than or equal to zero during the iteration loop it is removed from the current phase assemblage, i.e. its phase index is added to the set S_{neq}. The amounts of the constituents $n_{\phi i}^{\aleph+1}$ of the solution phases ϕ are calculated in a second step using Eq (3.21). It is possible that one or more values of $n_{\phi i}^{\aleph+1}$ become negative during the minimization loop. In that case, the step length (the difference between previous and newly calculated values) has to be reduced retroactively. Eriksson [75] suggests the following procedure:
For all constituents where $n_{\phi i}^{\aleph+1} < 0$, an under-relaxation factor $\sigma_{\phi i}$ is introduced:

$$\sigma_{\phi i} = - \left(\frac{n_{\phi i}^{\aleph}}{n_{\phi i}^{\aleph+1} - n_{\phi i}^{\aleph}} \right) \ . \tag{3.31}$$

To ensure that all molar amounts become positive the minimum value of all $\sigma_{\phi i}$ must be determined and

$$n_{\phi i}^{\aleph+1,\text{new}} = n_{\phi i}^{\aleph} + 0.999 \cdot \sigma_{\min} \left(n_{\phi i}^{\aleph+1} - n_{\phi i}^{\aleph} \right) \ , \tag{3.32}$$

where the newly obtained values $n_{\phi i}^{\aleph+1,\text{new}}$ are used as estimates for the following iteration cycle. Due to this procedure, solution phases are not directly removed because of the non-negativity constraints. However, a solution phase is removed from the current phase assemblage if its amount is less than a sufficiently small limiting value, i.e. $\left(\sum_j^M b_j\right) \cdot 10^{-14}\,\text{mol}$, as suggested by Piro [92].

3.2.2 Driving force for addition of new phases to the system

During the iteration loop, it is possible that the Gibbs energy of a phase that is not considered in the current ($\aleph$) phase assemblage lies below the current common tangent hyperplane that is defined by the chemical potentials $\overline{\chi}_j^{\aleph}$ of the components j. In this case, the addition of the phase leads to a lower total Gibbs energy of the system. Such situations are detected using a single numerical value resulting from the evaluation of the tangent plane distance function Δf_ϕ

$$\Delta f_\phi = \sum_{i=1}^{I_\phi} \left(\overline{\mu}_{\phi i} - \sum_{j=1}^{M} A_{ij}^{\phi} \overline{\chi}_j^{\aleph} \right) \,. \tag{3.33}$$

A new phase may be added to the current phase assemblage during the iteration loop if its phase index $\phi \in S_{\text{neq}}$ and the tangent plane distance function Δf_ϕ becomes negative. For stoichiometric phases the tangent plane distance function Δf_ω is defined as

$$\Delta f_\omega = \overline{\mu}_\omega - \sum_{j=1}^{M} A_{\omega j}^{\omega} \overline{\chi}_j^{\aleph} \,. \tag{3.34}$$

In Fig 3.1 the addition step of a new phase β is represented graphically for a binary system. The common tangent hyperplane (in a binary system simply a 1D-tangent line) at iteration step $\aleph$ is indicated in red. During this iteration $\aleph$ only the α-phase is considered in the current phase assemblage. However, as the Gibbs energy of the β-phase (blue) lies below the current tangent plane (red), a negative value of $\Delta f_\beta^{\aleph}$ occurs. This indicates that the β-phase should be added to the system for the next iteration step $\aleph$+1. Hence, the tangent hyperplane at the following iteration step $\aleph$+1 needs to be adjusted in a way that the tangent plane distance function $\Delta f_\beta^{\aleph+1}$ becomes zero (shown in purple). The tangent plane distance function can thus be interpreted as a driving force for the addition of a new phase to the equilibrium system. Phases that are not part of the equilibrium state are defined by positive values of the tangent plane distance function whose numerical value indicates "how far" the stability limit of the individual phase is from the current thermodynamic state. While the addition of stoichiometric phases to the phase assemblage is straight forward, the addition of a new solution phase to the phase assemblage is more complicated. Before a new

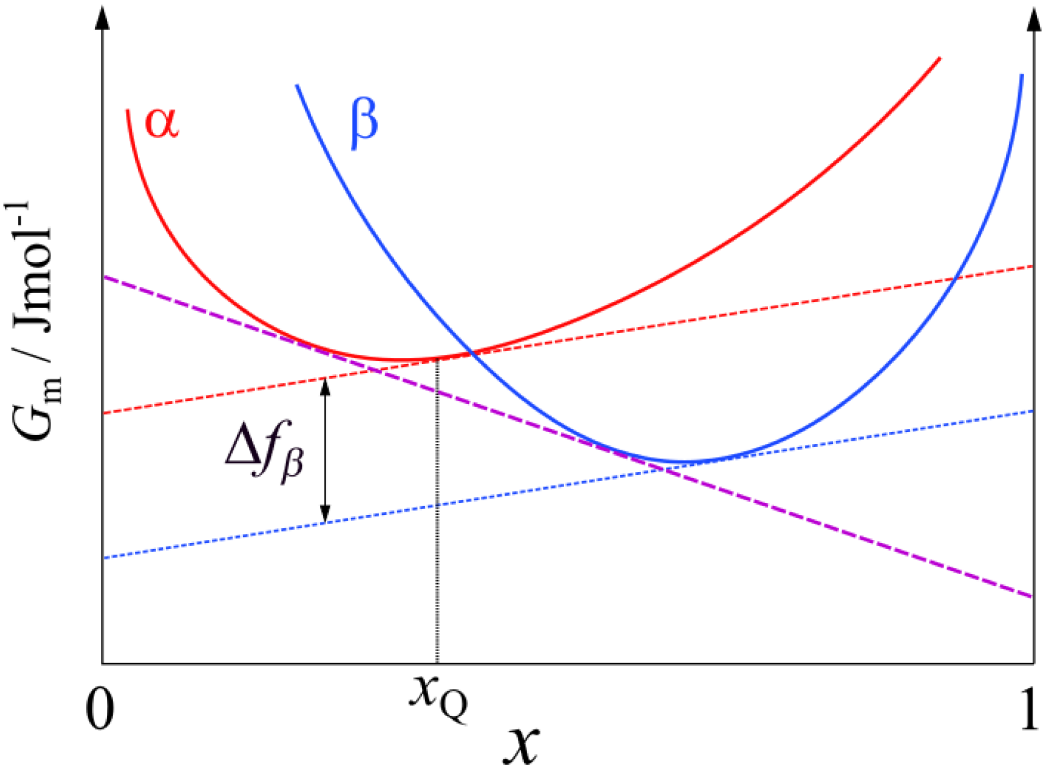

Figure 3.1: A graphical representation of a binary system with composition x_Q. At iteration ℵ only the α-phase is considered to be stable, the tangent hyperplane at iteration step ℵ is indicated via the red dashed line. As the β-phase lies below the red tangent hyperplane, it needs to be considered in the equilibrium phase assemblage. Thus, the tangent hyperplane at the following iteration step ℵ+1 needs to be adjusted in a way that the tangent plane distance function for β becomes zero (shown in purple).

solution phase can be added to the phase assemblage it must be determined at which constitution the new phase should be introduced to the phase assemblage.
Following Piro and Simunovich [93] the optimal composition of a newly introduced phase can be obtained by minimizing the tangent plane distance function subject to mass balance constraints, i.e.

$$\text{minimize } \Delta f_\phi = \sum_{i=1}^{I_\phi} \left(\overline{\mu}_{\phi i} - \sum_{j=1}^{M} A_{ij}^{\phi} \overline{\chi}_j \right) , \tag{3.35a}$$

$$\text{s. t. } \sum_{i=1}^{I_{\phi i}} x_{\phi i} = 1 . \tag{3.35b}$$

To not interfere with the numerical convergence too much, new phases are added to the phase assemblage with relatively small amounts, i.e. $\left(\sum_j^M b_j\right) \cdot 10^{-3}$ mol. At thermochemical equilibrium conditions the Gibbs phase rule holds; thus, a new phase is only introduced to the phase assemblage if the Gibbs phase rule allows for an additional phase

$$F = M - (\Phi + \Omega) + 2 , \tag{3.36}$$

where F is the number of independent variables that can be varied while maintaining the equilibrium state, M is the number of components and $(\Phi+\Omega)$ is the total number of solution and pure phases in equilibrium, respectively. Eq (3.36) determines the maximum amount of phases that can be present at equilibrium. At constant pressure and temperature the Gibbs phase rule becomes

$$F = M - (\Phi + \Omega) . \tag{3.37}$$

3.2.3 Convergence Criteria

The convergence of the iterative procedure is characterized by a single numerical value, the functional norm $\mathcal{F}^{\aleph}$ of the Lagrangian [92], and is defined as

$$\mathcal{F}^{\aleph} = \sqrt{\sum_{j=1}^{M} \left(\sum_{i=1}^{I_\phi} n_{\phi i}^{\aleph} A_{ij}^{\phi} + \sum_{\omega=1}^{\Omega} A_{\omega j}^{\Omega} n_{\omega}^{\aleph} - b_j \right)^2} + \sqrt{\sum_{i=1}^{I_\phi} \left(\overline{\mu}_{\phi i} - \sum_{j=1}^{M} A_{ij}^{\phi} \overline{\chi}_j^{\aleph} \right)^2 + \left(\overline{\mu}_{\omega} - \sum_{j=1}^{M} A_{\omega j}^{\omega} \overline{\chi}_j^{\aleph} \right)^2} \tag{3.38}$$

The functional norm $\mathcal{F}^{\aleph}$ is a measure of how well the equilibrium conditions are fulfilled at each iteration step $\aleph$. The iteration procedure stops when a value of $\mathcal{F}^{\aleph} \leq 10^{-10}$ is reached.

3.2.4 Outline of the iterative procedure

As the fundamentals of the Gibbs energy minimization algorithm are established, the main calculation loop for minimizing the Gibbs energy and finding the equilibrium values of $n_{\phi i}^{\text{equi}}$ and n_{ω}^{equi} can now be outlined:

1. For a given input (i.e, the M amounts b_j of the components, the temperature T, and the pressure P), a first guess about the stable phases that are present at the equilibrium state, their amounts and their constitution defined by $n_{\phi i}$ and n_{ω}, respectively, has to be made. In this first guess, the mass balance must be respected. In the case of metallurgical slags at temperatures above 1200°C the liquid phase is always considered. The first selection of phases together with their individual composition can be automatized using numerical routines [94, 95]. However, this feature is not implemented in this work.

2. The iteration loop starts with the determination of the rational activity coefficients $\gamma_{\phi i}$ using the modified quasi-chemical model for the liquid phase (see section 3.3).

3. The system of equations, consisting of (3.24), (3.29) and (3.30), is assembled and solved by means of the LAPACK routine "_gesv" [96] called via the numpy-Python interface [97] (numpy.linalg.solve). It is possible that during the iteration procedure the linear solver is not able to solve the system of equations in the case of a singular-matrix. In this case the system is solved (only for this iteration) using a least-squares procedure (numpy.linalg.lstsq) to overcome numerical difficulties. These cases are detected by the software and are reported at the end of the minimization loop.

4. The amounts $n_{\phi i}^{\aleph+1}$ of the constituents of the solution phases are calculated using Eq (3.21) and corrected in the case of negative $n_{\phi i}^{\aleph+1}$ by applying Eq (3.32).

5. Stoichiometric phases with a negative amount are removed from the set of considered phases. Solution phases with amounts smaller than $\left(\sum_j^M b_j\right) \cdot 10^{-14}\,\text{mol}$ are removed from the system. Due to convergence considerations only one phase is removed from the equilibrium phase assemblage per iteration step.

6. The driving force for the addition of a new phase is evaluated. A new phase is only allowed to be introduced to the current set of considered phases if its addition does not interfere with the Gibbs phase rule, Eq (3.36). Also, in order not to compromise convergence too much, only one phase is added per iteration. Also, adding a new phase is allowed only at every fifth iteration.

7. The convergence criterion Eq (3.38) is evaluated at the end of the iteration loop.

8. The iteration steps 2.-7. are run successively until convergence is reached.

The iteration procedure is represented graphically via a flowchart in Fig 3.2.

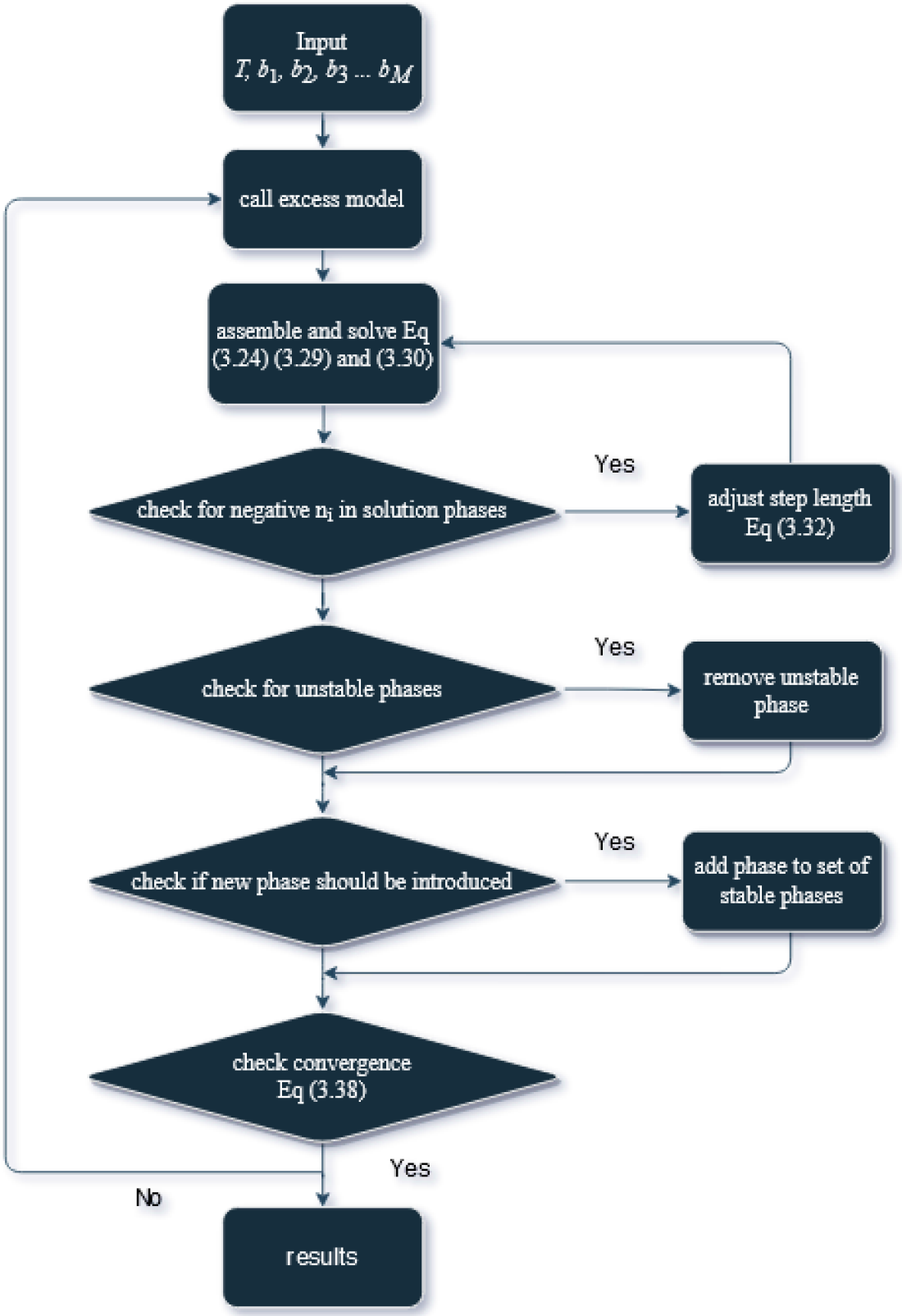

Figure 3.2: Flowchart representing the iteration procedure for calculating thermochemical equilibria.

3.3 Gibbs energy models

As mentioned above, the chemical potentials $\mu_{\phi i}$ of the individual constituents i comprising the phases ϕ considered in the Gibbs energy minimization routine need to be computable at every iteration step. Following the CALPHAD (see e.g. [64, 88]) approach to thermodynamics the Gibbs energy of a phase ϕ is generally expressed as

$$G_\phi = G_\phi^{\text{ref}} + G_\phi^{\text{id}} + G_\phi^{\text{ex}} + G_\phi^{\text{phys}} \ , \tag{3.39}$$

where G_ϕ^{ref} denotes the Gibbs energy of reference, G_ϕ^{id} is the contribution to the Gibbs energy stemming from the ideal configurational entropy; G_ϕ^{ex} and G_ϕ^{phys} are the excess Gibbs energy stemming from non-ideal interactions and the Gibbs energy contribution from significant physical effects (e.g. magnetic contributions), respectively. In the following discussion, the models used in this work providing expressions for the individual contributions to the Gibbs energy are presented. Finally, it will be shown how the chemical potentials $\mu_{\phi i}$ and especially the rational activity coefficients $\gamma_{\phi i}$ are calculated for the liquid phase.

3.3.1 Model for stoichiometric compounds

The Gibbs energies G_ω of the stoichiometric compounds are expressed via the usual temperature dependent function

$$G_\omega = C_1 + C_2 T + C_3 T \ln(T) + C_4 T^2 + C_5 T^3 + C_6 T^{-1} \ , \tag{3.40}$$

where C_1 contains the contribution to the Gibbs energy from the enthalpy of formation and the heat capacity of the individual compound, C_2 contains contributions of the absolute entropy and the heat capacity. The coefficients $C_3, ..., C_6$ are directly determined from the polynomial representing the heat capacities of the individual compounds. Similar equations are used to calculate the reference Gibbs energies for the constituents in the liquid phase.

3.3.2 Model for the liquid phase

In this work, the Gibbs energy of the liquid slag phase is derived by means of the modified quasi-chemical model [98–101], where atoms forming the liquid solution are distributed over the sites of a formal quasi-lattice. A characteristic of oxide melts is their tendency to short-range ordering. This holds especially for molten oxides containing considerable amounts of silica. The modified quasi-chemical model addresses short-range ordering by means of interactive nearest-neighbor pairs. It should be noted that the modified quasi-chemical model is far from being the only model

capable of describing the Gibbs energy of liquid oxides. Other models worth mentioning are the ionic two-sublattice model [102–104] and the non-ideal associate model [105–107]. Here, the modified quasi-chemical model is preferred since most of the assessments using this model are available for the thermodynamic system of interest. In this work the modified quasi-chemical model is used in the pair approximation for short-range ordering between species on a single sublattice. An extended approach to the modified quasi-chemical model is its development in a quadruplet approximation, which applies in particular to solutions with two sublattices. This extended model enables the simultaneous consideration of both inter- and intrasublattice short-range ordering phenomena [101,108]. The derivations necessary for implementing the modified quasi-chemical model in the quadruplet approximation in a thermodynamic software is provided in [109]. It is worth noting that in the case where one of the sublattices is either occupied by only a single species or remains empty, the equations of the quadruplet approximation are simplified to exactly match the equations of the single-sublattice modified quasi-chemical model.

Binary Solutions

In a binary solution - consisting of species A and B - pair-exchange reactions are defined in the form of

$$(\mathrm{A}-\mathrm{A})+(\mathrm{B}-\mathrm{B}) \rightleftharpoons 2\,(\mathrm{A}-\mathrm{B}) \qquad \Delta g_{\mathrm{AB}} = (\Delta h_{\mathrm{AB}} - T\Delta s_{\mathrm{AB}}) \ . \tag{3.41}$$

The non-configurational Gibbs energy change for the formation of two moles of $(\mathrm{A}-\mathrm{B})$ pairs is given by Δg_{AB} [98] and can be extended as a polynomial in the coordination equivalent fractions Y_{A} and Y_{B}. Pelton and Blander [98,110] suggest to expand Δg_{AB} as a polynomial in the coordination equivalent fractions in the following form

$$\Delta g_{\mathrm{AB}} = \Delta g^{\circ}_{\mathrm{AB}} + \sum_{p,q} L^{pq}_{\mathrm{AB}} Y^{p}_{\mathrm{A}} Y^{q}_{\mathrm{B}} \quad p \geq 0\,,\ q \geq 0\,, \tag{3.42}$$

where $\Delta g^{\circ}_{\mathrm{AB}}$ and L^{pq}_{AB} are (possibly temperature-dependent) model parameters that are fitted to experimental data and/or data from first-principles calculations. The more negative the Gibbs energy change Δg_{AB} is, the more favoured becomes the formation of $(\mathrm{A}-\mathrm{B})$ pairs. The phase becomes an ideal solution if the value of Δg_{AB} approaches zero.
It is convenient to introduce the nearest-neighbor pairs $(\mathrm{A}-\mathrm{A})$, $(\mathrm{B}-\mathrm{B})$ and $(\mathrm{A}-\mathrm{B})$ as "subordinated-constituents" of the solution phase. Following the definition given above, the species A and B qualify as the constituents of the phase, while the amounts of the nearest-neighbor pairs determine the (non-physical) structure of the phase on

a formal level. To relate the amounts of the nearest-neighbor pairs to the amounts of the species A and B the coordination numbers Z_A and Z_B are introduced. The coordination number Z_A represents formally the number of nearest-neighbor bonds of species A in the solution. However, in the context of the modified quasi-chemical model it should be viewed as a fitting parameter. The mass balances can then be written in the amounts of the nearest-neighbor pairs n_AA, n_BB:

$$Z_\mathrm{A} n_\mathrm{A} = 2n_\mathrm{AA} + n_\mathrm{AB} \;, \tag{3.43a}$$

$$Z_\mathrm{B} n_\mathrm{B} = 2n_\mathrm{BB} + n_\mathrm{AB} \;. \tag{3.43b}$$

The pair fractions are then defined as

$$x_\mathrm{AA} = \frac{n_\mathrm{AA}}{n_\mathrm{AA} + n_\mathrm{BB} + n_\mathrm{AB}} \;, \tag{3.44a}$$

$$x_\mathrm{BB} = \frac{n_\mathrm{BB}}{n_\mathrm{AA} + n_\mathrm{BB} + n_\mathrm{AB}} \;, \tag{3.44b}$$

$$x_\mathrm{AB} = \frac{n_\mathrm{AB}}{n_\mathrm{AA} + n_\mathrm{BB} + n_\mathrm{AB}} \;, \tag{3.44c}$$

and the overall mole fractions are

$$x_\mathrm{A} = \frac{n_\mathrm{A}}{n_\mathrm{A} + n_\mathrm{B}} \;, \tag{3.45a}$$

$$x_\mathrm{B} = \frac{n_\mathrm{B}}{n_\mathrm{A} + n_\mathrm{B}} \;. \tag{3.45b}$$

Additionally, the coordination equivalent fractions Y_A and Y_B are introduced

$$Y_\mathrm{A} = \frac{Z_\mathrm{A} n_\mathrm{A}}{Z_\mathrm{A} n_\mathrm{A} + Z_\mathrm{B} n_\mathrm{B}} = x_\mathrm{AA} + x_\mathrm{AB}/2 \;, \tag{3.46a}$$

$$Y_\mathrm{B} = \frac{Z_\mathrm{B} n_\mathrm{B}}{Z_\mathrm{A} n_\mathrm{A} + Z_\mathrm{B} n_\mathrm{B}} = x_\mathrm{BB} + x_\mathrm{AB}/2 \;. \tag{3.46b}$$

The introduction of the coordination equivalent fractions allows for more flexibility in terms of the composition of maximum ordering. The composition of maximum ordering in a solution is not necessarily $x_\mathrm{A} = x_\mathrm{B} = 0.5$; however, the parameters Z_A and Z_B can be chosen so that $Y_\mathrm{A} = Y_\mathrm{B} = 0.5$ corresponds to the composition at maximum ordering [110].

The Gibbs energy of the binary solution is given by

$$G_\phi = (n_\mathrm{A}\mu^\circ_\mathrm{A} + n_\mathrm{B}\mu^\circ_\mathrm{B}) - T\Delta S^\mathrm{config}_\phi + (n_\mathrm{AB}/2)\,\Delta g_\mathrm{AB} \;. \tag{3.47}$$

As no mathematical expression for the configurational entropy $\Delta S^\mathrm{config}_\phi$ in three dimensions is known, it is usually approximated by

$$\begin{aligned}\Delta S^\mathrm{config}_\phi = &-R\,(n_\mathrm{AA}\ln x_\mathrm{AA} + n_\mathrm{BB}\ln x_\mathrm{BB} + n_\mathrm{AB}\ln x_\mathrm{AB}) \\ &+ R\left(n_\mathrm{AA}\ln Y_\mathrm{A}^2 + n_\mathrm{BB}\ln Y_\mathrm{B}^2 + n_\mathrm{AB}\ln 2Y_\mathrm{A}Y_\mathrm{B}\right) - R\,(n_\mathrm{A}\ln x_\mathrm{A} + n_\mathrm{B}\ln x_\mathrm{B}) \;.\end{aligned} \tag{3.48}$$

The equilibrium values of the pair fractions of the nearest-neighbor pairs are derived by minimizing the internal Gibbs energy of the phase at constant overall composition

$$\left(\frac{\partial G_\phi}{\partial n_{\mathrm{AB}}}\right)_{n_{\mathrm{A}},n_{\mathrm{B}}} = 0 \,, \tag{3.49}$$

which results in the following relation

$$\frac{n_{\mathrm{AB}}^2}{n_{\mathrm{AA}} n_{\mathrm{BB}}} = 4\exp\left(-\frac{\Delta g_{\mathrm{AB}}}{RT}\right) \,. \tag{3.50}$$

Multi-component solutions

The mathematical relations for modelling the Gibbs energy of binary phases by means of the modified quasi-chemical model can be extended to multi-component solution phases in a straightforward manner:
In the following discussion of the generalized relations for multi-component phases, the constituents A, B, C,... are identified by integers $i = 1, 2, ..., I_\phi$, thus a formalism that is consistent with the notation used for the Gibbs energy minimization routine (see above) is elaborated. The mass balance for a species i in a multi-constituent solution phase ϕ is

$$Z_{\phi i} n_{\phi i} = n_{\phi ii} + \sum_{m=1}^{I_\phi} n_{\phi im} \,. \tag{3.51}$$

Pelton et al. [98, 99] introduced composition-dependent coordination numbers $Z_{\phi i}$ to adjust the composition of maximum short-range ordering in each sub-system:

$$Z_{\phi i} = \left[\frac{1}{n_{\phi ii} + \sum\limits_{m}^{I_\phi} n_{\phi im}} \left(\frac{n_{\phi ii}}{Z^i_{\phi ii}} + \sum_{m}^{I_\phi} \frac{n_{\phi im}}{Z^i_{\phi im}}\right)\right]^{-1} \,, \tag{3.52}$$

where $Z^i_{\phi im}$ is the value of $Z_{\phi i}$ when all nearest-neighbors of i are m. Additionally, the symmetric relation $Z^i_{\phi im} = Z^i_{\phi mi}$ holds and $Z^i_{\phi ii}$ becomes a major model parameter. The mole fraction x_i and the coordination equivalent fraction $Y_{\phi i}$ of species i are

$$x_{\phi i} = \frac{n_{\phi i}}{\sum\limits_{m=1}^{I_\phi} n_{\phi m}} \,, \tag{3.53}$$

and

$$Y_{\phi i} = \frac{Z_{\phi i} n_{\phi i}}{\sum_{m=1}^{I_\phi} Z_{\phi m} n_{\phi m}} = \frac{1}{2}\left(x_{\phi ii} + \sum_{m=1}^{I_\phi} x_{\phi im} \right) , \tag{3.54}$$

respectively. The pair fraction $x_{\phi ii}$ in a multi-component system is

$$x_{\phi ii} = \frac{n_{\phi ii}}{\sum_{n=1}^{I_\phi} \sum_{m=1}^{I_\phi} n_{\phi nm}} . \tag{3.55}$$

The Gibbs energy of the multi-component solution is

$$G_\phi = \sum_{i=1}^{I_\phi} n_{\phi i} \mu^\circ_{\phi i} - T\Delta S^{\text{config}}_\phi + \frac{1}{2}\left(\sum_{i=1}^{I_\phi} \sum_{m=1}^{I_\phi} n_{\phi im} \Delta g_{\phi im} - \sum_{i=1}^{I_\phi} n_{\phi ii} \Delta g_{\phi ii} \right) , \tag{3.56}$$

with

$$\Delta S^{\text{config}}_\phi = -R\left(\sum_{i=1}^{I_\phi} n_{\phi i} \ln(x_i) + \sum_{i=1}^{I_\phi} n_{\phi ii} \ln\left(\frac{x_{\phi ii}}{2Y^2_{\phi i}} \right) + \sum_{i=1}^{I_\phi} \sum_{m=1}^{I_\phi} n_{\phi im} \ln\left(\frac{x_{\phi im}}{2Y_{\phi i} Y_{\phi m}} \right) \right) . \tag{3.57}$$

The chemical potential $\mu_{\phi i}$ of species i is derived in the usual manner via

$$\mu_{\phi i} = \left(\frac{\partial G_\phi}{\partial n_{\phi i}} \right)_{n_{\phi m} \neq n_{\phi i}} = \frac{Z^i_{\phi ii}}{2} \left(\frac{\partial G_\phi}{\partial n_{\phi ii}} \right)_{n_{\phi im} \neq n_{\phi ii}} , \tag{3.58}$$

resulting in

$$\mu_{\phi i} = \mu^\circ_{\phi i} + RT \ln x_{\phi i} + \frac{Z^i_{\phi ii}}{2} \left(RT \ln\left(\frac{x_{\phi ii}}{Y^2_{\phi i}} \right) + \frac{\partial g^{\text{ex}}_\phi}{\partial n_{\phi ii}} \right) . \tag{3.59}$$

The excess term g^{ex}_ϕ is given as

$$g^{\text{ex}}_\phi = \frac{1}{2}\left(\sum_{i=1}^{I_\phi} \sum_{m=1}^{I_\phi} n_{\phi im} (\Delta g_{\phi im} - \Delta g^\circ_{\phi im}) \right) . \tag{3.60}$$

It is worth mentioning that $(\Delta g_{\phi im} - \Delta g^\circ_{\phi im})$ becomes zero in the case $i = m$.

3.3.3 Calculation of the partial excess terms

As discussed above, the chemical potential of a constituent i contributing to a phase ϕ can be generally expressed as

$$\mu_{\phi i} = \mu^{\circ}_{\phi i} + RT\left(\ln(x_{\phi i}) + \ln(\gamma_{\phi i})\right) \ . \tag{3.61}$$

From comparing this general expression with Eq (3.39) and Eq (3.59) one gets a new expression for the excess term that is used in the Gibbs energy minimization routine (more specifically in Eq (3.22)) outlined above

$$\frac{1}{RT}\frac{\partial G^{\mathrm{ex}}_{\phi}}{\partial n_{\phi i}} = \ln(\gamma_{\phi i}) = \frac{Z^{i}_{\phi ii}}{2}\left(\ln\left(\frac{x_{\phi ii}}{Y^{2}_{\phi i}}\right) + \frac{1}{RT}\frac{\partial g^{\mathrm{ex}}_{\phi}}{\partial n_{\phi ii}}\right) \ . \tag{3.62}$$

The key task is now to calculate the equilibrium pair fractions $x_{\phi ii}$ for a given overall composition specified by the mole fractions $x_{\phi i}$ of the constituents i in phase ϕ. For every possible pair-reaction of type (3.41) a pair-reaction constant $K_{\phi im}$ can be defined in the form of

$$K_{\phi im} = \frac{n^{2}_{\phi im}}{n_{\phi ii}n_{\phi mm}} = \frac{x^{2}_{\phi im}}{x_{\phi ii}x_{\phi mm}} = \exp\left(-\frac{\Delta g_{\phi im}}{RT}\right) \ . \tag{3.63}$$

However, as for $i = m$ the reaction constant becomes $K_{\phi im} = 1$ by definition, only π_{ϕ} independent equations of the form

$$x_{\phi im} - 2(x_{\phi ii}x_{\phi mm})^{\frac{1}{2}}\exp\left(-\frac{\Delta g_{\phi im}}{2RT}\right) = 0 \ , \tag{3.64}$$

need to be further considered, where

$$\pi_{\phi} = \frac{I_{\phi}!}{(I_{\phi}-2)!\,2} \ . \tag{3.65}$$

Additionally, I_{ϕ} mass balances in the form

$$x_{\phi ii} - Y_{\phi i} + \frac{1}{2}\sum_{m=1}^{I_{\phi}} x_{\phi im} - \frac{1}{2}x_{\phi ii} = 0 \ , \tag{3.66}$$

must be satisfied (see Eq (3.54)). Eq (3.64) and (3.66) result in a set of $(\pi_{\phi} + I_{\phi})$ non-linear equations in the unknowns $x_{\phi im}$. Negative values of $x_{\phi im}$ in Eq (3.64) result in complex roots, that have no physical meaning. Thus, to account for the non-negativity constraints a new set of substitution variables $\tilde{x}^{2}_{\phi im} = x_{\phi im}$ is introduced and inserted in Eqs (3.64) and (3.66), resulting in

$$\tilde{x}^{2}_{\phi im} - 2(\tilde{x}^{2}_{\phi ii}\tilde{x}_{\phi mm})^{\frac{1}{2}}\exp\left(-\frac{\Delta g_{\phi im}}{2RT}\right) = 0 \ , \tag{3.67}$$

and

$$\tilde{x}_{\phi ii} - Y_{\phi i} + \frac{1}{2}\sum_{m=1}^{I_\phi} \tilde{x}_{\phi im} - \frac{1}{2}\tilde{x}_{\phi ii} = 0\ . \tag{3.68}$$

This set of $(\pi_\phi + I_\phi)$ non-linear equations is solved by means of an iterative numerical procedure, i.e the well-established hybrid non-linear routine as suggested by Powell [111]. The equilibrium values of the pair fractions $x^{\text{equi}}_{\phi im}$ are obtained by means of back-substitution.
The equilibrium amounts $n^{\text{equi}}_{\phi im}$ of the individual pair fractions are calculated from combining Eqs (3.51) and (3.55). Finally, the partial excess terms $\ln(\gamma_{\phi i})$ are calculated using Eq (3.62).

3.3.4 Polynomial expansion of the Gibbs energy change for pair-reactions

As already stated above, the Gibbs energy change $\Delta g_{\phi im}$ for a nearest-pair interaction in a binary solution is usually expanded in a polynomial in the coordination equivalent fractions $Y_{\phi i}$ and $Y_{\phi m}$ of the form

$$\Delta g_{\phi im} = \Delta g^{\circ}_{\phi im} + \sum_{p,q} L^{pq}_{\phi im} Y^p_{\phi i} Y^q_{\phi m} \quad p \geq 0\,,\ q \geq 0\,. \tag{3.69}$$

If a third constituent n is introduced to the phase, interactions with the original constituents i and m must be considered and the polynomial expression for $\Delta g_{\phi im}$ must be modified (see [99, 108])

$$\Delta g_{\phi im} = \Delta g^{\circ}_{\phi im} + \sum_{p+q\geq 1} L^{pq}_{\phi im} \left(\frac{Y_{\phi i}}{Y_{\phi i}+Y_{\phi m}}\right)^p \left(\frac{Y_{\phi m}}{Y_{\phi i}+Y_{\phi m}}\right)^q + \sum_{p\geq 0,\ q\geq 0,\ r\geq 1} L^{pgr}_{\phi im(n)} \left(\frac{Y_{\phi i}}{Y_{\phi i}+Y_{\phi m}}\right)^p \left(\frac{Y_{\phi m}}{Y_{\phi i}+Y_{\phi m}}\right)^q Y^r_{\phi n}\ , \tag{3.70}$$

where the last term gives the contribution of the third constituent to the pair exchange energy $\Delta g_{\phi im}$. The model parameters $L^{pgr}_{\phi im(n)}$ are obtained from fitting the model function to experimental data. This extension ensures that $\Delta g_{\phi im}$ is constant at constant $Y_{\phi i}/Y_{\phi m}$ ratio (see Fig 3.3a). Since the three constituents of the solution are mathematically treated equally, this model is called symmetric. The symmetric model is convenient for solutions where the constituent-species behave "chemically similar". This vague term indicates already, that the selection of geometric models is generally subject to empirical experience. Alternatively, in the case when one constituent in the phase behaves "substantially different", the asymmetric model is applicable. The

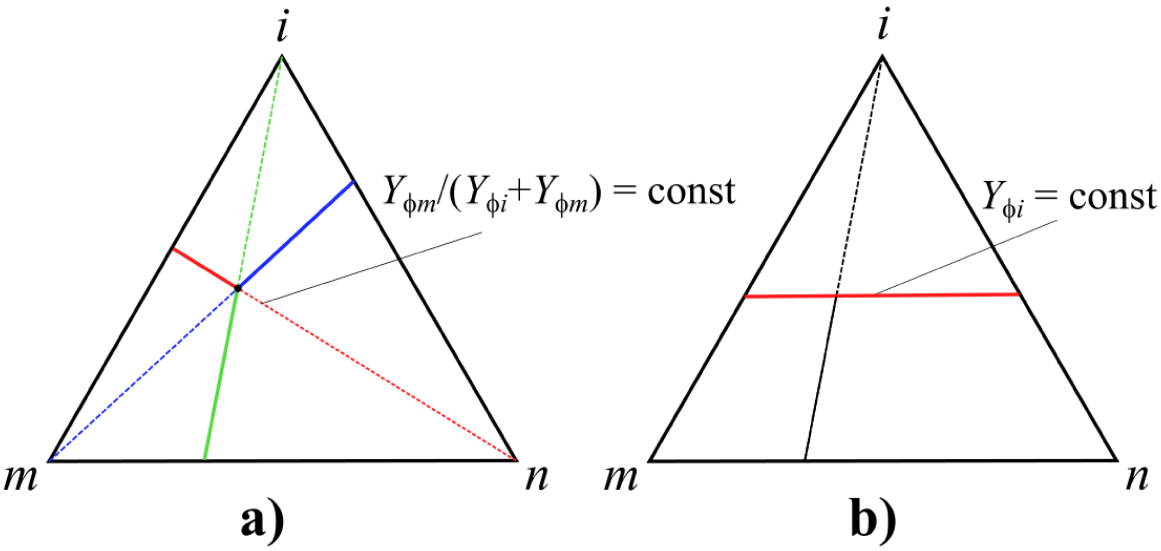

Figure 3.3: The symmetric (a) and asymmetric (b) model used for the extrapolation into ternary phases.

polynomial expansion for the Gibbs energy change for the pair exchange reaction with constituent i as the asymmetric species is given by

$$\Delta g_{\phi im} = \Delta g^{\circ}_{\phi im} + \sum_{p+q\geq 1} L^{pq}_{\phi im} Y^{p}_{\phi i} (1 - Y_{\phi i})^{q} + \sum_{p\geq 1,\, q\geq 0,\, r\geq 0} L^{pqr}_{\phi im(n)} Y^{p}_{\phi i} (1 - Y_{\phi i})^{q} \left(\frac{Y_{\phi n}}{Y_{\phi m} + Y_{\phi n}} \right)^{r} , \quad (3.71)$$

where the binary terms are constant along the red line in Fig (3.3b) and equal to their values at the $i - m$ binary line, i.e. $1 - Y_{\phi i} - Y_{\phi m} = 0$.

The geometrical models can be applied to extrapolate into higher order systems by defining

$$\zeta_{\phi im} = Y_{\phi i} + \sum_{n} Y_{\phi n} \quad (3.72)$$

where i-m-n represents a ternary sub-system, where m is the asymmetric constituent [108]. It is important to note that $\zeta_{\phi im} \neq \zeta_{\phi mi}$. In a multi-component phase the Gibbs energy change $\Delta g_{\phi im}$ for the pair-exchange reaction between i and m is written in

the following form:

$$\Delta g_{\phi im} = \underbrace{\Delta g^{\circ}_{\phi im}}_{\text{reference term}} + \underbrace{\sum_{p+q\geq 1} L^{pg}_{\phi i,} \left(\frac{\zeta_{\phi im}}{\zeta_{\phi im}+\zeta_{\phi mi}}\right)^{p} \left(\frac{\zeta_{\phi mi}}{\zeta_{\phi im}+\zeta_{\phi mi}}\right)^{q}}_{\text{binary term}} +$$

$$+ \underbrace{\sum_{p\geq 0,\, q\geq 0,\, r\geq 1} \left(\frac{\zeta_{\phi im}}{\zeta_{\phi im}+\zeta_{\phi mi}}\right)^{p} \left(\frac{\zeta_{\phi mi}}{\zeta_{\phi im}+\zeta_{\phi mi}}\right)^{q} \left(\sum_{n_{\mathrm{I}}} L^{pqr}_{\phi im(n_{\mathrm{I}})} Y_{\phi n_{\mathrm{I}}} (1-\zeta_{\phi im}-\zeta_{\phi mi})^{(r-1)}\right)}_{\text{contributions from ternaries, where } i\text{-}m\text{-}n_{\mathrm{I}} \text{ symmetric or } n_{\mathrm{I}} \text{ asymmetric}} +$$

$$+ \underbrace{\sum_{p\geq 0,\, q\geq 0,\, r\geq 1} \left(\frac{\zeta_{\phi im}}{\zeta_{\phi im}+\zeta_{\phi mi}}\right)^{p} \left(\frac{\zeta_{\phi mi}}{\zeta_{\phi im}+\zeta_{\phi mi}}\right)^{q} \left(\sum_{n_{\mathrm{II}}} L^{pqr}_{\phi im(n_{\mathrm{II}})} \left(\frac{Y_{\phi n_{\mathrm{II}}}}{\zeta_{\phi mi}}\right) \left(1-\left(\frac{Y_{\phi m}}{\zeta_{\phi mi}}\right)\right)^{(r-1)}\right)}_{\text{contributions from } i\text{-}m\text{-}n_{\mathrm{II}} \text{ ternaries, where } i \text{ asymmetric}} +$$

$$+ \underbrace{\sum_{p\geq 0,\, q\geq 0,\, r\geq 1} \left(\frac{\zeta_{\phi im}}{\zeta_{\phi im}+\zeta_{\phi mi}}\right)^{p} \left(\frac{\zeta_{\phi mi}}{\zeta_{\phi im}+\zeta_{\phi mi}}\right)^{q} \left(\sum_{n_{\mathrm{III}}} L^{pqr}_{\phi im(n_{\mathrm{III}})} \left(\frac{Y_{\phi n_{\mathrm{III}}}}{\zeta_{\phi im}}\right) \left(1-\left(\frac{Y_{\phi i}}{\zeta_{\phi im}}\right)\right)^{(r-1)}\right)}_{\text{contributions from } i\text{-}m\text{-}n_{\mathrm{III}} \text{ ternaries, where } m \text{ asymmetric}} . \tag{3.73}$$

In order to extend the polynomial representation of $\Delta g_{\phi im}$ properly it is, thus, necessary to assess all sub-binaries and sub-ternaries of the multi-component system beforehand. Usually, quaternary and higher-order interactions are neglected. On the one hand, this is due to experimental data becoming very scarce for quaternary systems and beyond. On the other hand, interactions become more and more improbable on the molecular level the higher the order of the interaction is. Therefore, their effect on the equilibrium states is considered to be relatively small.

The procedure for calculating the equilibrium state of multi-component, multi-phase systems is now established on a formal level. In the next section, the modelling approach for oxygen steelmaking slags is discussed in more detail. The elaboration of a thermodynamic database from literature sources is outlined in the following, which together with the Gibbs energy minimization routine allows the calculation of complex thermochemical equilibria with application to LD-steelmaking.

3.4 Modelling of the CaO-SiO$_2$-FeO$_x$-MgO-MnO-system

Slags resulting from the processing of low-phosphorus hot metal in oxygen steelmaking consist of up to 80% CaO, SiO$_2$ and FeO$_x$. Furthermore, depending on the case, significant contents of MgO, MnO, Al$_2$O$_3$, P$_2$O$_5$, Cr$_2$O$_3$ and S contribute to the

constitution of BOF slags [5]. In this work, the constitution of BOF slags during steelmaking is represented by the CaO-SiO_2-FeO_x-MgO-MnO-system. For the description of the thermodynamic conditions in steelmaking slags it is necessary to be able to calculate the Gibbs energies of all relevant phases in this system. To get a useful thermodynamic description of the CaO-SiO_2-FeO_x-MgO-MnO-system all unary, binary and ternary sub-systems need to be assessed following the CALPHAD approach outlined comprehensively by Lukas et al. [88]. The main focus in this work lies on the description of the liquid phase while the solid phases are modelled as stoichiometric phases; as will be shown later, the stoichiometric approximation for the solid phases is sufficient for modelling dissolution kinetics of oxide particles in many cases.
To get the total number π_{sub} of distinguishable binary or ternary sub-systems that need to be evaluated, combinatorical analysis can be used:

$$\pi_{\text{sub}} = \frac{M!}{(M - M_{\text{sub}})!\, M_{\text{sub}}!} \,, \tag{3.74}$$

where M is the number of components in the system, i.e. $M = 5$ in the quinary oxide system, and M_{sub} is the number of elements in the sub-systems, e.g. $M_{\text{sub}} = 2$ for the binary sub-systems, $M_{\text{sub}} = 3$ for the ternary sub-systems etc. Thus, to describe the quinary CaO-SiO_2-FeO-MgO-MnO system, 10 binary sub-systems as well as 10 ternaries have to be evaluated.

With reference to the geometric models discussed in section 3.3.4, all ternary subsystems containing SiO_2 are regarded "asymmetric", with SiO_2 as the asymmetric constituent. All ternary subsystems without SiO_2 are regarded "symmetric".
The equilibrium state of FeO_x-containing phases depends to a significant degree on the Fe^{3+}/Fe^{2+} ratio or equivalently the Fe_2O_3/FeO ratio, i.e. the oxidative state of iron in the phase. The oxidation ratio is highly dependent on temperature and the oxygen partial pressure p_{O_2} in the gas phase in equilibrium with the FeO_x-containing phase and has been investigated in various works, see e.g. [107, 112–120]. For oxygen steelmaking Schürmann et al. [115] argue for a steep gradient of p_{O_2} throughout the slag layer. According to their reasoning, the slag is in equilibrium with two different phases, i.e. the gas phase and the liquid iron. At the slag-gas interface, oxygen from the gas phase is in equilibrium with FeO and Fe_2O_3

$$2(\text{FeO}) + \frac{1}{2}\text{O}_2 \iff (\text{Fe}_2\text{O}_3)\,, \tag{3.75}$$

and an equilibrium constant can be defined

$$K_{\text{slag-gas}} = \frac{a_{(\text{Fe}_2\text{O}_3)}}{a^2_{(\text{FeO})} p^{\frac{1}{2}}_{\text{O}_2}} \,. \tag{3.76}$$

Schürmann et al. [115] assume that the oxygen partial pressure in the gas phase reaches about 1 atm and estimate the degree of oxidation at 1600°C from the Fe-FeO-Fe_2O_3 phase diagram, resulting in a Fe_2O_3/FeO-ratio of about 0.28 at the slag-gas interface.
On the opposite side of the slag layer, the slag is in equilibrium with liquid iron. Thus, the reaction equilibrium

$$(Fe_2O_3) + [Fe] \iff 3(FeO)\ , \tag{3.77}$$

defines the oxidation ratio of iron. According to Schürmann et al. [115], the oxygen partial pressure at the metal-slag interface is approximately $p_{O_2} = 10^{-8}$ atm and they derive an oxidation ratio of Fe_2O_3/FeO = 0.05 at 1600°C. Khadhraoui et al. [107] extend this discussion by arguing that carbon is oxidized from the liquid hot metal during the blow, resulting in a gas phase with a CO/CO_2 ratio of 90/10 with respect to gas volume. They calculate an oxygen partial pressure of p_{O_2}=$10^{-8.7}$ atm at 1600°C for the case where the slag is in equilibrium with a gas phase containing 90 vol% CO. Consequently, the gradient of the oxygen partial pressure throughout the slag layer becomes much flatter. Based on these results, the oxidation ratio is assumed to attain small values, i.e., Fe^{2+} is the dominant oxidation state of iron in the liquid slag during the BOF process. The influence of Fe^{3+} on the phase boundaries of the solid phases at oxygen steelmaking conditions is therefore assumed to be negligible. In addition, its effect on the viscosity of silicate slags is reported to be relatively small [121]. The interactions of Fe_2O_3 with the other constituents is thus neglected in this work. Analogous considerations can also be made for the different oxidation states of manganese. Thus, Mn^{+2} is assumed to be the dominant oxidative state. By neglecting the Fe_2O_3 and the Mn_2O_3 component in the liquid phase, the possibility to perform reliable calculations at higher oxygen partial pressures is prevented from the outset; however, by reducing the complexity of the thermodynamic model, the computation time can be significantly reduced, which brings advantages in terms of integration into a comprehensive LD-converter model.
Proceeding from the above, the state of the slag system is represented by the distribution of five components over the different phases. The amount of oxygen is assumed to be dependent on the amounts of the elements Ca, Si, Fe, Mn and Mg. As the amount of oxygen can not vary independently, the components of the system are chosen to be CaO, SiO_2, FeO, MgO and MnO. The constitution of the liquid phase is represented by the molar amounts (or equivalently the mole fractions) of CaO^{liquid}, SiO_2^{liquid}, FeO^{liquid}, MgO^{liquid} and MnO^{liquid} in the liquid. The superscripts indicate the difference between the components of the system and the constituents of the liquid phase. The stoichiometric matrix $\underline{\underline{A}}^{liquid}$ relating the molar amounts of the components of the system to the amounts of the constituents of the liquid phase is then

$$\underline{\underline{A}}^{\text{liquid}} = \begin{array}{c} \begin{array}{ccccc} \text{CaO} & \text{SiO}_2 & \text{FeO} & \text{MgO} & \text{MnO} \end{array} \\ \left(\begin{array}{ccccc} 1 & 0 & 0 & 0 & 0 \\ 0 & 1 & 0 & 0 & 0 \\ 0 & 0 & 1 & 0 & 0 \\ 0 & 0 & 0 & 1 & 0 \\ 0 & 0 & 0 & 0 & 1 \end{array} \right) \end{array} \begin{array}{c} \\ \text{CaO}^{\text{liquid}} \\ \text{SiO}_2^{\text{liquid}} \\ \text{FeO}^{\text{liquid}} \\ \text{MgO}^{\text{liquid}} \\ \text{MnO}^{\text{liquid}} \end{array}$$

The stoichiometric solid phases are related to the molar amounts of the system components by means of the matrix $\underline{\underline{A}}^{\Omega}$:

$$\underline{\underline{A}}^{\Omega} = \begin{array}{c} \begin{array}{ccccc} \text{CaO} & \text{SiO}_2 & \text{FeO} & \text{MgO} & \text{MnO} \end{array} \\ \left(\begin{array}{ccccc} 1 & 0 & 0 & 0 & 0 \\ 0 & 1 & 0 & 0 & 0 \\ 0 & 1 & 0 & 0 & 0 \\ 3 & 1 & 0 & 0 & 0 \\ 2 & 1 & 0 & 0 & 0 \\ 2 & 1 & 0 & 0 & 0 \\ 0 & 0 & 0 & 1 & 0 \\ 0 & 0 & 0 & 0 & 1 \\ 2 & 2 & 0 & 1 & 0 \\ 3 & 2 & 0 & 1 & 0 \\ 3 & 1 & 0 & 0 & 0 \\ 1 & 1 & 0 & 0 & 0 \\ 1 & 1 & 0 & 0 & 0 \\ 0 & 1 & 0 & 2 & 0 \\ 0 & 1 & 0 & 1 & 0 \\ 0 & 1 & 0 & 0 & 2 \\ 0 & 1 & 0 & 0 & 1 \end{array} \right) \end{array} \begin{array}{c} \\ \text{CaO}^{\text{lime}} \\ \text{SiO}_2^{\text{crist}} \\ \text{SiO}_2^{\text{tridym}} \\ \text{Ca}_3\text{SiO}_5^{\text{hatr}} \\ \text{Ca}_2\text{SiO}_4^{\text{C2S}\alpha'} \\ \text{Ca}_2\text{SiO}_4^{\text{C2S}\alpha} \\ \text{MgO}^{\text{peric}} \\ \text{MnO}^{\text{mang}} \\ \text{Ca}_2\text{MgSi}_2\text{O}_7^{\text{aker}} \\ \text{Ca}_3\text{MgSi}_2\text{O}_8^{\text{merw}} \\ \text{Ca}_3\text{Si}_2\text{O}_7^{\text{rank}} \\ \text{CaSiO}_3^{\text{woll}} \\ \text{CaSiO}_3^{\text{ps-woll}} \\ \text{Mg}_2\text{SiO}_4^{\text{forst}} \\ \text{MgSiO}_3^{\text{enst}} \\ \text{Mn}_2\text{SiO}_4^{\text{teph}} \\ \text{MnSiO}_3^{\text{rhod}} \end{array}$$

Although the list of selected solid phases is likely sufficient for the objectives of this work, it should be noted that in order to solve certain detailed questions in metallurgical processing, the current database would have to be considerably expanded. For a detailed thermochemical investigation of the dephosphorization behavior, for example, the introduction of solid solutions is inevitable, as the dephosphorization in the LD converter is largely based on the formation of silico-phosphate solid solutions (C2S-C3P, modelled as $(\text{Ca}^{2+}, \text{Mg}^{2+}, \text{Mn}^{2+})_3(\text{Ca}^{2+}, \text{Va})(\text{P}^{5+}, \text{Si}^{4+})_2(\text{O}^{2-})_8$). No independent assessment of the thermodynamic parameters is conducted in this work. Assessed parameters from various literature sources are "pieced" together to formulate a suitable thermodynamic database. This approach must be evaluated critically.

One must ensure that the thermodynamic parameters of the individual sources are compatible with each other to derive a useful thermodynamic description of the multi-component system, i.e. the same models must be used in the individual assessments (here the modified quasi-chemical model), the same unary-systems must be used in the assessments of the binary and ternary assessments and the same binary assessments must be used in the ternary assessments. Various assessments of CaO-SiO_2-FeO_x-MgO-MnO-system and its sub-systems using the modified quasi-chemical model are reported in the open literature, including [122–136]. Based on these assessments, the database used in this work is elaborated. The description of the unary systems follow Eq (3.40) and are taken from FactPS pure substance database.

The relevant data comprising the thermodynamic database are presented in the form of the following Tables listed in the Appendix: The Gibbs energy functions of the pure phases are listed in Table 2 and 3 in the Appendix. The binary interaction parameters $\Delta g^{\circ}_{\phi im}$ and $L^{pq}_{\phi im}$ can be found in Table 4 and the ternary interaction parameters $L^{pqr}_{\phi im(n)}$ are given in Table 5. The coordination numbers $Z^{i}_{\phi ii}$ are provided in Table 6.
In order to make an assessment of the usefulness of the developed software and database, equilibrium calculations and phase diagrams are calculated and compared to established software (i.e. FactSage [87]) and databases in the following discussion.

3.4.1 Software validation via equilibrium calculations in the CaO-SiO_2-FeO-MgO-MnO-system

The database is validated separately from the Gibbs energy minimization routine outlined above. For this purpose, the thermodynamic database is converted in a database format that can be used with FactSage 7.3. Now, equilibrium calculations can be performed using FactSage's "Equilib" module and phase diagrams can be drawn by means of FactSage's "Phase Diagram" module by coupling the database to those modules. Equilibrium calculations under various conditions are compared with results computed via FactSage to validate the Gibbs energy minimization routine. In Fig 3.4 the amounts of phases predicted by the software developed in this work and FactSage 7.3 are compared between 1200 °C and 1700°C at a global composition of 60 mol CaO, 25 mol SiO2, 15 mol FeO, 5 mol MgO and 5 mol MnO. The equilibrium phases that are predicted in this temperature interval include the liquid phase, lime (CaO), magnesia (MgO), dicalcium silicate (Ca_2SiO_4) and tricalcium silicate (Ca_3SiO_5). As the temperature rises, the amount of liquid phase increases continuously while the solid phases become unstable. The numerical results from the Gibbs energy minimization routine developed in this work agree with the calculations performed by means of the FactSage solver.

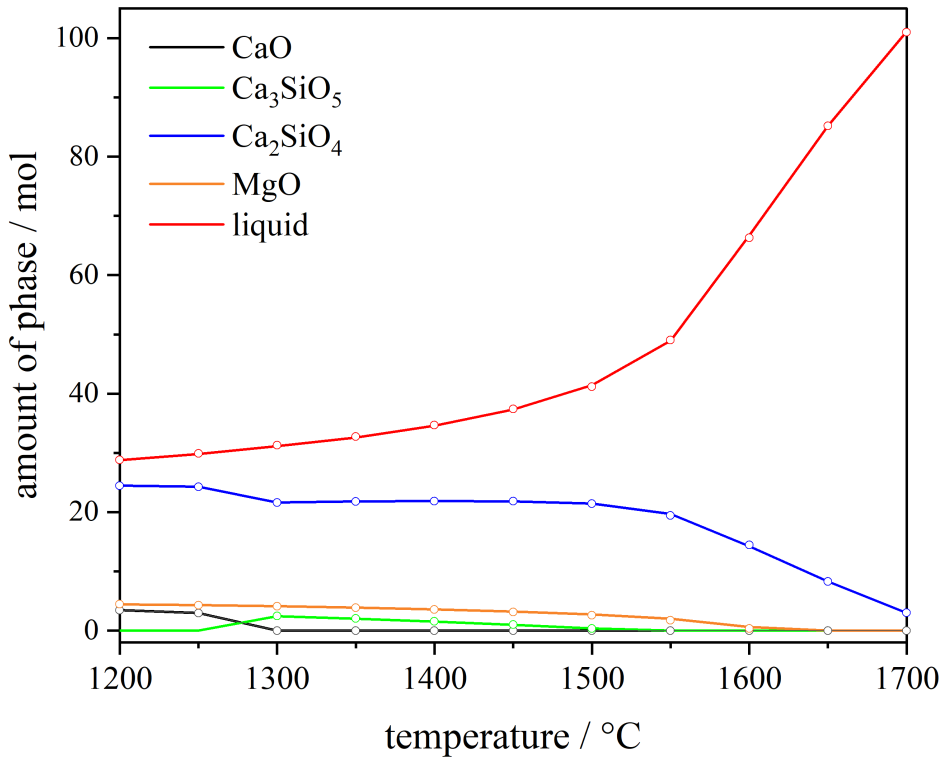

Figure 3.4: Equilibrium amounts of phases with rising temperature at global composition: 60 mol CaO, 25 mol SiO_2 15 mol FeO, 5 mol MgO and 5 mol MnO. The colored lines are calculated by means of FactSage 7.3 and the circles represent calculated by the software routine from this work.

3.4.2 Discussion of the CaO-SiO_2-FeO_x-system

The ternary CaO-SiO_2-FeO_x-system is the basic thermodynamic system in terms of BOF slags, especially for processing low-phosphorus hot metal, and is discussed in the following in the temperature and p_{O_2} ranges relevant for steelmaking practice. As outlined above, the oxidation ratio Fe_2O_3/FeO is assumed to be lower than 0.05 at low oxygen partial pressures ($p_{O_2} < 10^{-8}$ atm). Thus, FeO is considered to be the only relevant iron oxide in the liquid slag phase at steelmaking conditions.
Hidayat et al. [133] recently re-assessed the CaO-SiO_2-FeO_x-system incorporating "latest available experimental data" using the modified quasi-chemical model for modelling the Gibbs energy of the liquid phase. Their assessment is used in this

work and for the equilibrium calculations in systems containing this quasi-ternary system as a sub-set. However, some interaction parameters that are listed in their publication [133] are modified in this work using an unpublished optimization of these parameters that was provided by Denis Shishin, one of the co-workers of the original publication, see Table 5 in the Appendix.
The isothermal section of the CaO-SiO_2-FeO phase diagram at 1600°C is shown in Fig 3.5. As with all phase diagrams in this discussion, the CaO-SiO_2-FeO-system is presented with respect to the mass fractions of the individual components for convenience in terms of metallurgical practice. The results from this work are compared to results from the FToxid database (FactSage 7.3), a recent assessment from Khadhraoui et al. [107] and experimental data from Trömel et al. [137] and Görl et al. [138]. The calculated phase boundaries from this work and from FToxid are indicated in black and blue, respectively. The phase boundaries in the CaO-rich region from [107] are highlighted in via green dashed lines. There are significant differences observed in terms of the phase boundaries near the CaO-corner of the assessed phase diagrams. The calculations using FToxid predict a much smaller dicalcium silicate (C2S)+liquid region at 1600°C compared to the assessment of Khadhraoui et al. [107], the experimental data from [137] and this work. The solubility limit of CaO for moderate to low contents of FeO predicted by Khadhraoui et al. [107] agrees with the results from this work. The solubility limit of tricalcium silicate (C3S) however, is predicted to be higher in this work. The exact origin of the different deviations in the phase diagrams are difficult to trace, since the interaction parameters used in FToxid and from [107] are not published for commercial reasons. However, it is assumed that the database developed in this work from open sources is sufficient to make reasonable predictions in the CaO-SiO_2-FeO system under the conditions outlined above.
In the following the effect of temperature and the influence of the addition of MgO and MnO on the stability regions of relevant phases during steelmaking will be discussed.

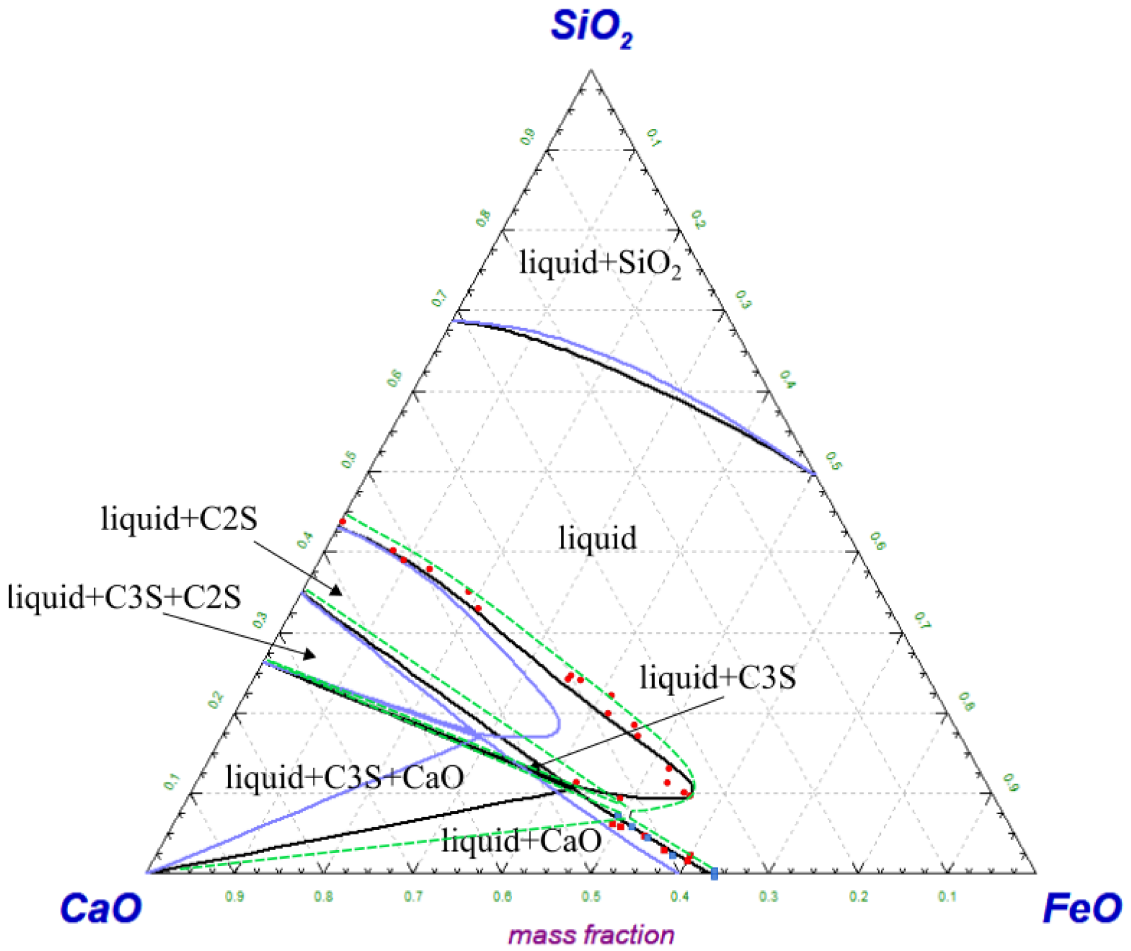

Figure 3.5: Isothermal section of the CaO-SiO_2-FeO phase diagram at 1600°C. The black lines indicate the results from this work, the blue lines are calculated by means of the FToxid database and the green, dashed lines corresponds to the results from Khadhraoui et al. [107]. The red and blue points are experimental values from Trömel et al. [137] and Görl et al. [138], respectively. The phase diagram using the database from this work and FToxid are calculated by means of FactSage 7.3. C2S denotes dicalcium silicate and C3S denotes tricalcium silicate.

Effect of temperature on the phase boundaries in the CaO-SiO_2-FeO_x-system at low oxygen partial pressures

During the first few minutes of the oxygen blow in the BOF process the temperature of the slag rises rapidly up to about 1500-1600°C [5]. From this fact it follows that

the dependence of the stability regions with temperature must be studied carefully to account for the needs of industrial steelmaking practice. Superimposed isothermal sections of the phase diagram of the ternary CaO-SiO_2-FeO-system are shown in Fig 3.6 at 1400°C, 1500°C and 1600°C, respectively. In can be observed that the wollastonite (CS) region decreases continuously with increasing temperature until it is no longer present at 1600°C. A similar statement can be made for the stability regions containing $Ca_3Si_2O_7$ (C3S2), which is already unstable at 1500°C. In steelmaking practice, the solubility line of C2S marks the conditions at which the slag becomes heterogeneous. The position of the C2S region in the temperature-composition space has a significant impact on the physical properties of slags (e.g. viscosity) or the ability of the slag to absorb phosphorus. It can be seen from Fig 3.6 that with rising temperature the liquid phase domain increases, while the liquid-Ca_2SiO_4 domain decreases significantly. The "nose" representing the solubility limit of dicalcium silicate (C2S) is shifted in the direction of the edge of the CaO-SiO_2-binary system. In contrast, the solubility line for lime is hardly influenced by temperature in the investigated temperature-range.

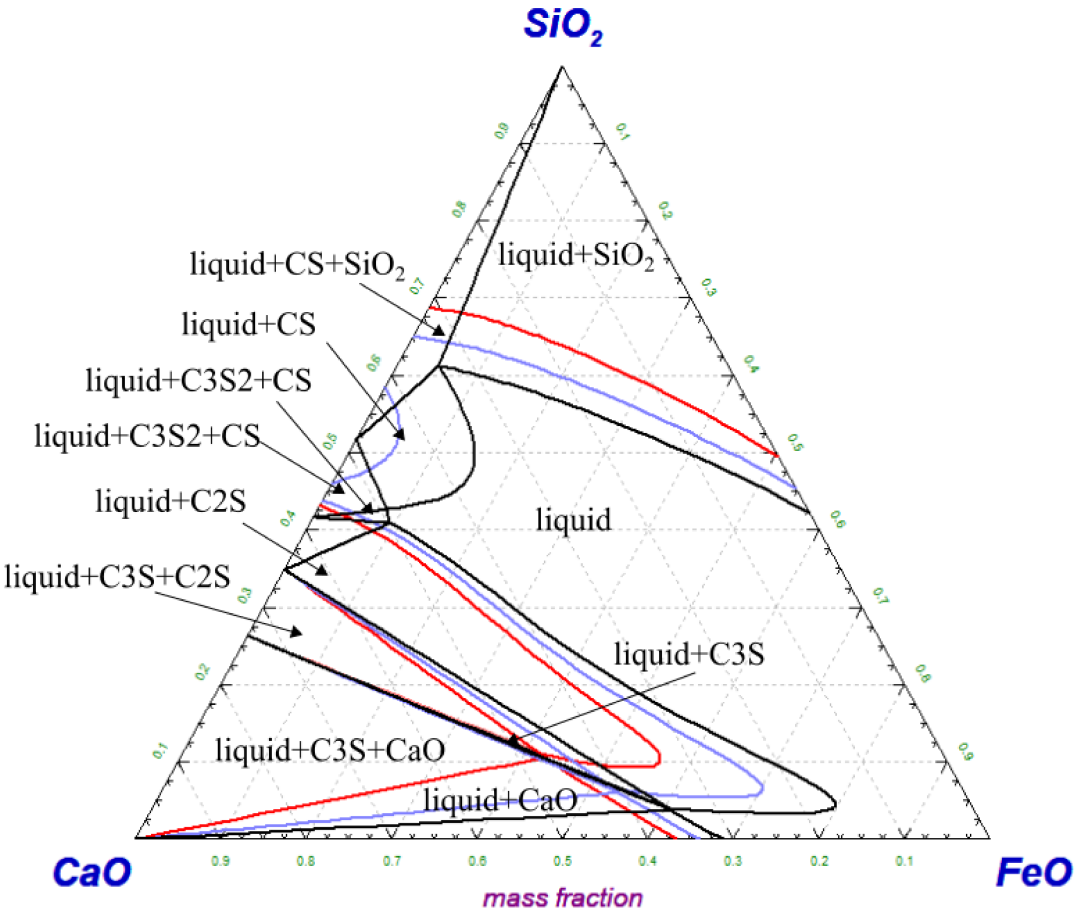

Figure 3.6: Ternary CaO-SiO_2-FeO phase diagram calculated from the developed thermodynamic database. The colored lines indicate the phase boundaries at different temperatures, i.e. black lines are at 1400°C, the blue lines at 1500°C and red lines at 1600°C. The isotherms are calculated by means of FactSage 7.3.

Effect of MgO addition in the CaO-SiO_2-FeO_x-MgO-system at low oxygen partial pressures

MgO enters BOF slags due to the wear of the refractory lining during the process or via feeding MgO-containing additives into the vessel. In terms of slag control, it is of particular interest to the steelmaker how the MgO content in the slag affects the location of the equilibrium phase regions in the multi-component system. To account for the interactions of MgO with the remaining constituents in the liquid slag, the assessments of [123, 124, 126, 127, 129, 130, 139, 140] are considered and relevant

interaction parameters are incorporated in the database, see Tables 4 and 5 in the Appendix, respectively.
The influence of MgO on the phase boundaries in the CaO-SiO_2-FeO-MgO system at 1500°C is shown in Fig 3.7. It should be noted that Fig 3.7 is not an isothermal section of a ternary phase diagram. To focus the discussion on the phase boundaries relevant for steelmaking some simplifications are made in this diagram, as not every equilibrium phase is indicated. Hence, interpretation of this figure should be done with great caution. However, some important conclusions can be drawn in terms of the slag phases relevant in BOF steelmaking. The C2S region is heavily influenced by the MgO content in the slag. Similar to the effect of rising temperatures the "C2S-nose" moves in the direction of the CaO-SiO_2 binary system. The solubility region of lime is hardly touched by the rising MgO-content in the system.

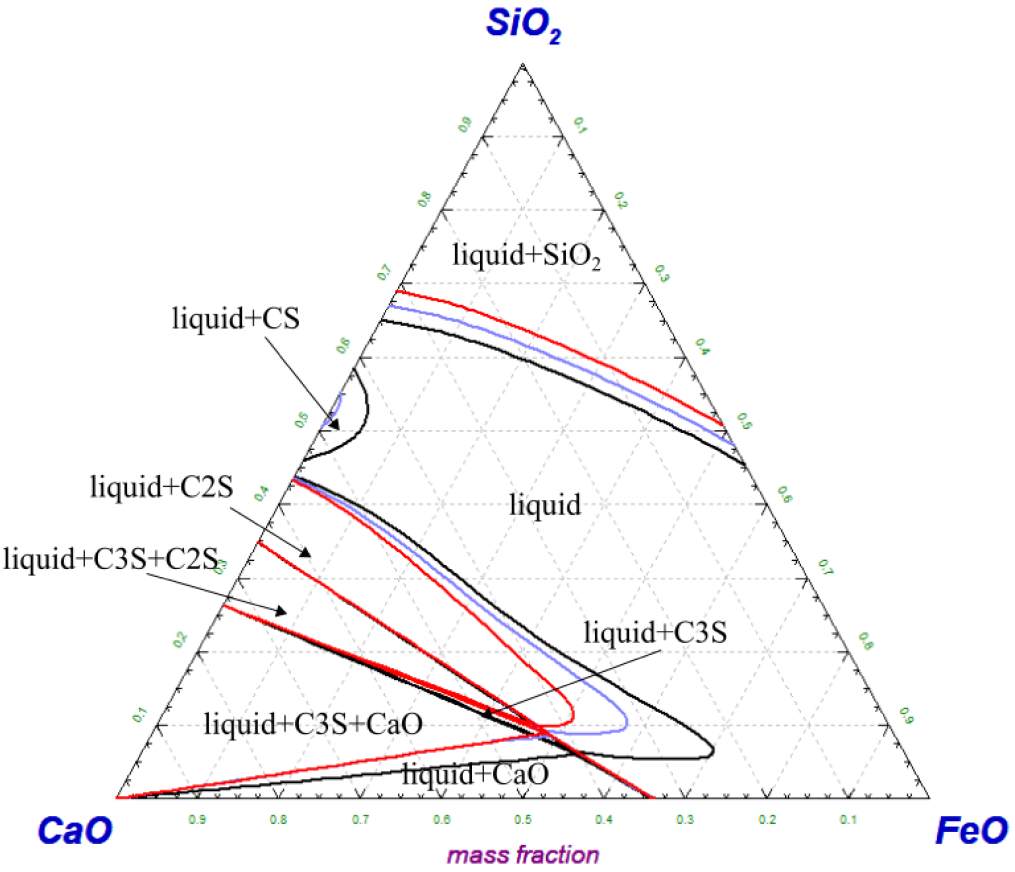

Figure 3.7: Characteristic zero phase fraction lines in the CaO-SiO_2-FeO-MgO system at 1500°C calculated from the developed thermodynamic database. The colored lines indicate the phase boundaries at different MgO contents, i.e. black lines are at $w_{\mathrm{MgO}} = 0$, the blue lines at $w_{\mathrm{MgO}} = 0.025$ and red lines at $w_{\mathrm{MgO}} = 0.05$. The zero phase fraction lines are calculated by means of FactSage 7.3.

Effect of MnO addition in the CaO-SiO_2-FeO_x-MnO-system at low partial pressures

The interactions of MnO with the other constituents in the liquid slag using the modified quasi-chemical model are investigated in various assessments [122, 125, 129, 130, 135, 136, 140]. The suggested parameters from these investigations for the database used in this work are listed in Tables 4 and 5 in the Appendix, respectively. The influence of MnO in steelmaking slags is discussed via zero phase fraction lines of the CaO-SiO_2-FeO_x-MnO-system at 1500°C and low oxygen partial pressures with rising

contents of MnO in Fig 3.8. Analogous to the above, Fig 3.8 does not represent an isothermal section of an actual ternary phase diagram, which is to be considered for the interpretation. Compared to MgO, the addition of MnO affects the position of the C2S phase field relatively little. This is qualitatively in accordance with the findings of Khadhraoui [141]. The pseudo-wollastonite field however, is strongly affected by the addition of MnO to the system and is already vanished at $w_{\mathrm{MnO}} = 0.05$. It is predicted that the effect of MnO addition to the CaO-SiO_2-FeO_x-MnO-system on the solubility limit of lime can be neglected.

Insights from thermochemical calculations for steelmaking practice

As shown, the Gibbs energy minimization routine coupled with a thermodynamic database allows for the calculation of equilibrium states and phases at steelmaking conditions. Various conclusions from these thermochemical equilibrium calculations can be drawn with relevance for steelmaking practice:

- The solubility limit of lime at steelmaking conditions is hardly affected by temperature or the addition of MgO or MnO. Thus, the driving force for diffusion limited dissolution of lime in BOF slags can barely be influenced by rising the temperature of the slag or by adding the above oxides to it. However, the dissolution rate of lime may nevertheless be enhanced by a lower slag viscosity and an increase in the diffusion coefficient at higher temperatures. In addition, the presence of certain oxides in the liquid phase can suppress the formation of intermediate boundary layers and thus alter the dissolution mechanism. This will be discussed in more detail in the next chapter.

- The saturation limit for the C2S phase is highly dependent on temperature and MgO content in the liquid slag. The behavior of the stability regions of silicate phases in the CaO corner of the CaO-SiO_2-FeO-MgO-MnO-system with varying temperature and composition are highly relevant for oxygen steelmaking practice. In the context of the dissolution of lime, a smaller stability range for C2S and C3S might enhance the dissolution kinetics of lime by suppressing the formation of intermediate boundary layers at the lime-liquid interface, see also e.g. [38, 47].

- With reference to Fig 3.5, it is interesting to see how the predictions of established databases that are regularly used in metallurgical practice, can differ so much from each other. Consequently, the responsible process metallurgist should always critically evaluate the applicability of open and, in particular, commercial (black box) databases.

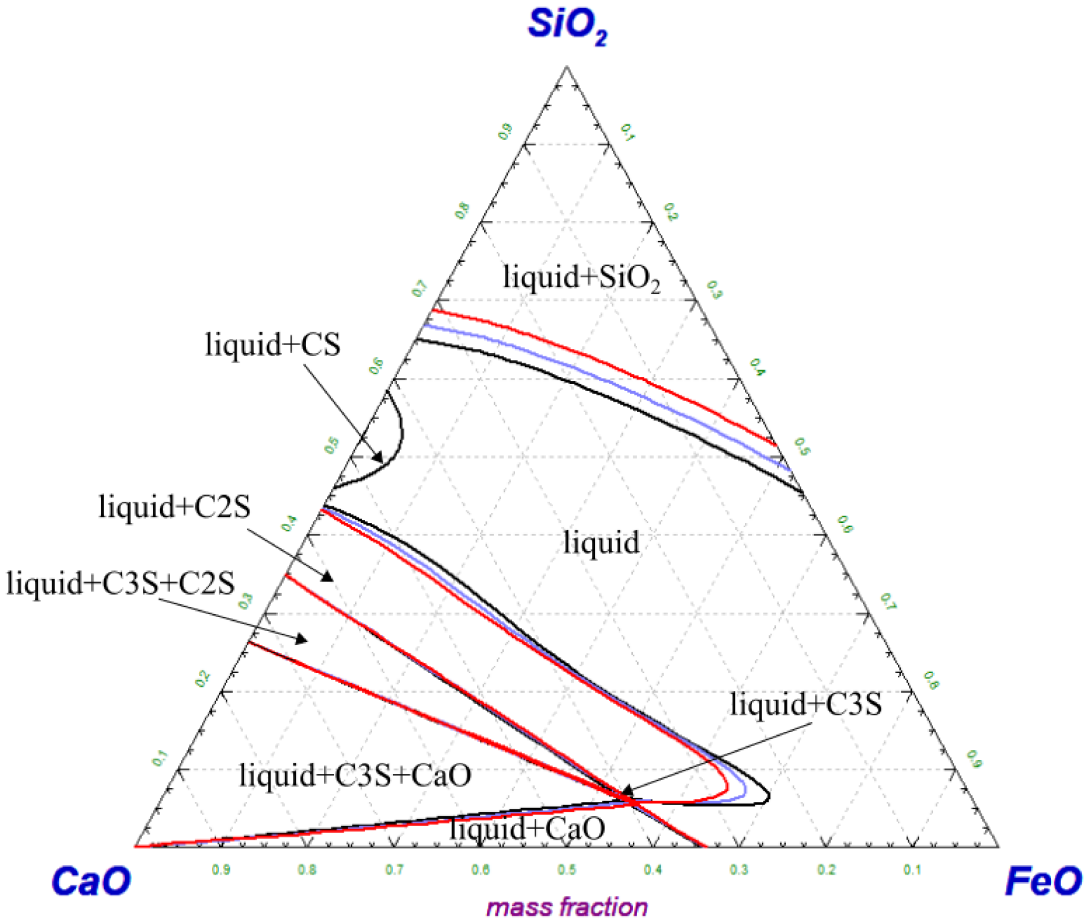

Figure 3.8: Characteristic zero phase fraction lines in the CaO-SiO_2-FeO-MnO system at 1500°C calculated from the developed thermodynamic database. The colored lines indicate the phase boundaries at different MnO contents, i.e. black lines are at $w_{\mathrm{MnO}} = 0$, the blue lines at $w_{\mathrm{MnO}} = 0.05$ and red lines at $w_{\mathrm{MnO}} = 0.1$. The zero phase fraction lines are calculated by means of FactSage 7.3.

- The Gibbs energy minimization software together with the database outlined above can be coupled easily to comprehensive LD-process models, allowing for fast evaluation of the equilibrium states and phases in multi-component slags during operation. Furthermore, the solubility limits of solid oxide phases (e.g. C2S, C3S, Lime or MgO) can be calculated. These values might serve as boundary and initial conditions for simulating the kinetics of solid-liquid phase transformations in steelmaking slags. This will be further investigated in great detail

in the next chapter.

4 Kinetics of solid-liquid phase transformations in metallurgical slags

As discussed previously, a software package is developed in this work to calculate thermodynamic functions and equilibrium phases. The numerical routines from this package are used as sub-routines for simulating the kinetics of solid/liquid phase transformations. The main code is based on the evolution equations of the kinetic parameters for a multi-component slag system with certain contact conditions valid at the sharp solid/liquid interface.

4.1 Thermodynamic contact conditions at the interface

The kinetics of (solid-liquid) phase transformations is strongly influenced by the thermodynamic contact conditions at the interface separating the parent and the new phase. In principle, two extreme cases are conceivable:

- On the one hand, local equilibrium at the interface, where diffusion in the bulk material determines the kinetics of the phase transformation.
- On the other hand, the transformation kinetics can be dominated by an interface reaction (see e.g., [142, 143]).

Assuming local equilibrium conditions at the (solid/liquid) interface is in many cases physically reasonable; this holds especially for processes occurring at high temperatures. The local equilibrium condition dictates the equality of the chemical potentials of all components j at the solid and the liquid sides of the (spherical) interface with position R:

$$\mu_{j,R}^{\text{liquid}} = \mu_{j,R}^{\text{solid}}, \qquad j = 1, .., M, \tag{4.1}$$

The chemical potentials at the interface can be derived by means of the Gibbs energy minimizing routine introduced in Chapter 3. The equilibrium concentrations or mole fractions are hereby also derived automatically and serve as boundary conditions for the resulting multi-component diffusion problem; details on the initial and boundary

conditions of the dissolution problem will be discussed later. It follows from the local-equilibrium condition at the interface, Eq (4.1), that there is no chemical driving force Δf_{chem} acting on the interface. Thus, the solid-liquid transformation is solely driven by diffusion in the liquid phase with the interface migrating due to mass balance considerations. Assuming that the molar volumes V_j of the diffusing species j are equal to the molar volume V_{M} the interface velocity becomes

$$v = \left(\sum_{j=1}^{M} [[J_j]] V_{\text{M}} \right) \left(\sum_{j=1}^{M} [[x_j]] \right)^{-1} , \tag{4.2}$$

where $[[J_j]]$ and $[[x_j]]$ denote the jumps of the fluxes and the jumps of the mole fractions of the substitutional species at the interface, respectively.

The situation is different for congruent phase transformations, where there are no non-zero concentration gradients occurring during the transformations process. In this case, the jump $[[\mu_{j,R}]]$ in the chemical potentials of the components j at the interface R leads to a chemical driving force $\Delta f_{\text{chem}} \neq 0$ promoting the motion of the interface. The thermodynamic contact conditions at a migrating sharp (i.e. infinitely thin) interface are derived from the thermodynamic extremal principle [144–146]. It follows from the thermodynamic extremal principle that the jumps of the chemical potentials at the interface are equal

$$[[\mu_{1,R}]] = [[\mu_{2,R}]] = ... = [[\mu_{M,R}]] , \tag{4.3}$$

Eq (4.3) is subsequently called the equal jump condition. The equal jump condition can also be interpreted as the minimum distance of the Gibbs energy of the unstable phase from the tangential hyperplane defining the equilibrium state. By applying the equal jump condition at the interface, the chemical driving force at the interface can be calculated

$$\Delta f_{\text{chem}} = \sum_{j=1}^{M} x_{j,R}^{0} [[\mu_{j,R}]] = [[\mu_{j,R}]] , \tag{4.4}$$

where $x_{j,R}^{0}$ are the mole fractions of the components at the parent side of the interface. The finite kinetics of the interfacial reaction are represented formally by an interface mobility M_{I}, that, in a first approximation, is only dependent on temperature. The temperature-dependence of the interface mobility can be described by an Arrhenius-like relation

$$M_{\text{I}} = M_{\text{I0}} \exp\left(-\frac{\Delta Q_{\text{M}}}{RT} \right) , \tag{4.5}$$

where M_{I0} is a pre-exponential factor and Q_{M} is the activation energy for the movement of the interface. The velocity v of the interface is then calculated from

$$v = \frac{M_{\text{I}}}{V_{\text{M}}} \Delta f_{\text{chem}} . \tag{4.6}$$

The thermodynamic contact conditions at the interface for the case of local equilibrium at the interface and the equal jump conditions at the interface can be interpreted graphically by means of $G_\mathrm{m} - x$ diagrams and are shown for the binary case in Fig 4.1.

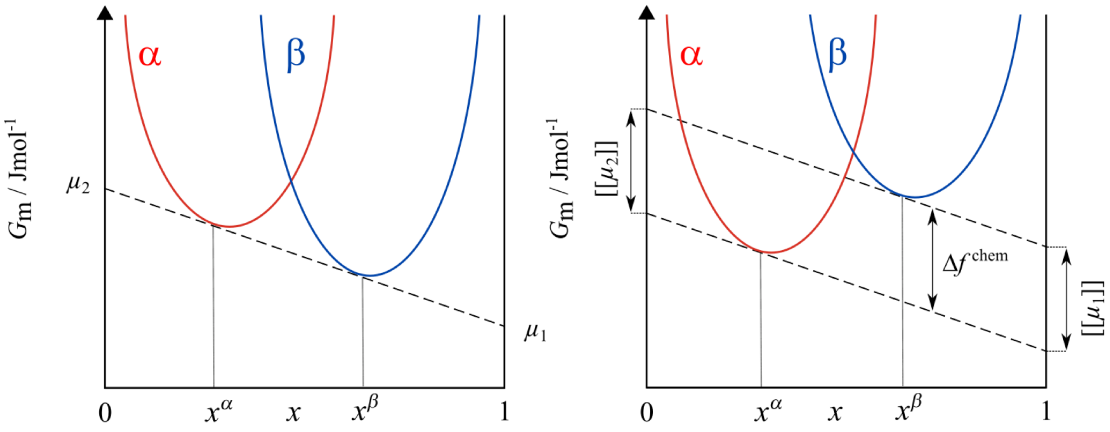

Figure 4.1: The thermodynamic contact conditions at the interface of two phases, α and β, in the binary case represented by means of $G_\mathrm{m} - x$ diagrams. The local equilibrium condition is depicted on the left, where the chemical potentials μ_1 and μ_2 of the components 1 and 2 are equal at both sides of the interface and are defined by the common tangent of the molar Gibbs energy functions G_m^α and G_m^β. The equal jump condition is shown right; the jumps of the chemical potentials $[[\mu_1]]$ and $[[\mu_2]]$ are equal and determine the chemical driving force Δf^chem at the interface.

4.2 Diffusive mass transport in multi-component systems

Contrary to what is often misleadingly stated, the field of applicability for thermodynamics is not limited to equilibrium calculations. A non-equilibrium system, i.e. the liquid phase and one or more solid phases, can be divided into an ensemble of elemental cells where local equilibrium is defined in each cell, see e.g. Kondepudi [147]. The local equilibrium concept allows for assigning thermodynamic variables (e.g. chemical potentials, temperatures) to every material volume in the system. For systems not too far from equilibrium, linear relations can be defined for the rates at which the individual elemental cells exchange energy and matter with their adjacent neighbors. A thermodynamic system that initially deviates from equilibrium evolves to a state of minimum Gibbs energy. The evolution equations are governed by maximum Gibbs energy dissipation in each time increment. From irreversible

(non-equilibrium) thermodynamics [148, 149] follow the linear relations between the rate of entropy production $\dot{\sigma}$, the thermodynamic fluxes J_j and their corresponding thermodynamic forces F_j :

$$\dot{\sigma} = -\frac{1}{T}\sum_{j=1}^{M} J_j F_j \,. \tag{4.7}$$

Following Balluffi et al. [149], the evolution equations for mass transport in a multi-component system are developed below.
The 1D-phenomenological equation relating the diffusive fluxes J_j in a multi-component phase to the thermodynamic driving forces, i.e. the gradients of the chemical potentials in z-direction, is

$$J_j = -\sum_{k=1}^{M-1} L_{jk}\frac{\partial \mu_k}{\partial z} \,, \tag{4.8}$$

where L_{jk} are the coefficients of the positive, semi-definite Onsager matrix. Hence, the Onsager coefficients follow the reciprocal relationship

$$L_{jk} = L_{kj} \,. \tag{4.9}$$

Assuming spatially constant molar volumes V_j the conservation requirement holds in the volume fixed frame [149, 150]:

$$\sum_{j=1}^{M} V_j J_j = 0 \,, \tag{4.10}$$

and

$$J_M = -\frac{1}{V_M}\sum_{j=1}^{M-1} V_j J_j \,. \tag{4.11}$$

Under isothermal and isobaric conditions the rate of entropy production $\dot{\sigma}$ can be related to multi-component diffusion. Thus, combining Eqs (4.7), (4.8), (4.10) and (4.11) gives

$$\dot{\sigma} = -\frac{1}{T}\sum_{j=1}^{M-1} J_i \frac{\partial}{\partial z}\left(\mu_j - \frac{V_j}{V_M}\mu_M\right) \,. \tag{4.12}$$

Comparing with Eq (4.7) reveals the thermodynamic force F_j as

$$F_j = -\left(\frac{\partial \mu_j}{\partial z} - \frac{V_j}{V_M}\frac{\partial \mu_M}{\partial z}\right) \,. \tag{4.13}$$

Thus, the diffusive flux J_j can be written as

$$J_j = \sum_{k=1}^{M-1} L_{jk} F_k = -\sum_{k=1}^{M-1} L_{jk} \left(\frac{\partial \mu_k}{\partial z} - \frac{V_k}{V_M} \frac{\partial \mu_M}{\partial z} \right) . \tag{4.14}$$

The local equilibrium concept allows for applicability of the Gibbs-Duhem relation, hence, only $M-1$ chemical potentials can change with composition independently

$$\frac{\partial \mu_j}{\partial z} = \sum_{k=1}^{M-1} \frac{\partial \mu_j}{\partial c_k} \frac{\partial c_k}{\partial z} . \tag{4.15}$$

where c_k is the concentration of k. Combining Eq (4.14) with (4.15) gives

$$J_j = -\sum_{l=1}^{M-1} L_{jl} \sum_{k=1}^{M-1} \left(\frac{\partial \mu_j}{\partial c_k} - \frac{V_j}{V_N} \frac{\partial \mu_N}{\partial c_k} \right) \frac{\partial c_k}{\partial z} . \tag{4.16}$$

Eq (4.16) is often expressed as

$$J_j = -\sum_{k=1}^{M-1} \tilde{D}_{jk} \frac{\partial c_k}{\partial z} , \tag{4.17}$$

with the interdiffusivities $\tilde{D}_{jk}$ defined as the sum of products of the Onsager coefficients L_{jl} and the thermodynamic factors

$$\tilde{D}_{jk} = \sum_{l=1}^{M-1} L_{jl} \underbrace{\left(\frac{\partial \mu_l}{\partial c_k} - \frac{V_l}{V_M} \frac{\partial \mu_M}{\partial c_k} \right)}_{\text{thermodynamic factors}} . \tag{4.18}$$

Finally, the partial differential equations for multi-component diffusion in 1D relate the evolution of the concentrations c_j in the system with the gradients of diffusive fluxes

$$\frac{\partial c_j}{\partial t} = -\frac{\partial}{\partial z} J_j = -\frac{\partial}{\partial z} \sum_{k=1}^{M-1} \left(\sum_{l=1}^{M-1} L_{jl} \left(\frac{\partial \mu_l}{\partial c_k} - \frac{V_l}{V_M} \frac{\partial \mu_M}{\partial c_k} \right) \frac{\partial c_k}{\partial z} \right) = -\frac{\partial}{\partial z} \sum_{k=1}^{M-1} \left(\tilde{D}_{jk} \frac{\partial c_k}{\partial z} \right) . \tag{4.19}$$

In many cases, the interdiffusivities are only available as constant values, i.e. their dependence on the gradients of the chemical potentials is neglected. In this case, Eq (4.19) is linearized:

$$\frac{\partial c_j}{\partial t} = -\sum_{k=1}^{M-1} \left(\tilde{D}_{jk} \frac{\partial^2 c_k}{\partial z^2} \right) . \tag{4.20}$$

For spherical systems Eq (4.20) becomes

$$\frac{\partial c_j}{\partial t} = -\sum_{k=1}^{M-1} \tilde{D}_{jk} \left(\frac{\partial^2 c_k}{\partial r^2} + \frac{2}{r} \frac{\partial c_k}{\partial r} \right) . \tag{4.21}$$

As the constitution of a phase is usually given in mole fractions x_j, it is convenient to formulate the diffusion equations in terms of the mole fractions

$$\frac{\partial x_j}{\partial t} = -\sum_{k=1}^{M-1} \tilde{D}_{jk} \left(\frac{\partial^2 x_k}{\partial r^2} + \frac{2}{r} \frac{\partial x_k}{\partial r} \right) . \tag{4.22}$$

4.3 Numerical integration of the evolution equations

The partial differential equation (4.22) is integrated numerically by means of a finite-difference central approximation with an uneven grid:

$$\left. \frac{\partial x_j}{\partial t} \right|_n \approx \frac{\Delta x_{j,n}}{\Delta t} = \sum_{k=1}^{M-1} \tilde{D}_{jk} \left(\frac{x_{k,n-1} + x_{k,n+1} - 2x_{k,n}}{\Delta r^2} + \frac{2}{R} \frac{x_{k,n+1} - x_{k,n-1}}{2\Delta r} \right) , \tag{4.23}$$

where $x_{j,n}$ denotes the mole fraction of species j at nodal point n ranging from 0 to p, Δ indicates the difference of a value to its direct neighbor in the time-space grid. A schematic representation of the one-dimensional mesh of the numerical model is shown in Fig 4.2. The mole fractions at the nodal point adjacent to the interface are treated by a parabola approximation (see Ogris and Gamsjäger [151])

$$x_j = a_{0,j} r^2 + a_{1,j} r + a_{2,j} , \tag{4.24}$$

where $a_{0,j}$, $a_{1,j}$ and $a_{2,}$ are the coefficients of the polynomial and follow from

$$a_{0,j} = \frac{x_{j,R}\Delta r + x_{j,R+2}\Delta r_R - x_{j,R+1}(\Delta r + \Delta r_R)}{\Delta r_R \Delta r (\Delta r_R + \Delta r)} , \tag{4.25}$$

$$a_{1,j} = \frac{x_{j,R+2}\Delta r_R^2 - x_{j,R}\Delta r^2 + x_{j,R+1}(\Delta r^2 - \Delta r_R^2)}{\Delta r_R \Delta r (\Delta r_R + \Delta r)} , \tag{4.26}$$

and

$$a_{2,j} = x_{j,R+1} . \tag{4.27}$$

The index R indicates the nodal point at the solid-liquid interface. From the position- and time dependence of the mole fractions $x_{j,R+1}$, $x_{j,R+2}$ and Δr_R follows that the coefficients $a_{0,j}$, $a_{1,j}$ and $a_{2,j}$ dependent on position and time. The time

derivative of the mole fraction $\dot{x}_{j,R+1}$ is obtained by inserting $a_{0,j}$ and $a_{1,j}$ from Eqs (4.25) and (4.26) into Eq (4.22):

$$\dot{x}_{j,R+1} \approx \Delta x_{j,R+1} = \sum_{k=1}^{M-1} 2a_{0,k}\tilde{D}_{jk}\left(3 + \frac{a_{1,k}}{a_{0,k}r_{R+1}}\right). \tag{4.28}$$

The mole fractions are updated each time-step via

$$x_{j,n}^{t+\Delta t} = x_{j,n} + \Delta x_{j,n}\ . \tag{4.29}$$

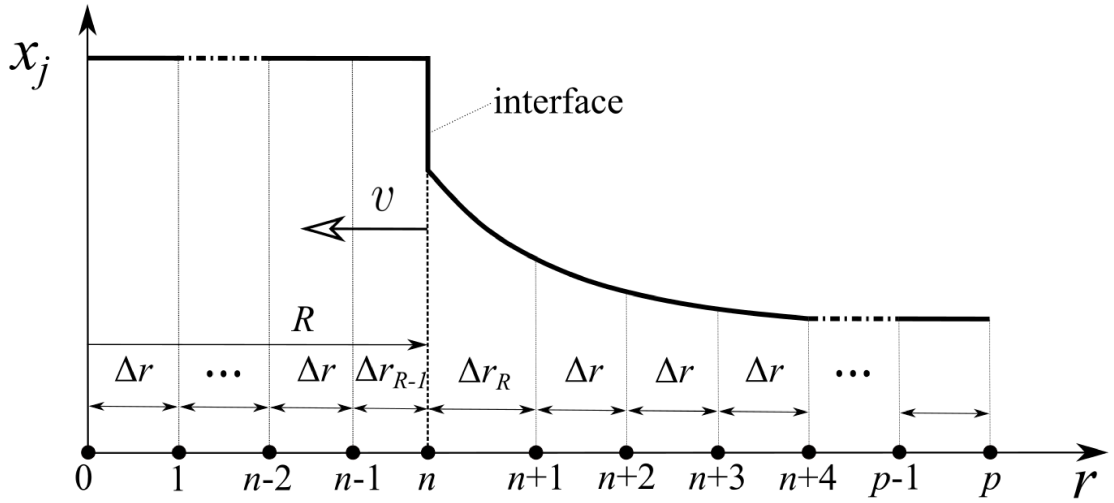

Figure 4.2: Schematic representation of the one-dimensional mesh of the numerical model [151].

The numerical solution of the diffusion equation is compared to the square root diffusivity method [44, 152, 153], an established mathematical tool to solve multi-component diffusion problems on the basis of superimposed error-functions

$$x_j(z,t) = x_{j,0} + |\Delta\underline{x}_0|\sum_{k=1}^{M-1} a_{jk}\mathrm{erfc}\left(\frac{z}{2e_k\sqrt{t}}\right)\ , \tag{4.30}$$

where $x_{j,0}$ denotes the initial mole fraction of species j at the right hand side of a diffusion couple and $|\Delta\underline{x}_0|$ is the magnitude of the initial composition-difference vector. The square roots of the eigenvalues of the interdiffusivity matrix $\underline{\underline{\tilde{D}}}$ are represented by e_k. The amplitudes a_{jk} of the individual error-functions are derived as discussed

in the following:
The interdiffusivity matrix $\underline{\underline{\tilde{D}}}$ is decomposed into

$$\underline{\underline{\tilde{D}}} = \underline{\underline{\tilde{D}_r}} \cdot \underline{\underline{\tilde{D}_r}} \,, \tag{4.31}$$

where $\underline{\underline{\tilde{D}_r}}$ is called the square-root diffusivity matrix and can be obtained by assembling the eigenvalues of $\underline{\underline{\tilde{D}}}$ into a diagonal matrix $\underline{\underline{E_D}}$ and the eigenvectors of $\underline{\underline{\tilde{D}}}$ into the transformation matrix $\underline{\underline{E}}$

$$\underline{\underline{\tilde{D}}}^{1/2} = \underline{\underline{E}} \cdot \underline{\underline{E_D}}^{1/2} \cdot \underline{\underline{E}}^{-1} = \underline{\underline{\tilde{D}_r}} \,. \tag{4.32}$$

The amplitudes a_{jk} of the complementary error functions are calculated from

$$a_{jk} = E_{jk}^{-1} \sum_{l=1}^{M-1} E_{kl} \cos \psi_l \,, \tag{4.33}$$

where ψ_l are the $M-1$ independent Euler angles between the initial composition difference vector $\Delta \underline{x}_0$ and the composition axes. To validate the numerical model, the mole fraction profiles calculated by the square root diffusivity method and the numerical solver used in this work are compared. The reference case - taken from [44] - represents a Ni-Cr-Al diffusion couple, with initial compositions $x_{\mathrm{Ni}} = 0.87$, $x_{\mathrm{Cr}} = 0.08$ and $x_{\mathrm{Al}} = 0.05$ on the left and $x_{\mathrm{Ni}} = 0.78$, $x_{\mathrm{Cr}} = 0.17$ and $x_{\mathrm{Al}} = 0.05$ on the right side of a planar interface positioned at 100 µm. The diffusion time is $t = 100$ s and the interdiffusivity matrix is

$$\underline{\underline{\tilde{D}}} = \begin{pmatrix} 22 & 7.6 \\ 7.8 & 12.6 \end{pmatrix} \cdot 10^{-15} \, [\mathrm{m^2 s^{-1}}] \,. \tag{4.34}$$

The composition profiles of Cr and Al are calculated by the numerical solver agree well with the concentration profiles predicted by the square root diffusivity method and are shown in Fig 4.3. It is interesting to note that due to the coupling of multicomponent diffusive fluxes, a concentration peak of aluminum is formed even though the initial concentration profile does not show any gradients. Effects of this kind can not be observed by means of effective-binary diffusion models.

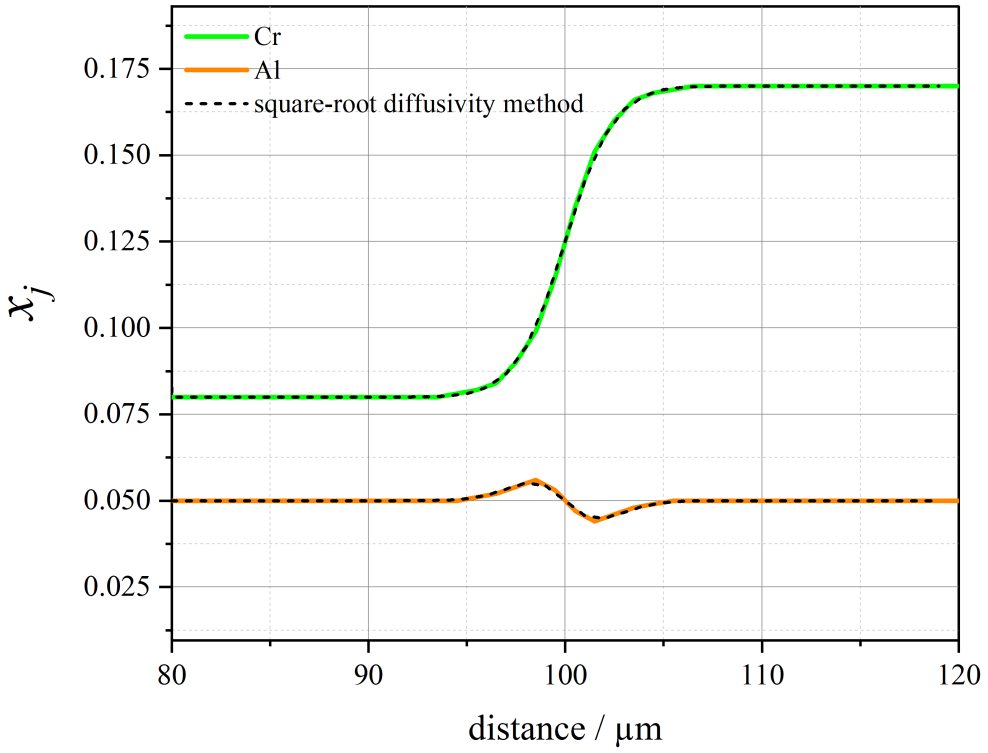

Figure 4.3: Comparison of multi-component mole fraction profiles calculated by means of the numerical model and the square root diffusivity method.

4.4 Choice of endmembers as diffusing species

In metallurgical slags, the nature of diffusing species is often not known. However, as will be shown in the following, the choice of the endmembers as diffusion species does not affect the applicability of the modelling approach presented above as long as the number of independent variables does not change [150]. For describing the molecular structure of slags two models can be destinguished, the ionic theory and the molecular theory [154]. The ionic theory takes into account the ionic character of liquid slags, whereas the molecular theory explains the properties of metallurgical slags via observable or virtual oxidic molecules. For the study of the effect of the choice of endmembers according to the ionic theory and the molecular theory, respectively, the entropy production rate for mass transport in both cases is investigated.
In the sense of the ionic theory, the diffusion ionic species are e.g. Ca^{2+}, Fe^{2+}, Mg^{2+},

Mn^{2+} and O^{2-}. Following [150], the rate of entropy production due to one-dimensional diffusion of ions in the liquid is given by

$$\dot{\sigma} = \frac{1}{T} \sum_{j=0}^{M} J_j \frac{\partial(\mu_j + q_j \mathscr{F} \psi_{\mathrm{el}})}{\partial z} \ , \tag{4.35}$$

where q_j is the electric charge of species j, $\mathscr{F}$ is the Faraday constant and ψ_{el} is the electric potential. The sum of the charge flux due to chemical diffusion is subject to the following condition

$$\sum_{j=0}^{M} q_j J_j = 0 \ . \tag{4.36}$$

Thus, the rate of entropy production in the case of ion diffusion, Eq (4.35), simplifies to

$$\dot{\sigma} = \frac{1}{T} \sum_{j=0}^{M} J_j \frac{\partial \mu_j}{\partial z} \ . \tag{4.37}$$

In the scope of the molecular theory, the structure of molten oxides is described by means of oxide molecules with chemical formula $\mathrm{M}_{a_j}\mathrm{O}_{b_j}$, where M is a metal, e.g. Ca, Fe, Si, Mg and Mn; a_j and b_j are stoichiometric coefficients. The ionic and the molecular species can be related via a dissociation relation of the following form

$$\mathrm{M}_{a_j}\mathrm{O}_{b_j} \iff a_j \mathrm{M}^{q_j} + b_j \mathrm{O}^{q_{\mathrm{O}}} \ . \tag{4.38}$$

As the molecules, $\mathrm{M}_{a_j}\mathrm{O}_{b_j}$, are neutrally charged, the following charge constraint applies

$$a_j q_j + b_j q_{\mathrm{O}} = 0 \ . \tag{4.39}$$

The fluxes $J_{\mathrm{M}_{a_j}\mathrm{O}_{b_j}}$ of the oxide molecules are eventually related to the fluxes of the corresponding ions

$$J_{\mathrm{M}_{a_j}\mathrm{O}_{b_j}} = J_j / a_j \ . \tag{4.40}$$

From local equilibrium follows the relation of the chemical potential of the molecule $\mathrm{M}_{a_j}\mathrm{O}_{b_j}$ to its comprising ions

$$\mu_{\mathrm{M}_{a_j}\mathrm{O}_{b_j}} = a_j \mu_j + b_j \mu_{\mathrm{O}} \tag{4.41}$$

The entropy production rate in the light of the molecular theory is thus

$$\dot{\sigma} = \frac{1}{T} \left(\sum_{j=1}^{M} J_{\mathrm{M}_{a_j}\mathrm{O}_{b_j}} \frac{\partial(\mu_{\mathrm{M}_{a_j}\mathrm{O}_{b_j}} - b_j \mu_{\mathrm{O}})}{\partial z} + J_{\mathrm{O}} \frac{\partial \mu_{\mathrm{O}}}{\partial z} \right) \ . \tag{4.42}$$

By using

$$b_j = -a_j \frac{q_j}{q_{\mathrm{O}}} \tag{4.43}$$

the entropy production rate becomes

$$\dot{\sigma} = \frac{1}{T} \left(\sum_{j=1}^{M} J_{\mathrm{M}_{a_j}\mathrm{O}_{b_j}} \frac{\partial \mu_{\mathrm{M}_{a_j}\mathrm{O}_{b_j}}}{\partial z} + \sum_{j=0}^{M} \frac{q_j}{q_{\mathrm{O}}} J_j \frac{\partial \mu_{\mathrm{O}}}{\partial z} \right) . \tag{4.44}$$

The second sum in Eq (4.44) becomes zero due to the zero net charge flux constraint, Eq (4.36). Hence,

$$\dot{\sigma} = \frac{1}{T} \left(\sum_{j=1}^{M} J_{\mathrm{M}_{a_j}\mathrm{O}_{b_j}} \frac{\partial \mu_{\mathrm{M}_{a_j}\mathrm{O}_{b_j}}}{\partial z} \right) . \tag{4.45}$$

Thus, it follows from local equilibrium that the choice of endmembers for diffusion has no effect on the entropy production rate as long as the number of independent variables is the same, see [150]. This result leads to the fact that the diffusive species can be freely chosen under the given conditions. In this work, the endmembers for diffusion in the liquid phase correspond to the constiutuents selected to describe the thermodynamic state of the liquid phase, e.g. CaO, SiO_2 or FeO (see Section 3.4).

4.5 Boundary and initial conditions

The dissolution kinetics of oxide particles is investigated in a 1D spherical system with r as the spatial coordinate. The dissolving particle with a time dependent radius $R(t)$ is surrounded by a liquid phase with thickness $S(t)$. Here, $S(t)$ also determines the boundary of the system. The thickness of the liquid phase is dependent on time; as the radius $R(t)$ shrinks, $S(t)$ becomes larger. However, the sum $S(t) + R(t)$ remains constant. A scheme of the geometric conditions of a spherical dissolving particle is shown in Fig 4.4.

Assuming that diffusion occurs only in the liquid phase and no material can leave the system at the system boundary $R + S$, the boundary conditions at $r = R$ and $r = R + S$ are given by

$$x_j \Big|_{(r=R,\,t)} = x_{j,R}^{\mathrm{liquid}} , \tag{4.46}$$

and

$$\frac{\partial x_j}{\partial r} \Big|_{(r=R+S,\,t)} = 0 , \tag{4.47}$$

respectively. The mole fraction $x_{j,R}^{\mathrm{liquid}}$ at the liquid side of the interface is determined by the thermodynamic contact conditions at the interface. It is calculated by means

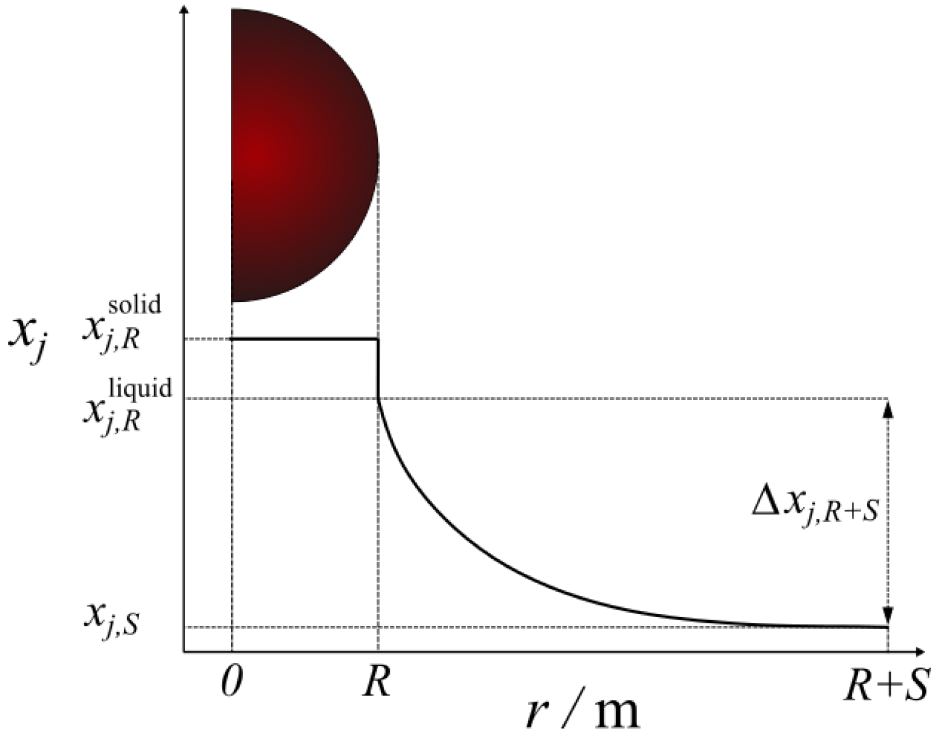

Figure 4.4: Schematic representation of the geometric conditions of the dissolving particle.

of Gibbs energy minimization, i.e. local equilibrium at the interface, Eq (4.1), or from the equal jump condition, Eq (4.3), respectively. Initially ($t = 0$), the mole fractions x_j in the liquid are evenly distributed

$$x_j\Big|_{(r>R,\,t=0)} = x_{j,0} \ , \tag{4.48}$$

where $x_{j,0}$ denotes the mole fractions describing the initial composition of the liquid phase. Again, the composition at the liquid side of the interface at the start of the dissolution process is given by

$$x_j\Big|_{(r=R,\,t=0)} = x_{j,R}^{\text{liquid}} \ . \tag{4.49}$$

4.6 Convective contributions to mass transfer

The dissolution kinetics of particles that are unstable in liquid matrices are generally subject to convective flows of various origins. Convective flows may be produced by

mechanical or electromagnetic stirring, an uneven temperature distribution, density gradients in the liquid or capillary effects. In general, convective flow enhances mass transport and, therefore, reduces the total dissolution time. In engineering, dimensionless quantities are often used to estimate the physical reality of heat and mass transport problems. The Péclet number Pe is a dimensionless number that relates the convective transport rate to the diffusive transport rate. It is a comprehensible quantity to reveal the physical conditions of mass transport for a given situation. The Péclet number for studying diffusion-convection problems is defined as

$$Pe = \frac{2\,R\,u_c}{D}\ , \tag{4.50}$$

where u_c is the characteristic velocity of the convective flow field, see e.g. [155]. High Péclet numbers indicate that the mass transport is dominated by convective flows and low values of Pe signify a diffusive process. For a dissolving spherical particle the concentration gradient at the interface is often approximated by

$$\left.\frac{\partial x_j}{\partial r}\right|_{r=R} \propto \frac{\Delta x_j}{\delta}\ , \tag{4.51}$$

where δ is called the boundary layer thickness, a key parameter in describing diffusion-convection problems, and Δx_j represents the mole fraction difference of j over the boundary layer thickness. The boundary layer thickness δ together with the particle radius R defines a spherical shell in which diffusion occurs. In this sense, Eq (4.51) represents a strong simplification of the mole fraction profile in case of a non-steady state process. Outside the spherical shell defined by R and δ the material transport is fully governed by convection. It follows from this approximation that the concentration gradients of all components outside of the spherical shell defined by δ become zero

$$\left.\frac{\partial x_j}{\partial r}\right|_{r>R+\delta} = 0\ , \qquad j = 1, ..., M\ . \tag{4.52}$$

In case the convective flow field around the patricle is (at least approximately) known, the Péclet number can be used to estimate the boundary layer thickness δ [155] as

$$\delta/R \propto Pe^{-1/3}\ ; \tag{4.53}$$

details follow below. The convective contribution to the dissolution kinetics of a spherical particle can be interpreted in the following way: The convective flow field disturbs the concentration profile around the particle as it increases the gradient of the mole fractions by "cutting-off" the concentration profile at a certain distance δ from the interface position R. In the model elaborated in this work the convective

contribution to the transport kinetics is, thus, respected in the form of a "cut-off-distance" δ_c. Inside the spherical shell defined by the cut-off distance δ_c the diffusion equation is solved as usual, without the approximation from Eq (4.51). Thus, a new boundary condition is introduced

$$x_j \Big|_{r=R+\delta_c} = x_{j,S} \ . \tag{4.54}$$

A schematic representation of the influence of δ_c on the mole fraction profile near the solid-liquid interface is depicted in Fig 4.5. It can be seen, that the gradient of the mole fractions x_j becomes steeper for smaller values of δ_c. The influence of δ_c on the dissolution profile of a spherical particle is shown in Fig 4.6. It can be seen that particles dissolve faster with smaller δ_c. Moreover, as δ_c becomes smaller, the characteristic dissolution profile approaches a linear function. It is worth mentioning that although the dissolution profile becomes almost linear for small δ_c, the interface reaction is not the limiting step for the transformation. Thus, the dissolution profile for the case $\delta_c = 0.2R_0$ in Fig 4.6 must not be confused with the chemical reaction control mode of the classical shrinking core model, Eq (2.9). This further stresses the fact that the limiting steps of the dissolution behavior can only be assessed if the flow conditions around the particle can be estimated.

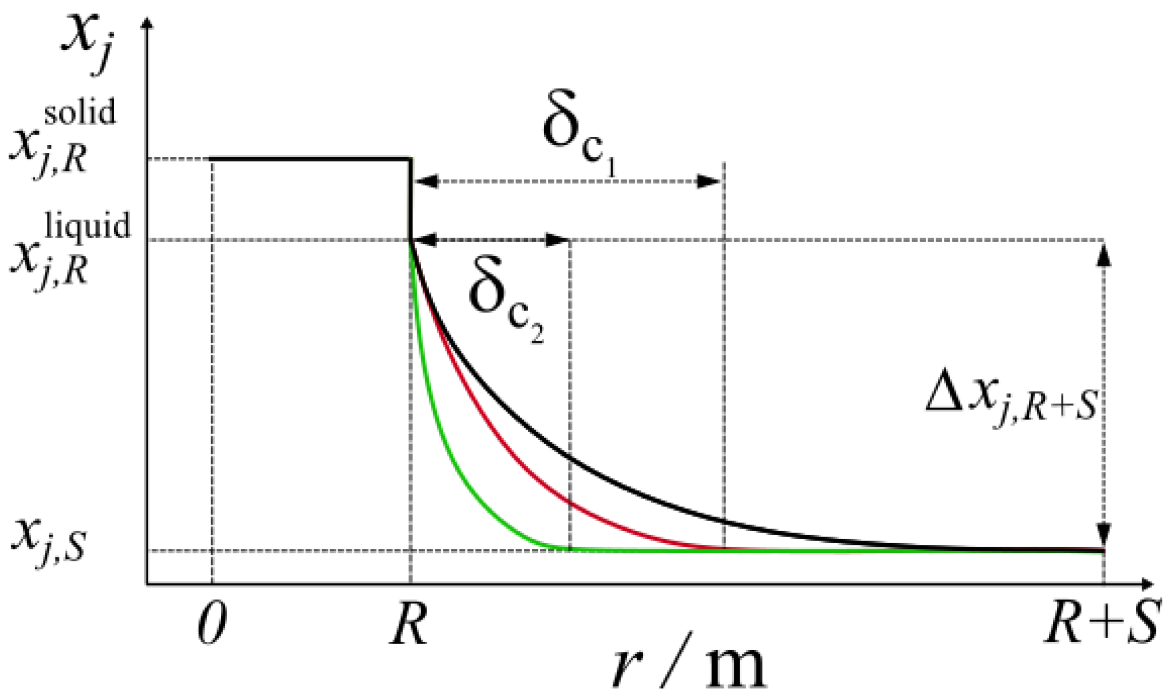

Figure 4.5: Influence of the cut-off distance δ_c on the mole fraction profile near the solid-liquid interface of a spherical particle. Three cases are displayed: the undisturbed mole fraction profile is indicated in black; the two cases where the mole fraction profile is cut-off due to convective effects with δ_{c_1} (red) $> \delta_{c_2}$ (green).

To predict the dissolution kinetics subject to convective flows, it is necessary to estimate the value of the cut-off distance δ_c. Two cases have to be distinguished, i.e. free convection and forced convection. In the first case, density gradients in the melt lead to convective flows and the cut-off distance is determined by the Rayleigh number

$$Ra = \frac{g\,(\rho_R - \rho_S)\,(2R)^3}{D\,\eta}\,, \tag{4.55}$$

where g is the gravitational acceleration ($\approx 9.81\,\mathrm{m\ s^{-1}}$), ρ_R is the fluid density at the solid-liquid interface, ρ_S is the fluid density of the liquid bulk and η is the viscosity of the liquid. As reported by Kerr [156], the cut-off distance for density driven flow can be approximated via

$$\delta_c \approx \frac{2R}{2 + 0.6Ra^{1/4}}\,. \tag{4.56}$$

Additionally, the solid particle might move relative to the molt due to its density being significantly different from the density of the liquid phase. Following Martin

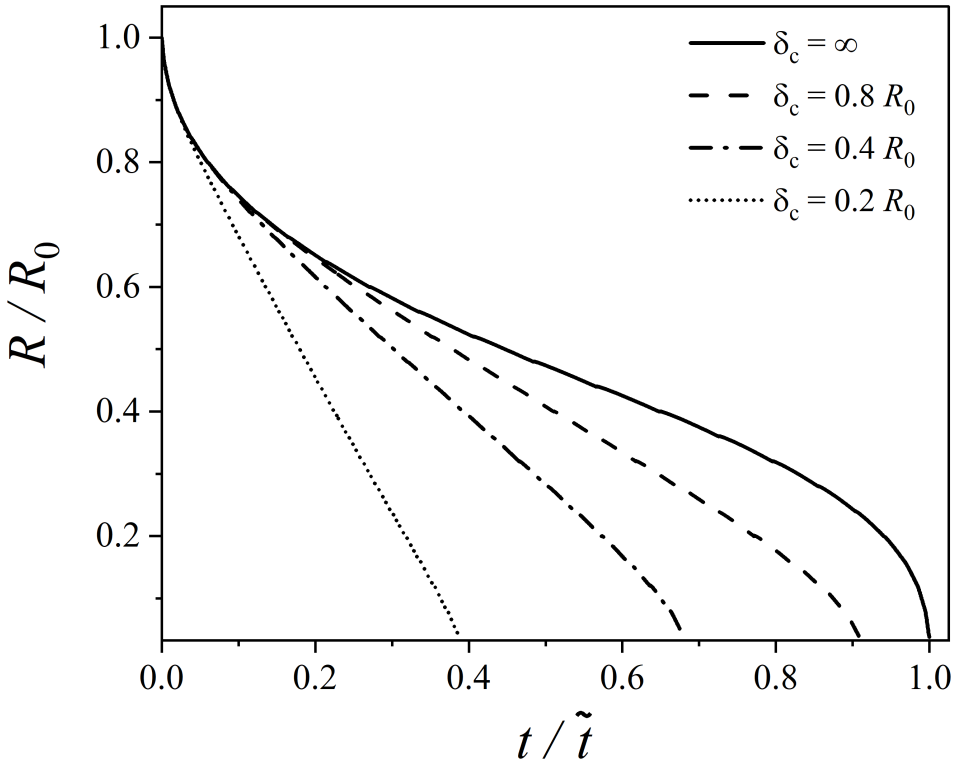

Figure 4.6: Influence of the cut-off distance δ_c on the dissolution profile of a spherical particle.

and Nokes [157], the relative velocity u_c of this particle is calculated from

$$u_c = \frac{g\,(\rho_{\text{solid}} - \rho_R)\,(2R)^2}{18\eta}\ , \tag{4.57}$$

where ρ_{solid} is the density of the solid particle. In the case of small Reynolds numbers Re, defined as

$$Re = \frac{2R\,u_c\,\rho_R}{\eta}\ , \tag{4.58}$$

the Péclet number controls the cut-off thickness. In this case, Kerr [156] suggests the following approximation

$$\delta_c \approx \frac{2R}{1 + (1 + Pe)^{1/3}}\ . \tag{4.59}$$

For Reynolds numbers $Re \leq 10^5$ Zhang and Xu [158] recommend the use of the following expression to approximate the Sherwood number Sh

$$Sh \approx 1 + (1 + Pe)^{1/3} \left(1 + \frac{0.096 Re^{1/3}}{1 + 7 Re^{-2}} \right) . \tag{4.60}$$

Finally, the Sherwood number Sh can be used together with

$$Sh = 2R/\delta_c \, , \tag{4.61}$$

to calculate the cut-off distance δ_c for a wide range of the Reynolds number Re.

5 | Experimental part and validation

The numerical model is validated by means of experimental observations using High-Temperature Confocal Scanning Laser Microscopy (HT-CSLM). The numerical results are compared to published data from the open literature and from experiments that are performed at the Chair of Ferrous Metallurgy at Montanuniversität Leoben. HT-CSLM is chosen for investigating the kinetics of solid-liquid phase transformations due to the offered possibility to observe in-situ phase transformations in metallurgical slags at high temperatures (> 1500°C). It is worth noting that iron(oxide)-containing slags can not be investigated in the HT-CSLM due to diminishing optical transparency. Nevertheless, it is expected that lessons learned using other steelmaking slags (e.g. CaO-SiO_2-Al_2O3-slags) can be applied to Fe-containing slags.

5.1 High-Temperature Confocal Scanning Laser Microscopy set-up

The experimental set-up consists of a VL2000DX CSLM from Lasertec and a high temperature furnace of the type SVF17-SP from Yonekura. The furnace chamber is ellipsoidal in shape and coated with gold. The thermal radiation emitted by a halogen lamp located in one of the focal points of the ellipsoid is reflected by the walls of the furnace onto the sample located in the opposite focal point. During the experiment, the sample is placed in a platinum crucible standing on a sample holder. The platinum crucible can withstand the high temperatures during the experiment (>1500 °C) and does not undergo any significant reactions with the slags that are used. A laser beam with a wavelength of 405 nm acts as a light source. A camera system captures the laser light reflected from the sample, and finally a video recording of the observed sample throughout the experiment is made. A sketch of the experimental set-up is shown in Fig 5.1.

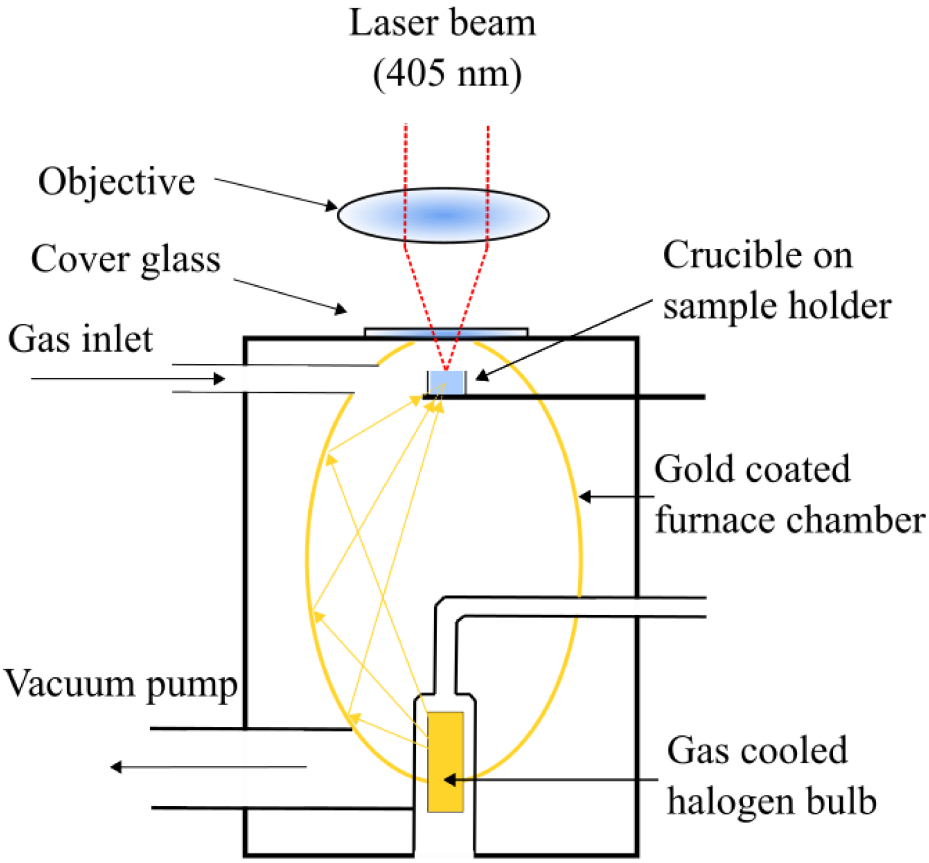

Figure 5.1: A schematic diagram of the HT-CSLM set-up at the Chair of Ferrous Metallurgy, Montanuniversität Leoben. The yellow arrows indicate that electromagnetic waves emanating from the halogen bulb are reflected at the ellipsoidal walls of the furnace chamber and converge at the opposite focal point of the ellipsoid, i.e. the position of the sample.

5.2 Cyclic partial phase transformations in the CaO-SiO_2 system

The theoretical concepts presented in Section 4.1 are applied to complement experimental studies of congruent and incongruent solid-liquid phase transformations in the CaO-SiO_2 system using cyclic partial phase transformations [159–162] via High-Temperature Confocal Scanning Laser Microscopy (HT-CSLM), see Ogris et al. [163]. The results of this publication [163] are summarized in the following and conclusions are drawn for modelling the dissolution kinetics of oxide particles dissolving in multi-component slags:

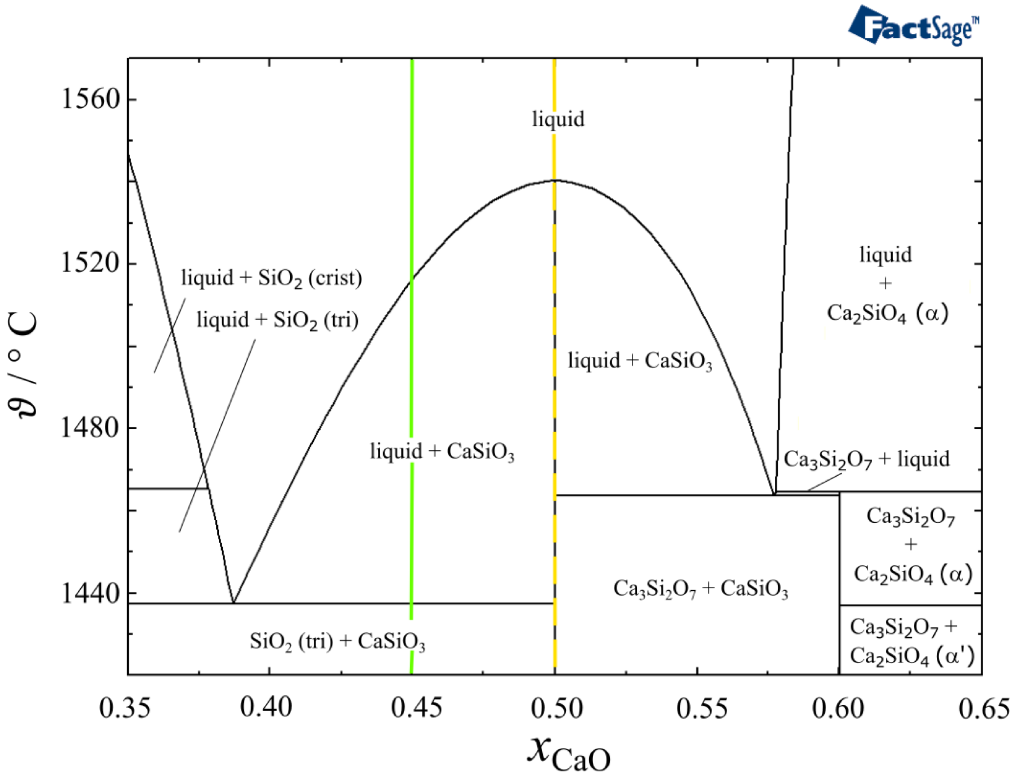

Figure 5.2: A section of the CaO-SiO_2 phase diagram calculated using FactSage 7.2 and the FToxid database. The composition for incongruent phase transformations is highlighted in green. The composition for the congruent case is indicated in yellow [163].

Two slag compositions are chosen at which congruent and incongruent solid-liquid phase transformations are expected to occur, respectively (see Fig 5.2). In the incongruent case, diffusion is likely to significantly affect the kinetics of the investigated solid-liquid phase transformations, while in the congruent case chemical diffusion is not required. The cyclic growth and shrinkage of a solid phase (i.e. wollastonite) is observed in-situ via HT-CSLM while the binary slag system is subjected to cyclic heating (above the liquidus or melting temperature, respectively) and cooling. The heat treatment is designed to keep both the solid and the liquid phase present throughout the experiment to suppress nucleation processes during the observation. The kinetics of the solid-liquid phase transformations can be derived from the measurement of the mean velocity of the solid-liquid front and the increase in observable area of the solid phase during the heat treatment. The solid-liquid front that is tracked via HT-CSLM in the observation window is shown in Fig 5.3.

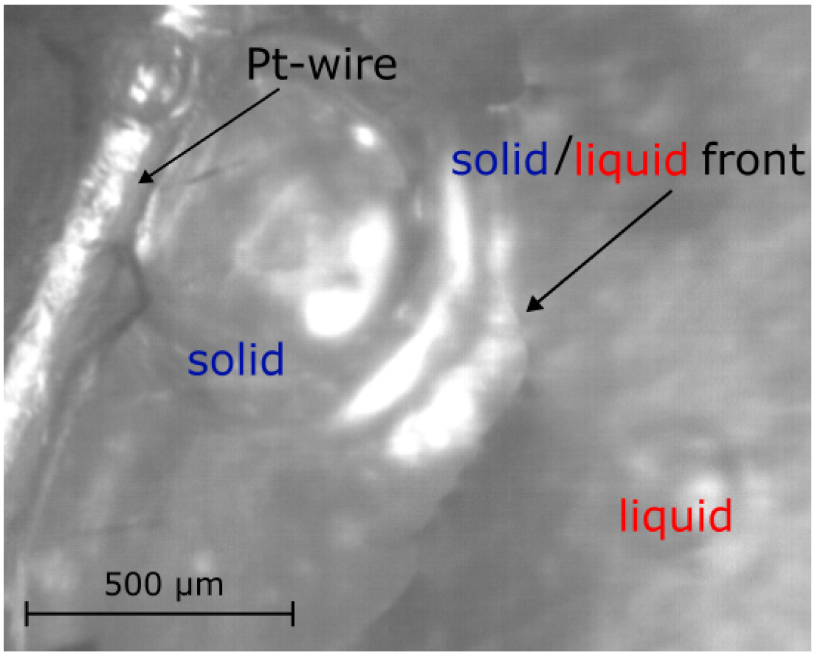

Figure 5.3: An image of the solid/liquid front during a transformation cycle at 1515°C observed in-situ via HT-CSLM. During solidification, the solid wollastonite (bright gray) grows, meaning that the solid/liquid front migrates to the right. In the case of melting, the wollastonite shrinks, which can be observed via a front migration to the left. The platinum wire used as the original nucleation site is also visible [163].

The evolution of the normalized observable area A/A_0 of wollastonite during one representative cycle of the induced partial phase transformations for the congruent case is shown in Fig 5.4. The congruent case is indicated via a double line and open triangle symbols. The cycle starts with the growing stage (highlighted in blue) which is initiated by lowering the temperature. After reaching the target (minimum) temperature, the sample is heated up instantly. Now, the temperature rises while the solid phase is still subject to growth; this stage is called inverse stage (highlighted in red). Finally, after surpassing the melting temperature, the velocity of the solid-liquid interface changes its direction rapidly and the observable area of the solid phase declines, i.e. the shrinking stage (indicated in black) is initiated. In contrast to congruent phase transformations, the observed incongruent transformations (indicated via single line and open circles in Fig 5.4) are characterized by an additional pronounced transformation stage where the velocity of the solid-liquid interface approaches almost zero. This stage is referred to as "stagnant stage" and is highlighted in green in Fig 5.4. This phenomenon is investigated by means of simulating the cyclic partial phase transformation using the sharp-interface approach presented above. The

basic features of the kinetics of incongruent transformations can be described by a diffusion-controlled mechanism, using Eq (4.1) for deriving the boundary condition at the interface and Eq (4.2) to calculate the velocity of the interface. The numerical results are presented in Fig 5.5. The stagnant stage appears due to the diffusion-controlled manner of incongruent phase transformations as the interface velocity can not change its direction immediately after reaching the peak position as long as the mole fraction field around the interface does not support the net material transport in the new direction, see Fig 5.5 (b).

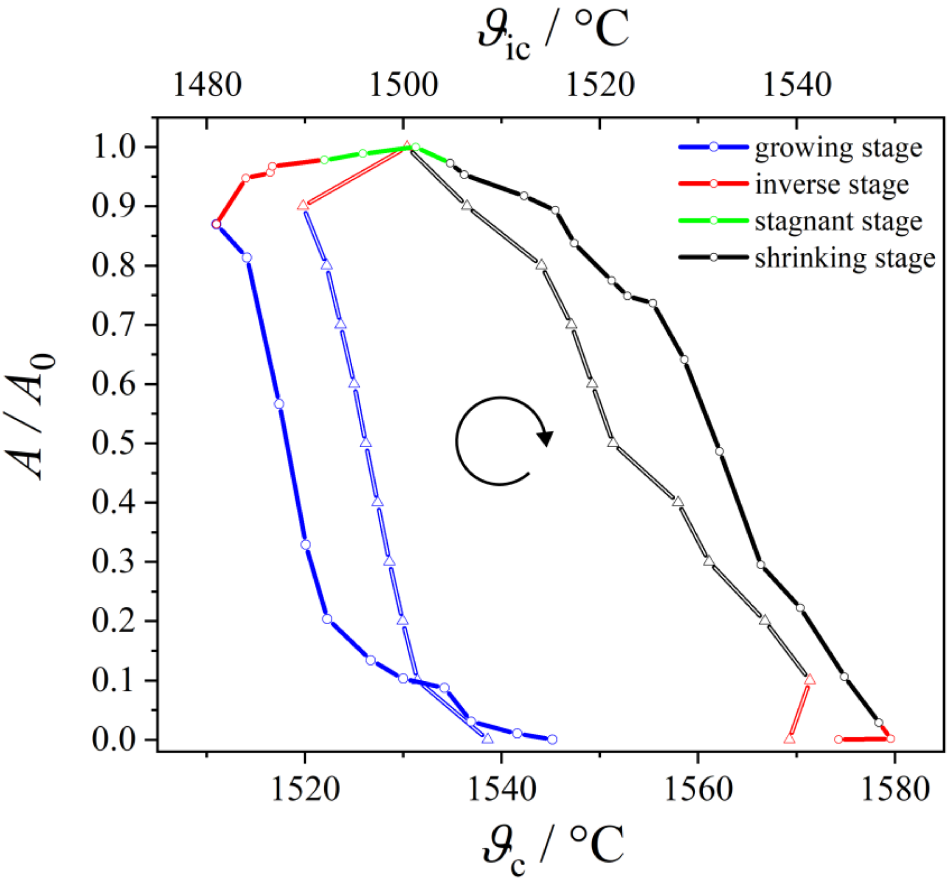

Figure 5.4: Representative results showing the evolution of the normalized observable area of wollastonite during a heating cycle for the congruent (c) and incongruent (ic) case [163]. The curved arrow indicates time direction.

In contrast, the kinetics of congruent phase transformations is modeled by a rate limiting reaction at the interface, where the equal jump condition, Eq (4.3), applies. Bulk chemical diffusion is not required during congruent phase transformations. The interface velocity for the congruent case is calculated using Eq (4.6). Based on the

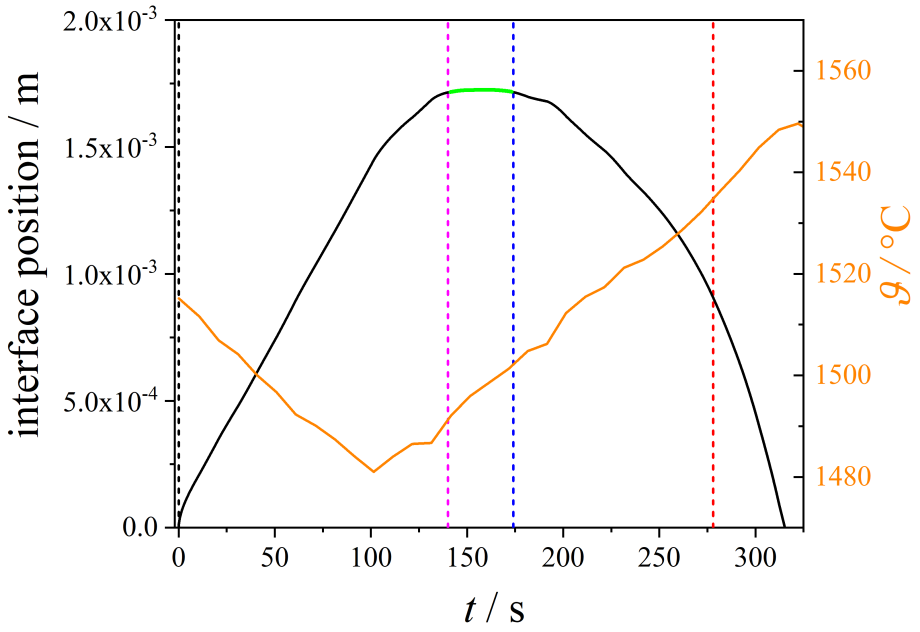

(a)

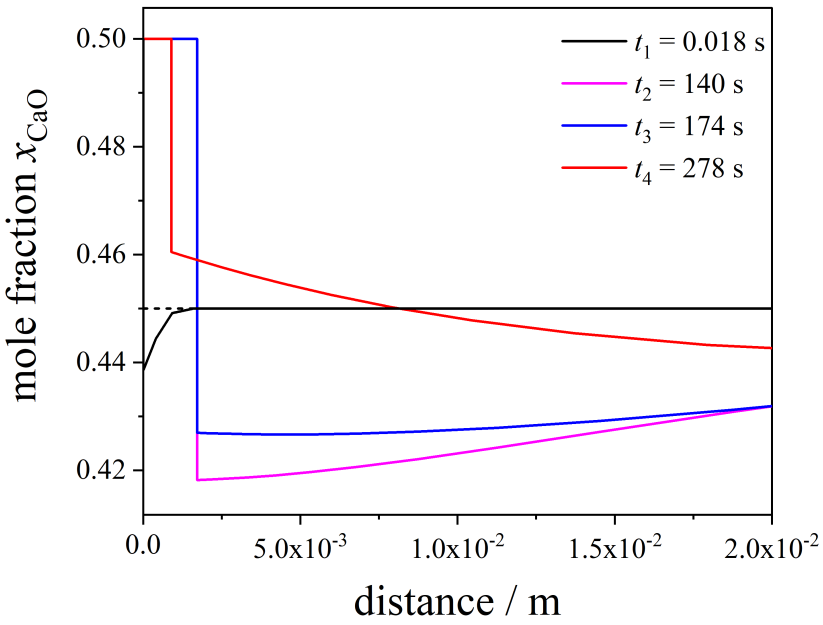

(b)

Figure 5.5: Simulated evolution of the interface position for the incongruent case during a representative transformation cycle (a). The stagnant stage is highlighted in green. The temperature during the transformation cycle is represented via the orange line. The color coded dashed lines correspond to the times at which the mole fraction profiles of x_{CaO} are shown in (b), [163].

results from the numerical model, the stagnant stage is not predicted to occur in cyclic partial phase transformations subject to the congruent case. The velocity of the interface simply follows the direction on the chemical driving force Δf^{chem} acting on it. The experimental observations are compared to the numerical results for the incongruent and the congruent case in Fig 5.6.

In the congruent case the peak of the normalized area profile A/A_0 of the simulated transformation cycle is located at a higher time compared to the experimental observation. It is likely that a deviation of the actual temperature at the solid/liquid interface from the temperature measurement during the experiment caused this divergence. Due to its faster kinetics, this phenomenon is more dominant in the congruent case. The complex heat flow through the experimental set-up is not accounted for in the numerical simulations, i.e the temperature is assumed to be evenly distributed over the sample, for details see Ogris et al. [163]. However, the basic features of the kinetics of congruent and incongruent solid-liquid phase transformations in oxide systems can be described using the simple concepts presented above. Specifically, it is shown that the kinetics of solid-liquid phase transformations in the CaO-SiO_2 system are limited solely by bulk diffusion in the liquid phase in case of incongruent transformations and are limited by an interfacial reaction in the congruent case. The insights derived from this study [163] are used for modelling the dissolution kinetics of various oxides in multi-component slags, as subsequently discussed.

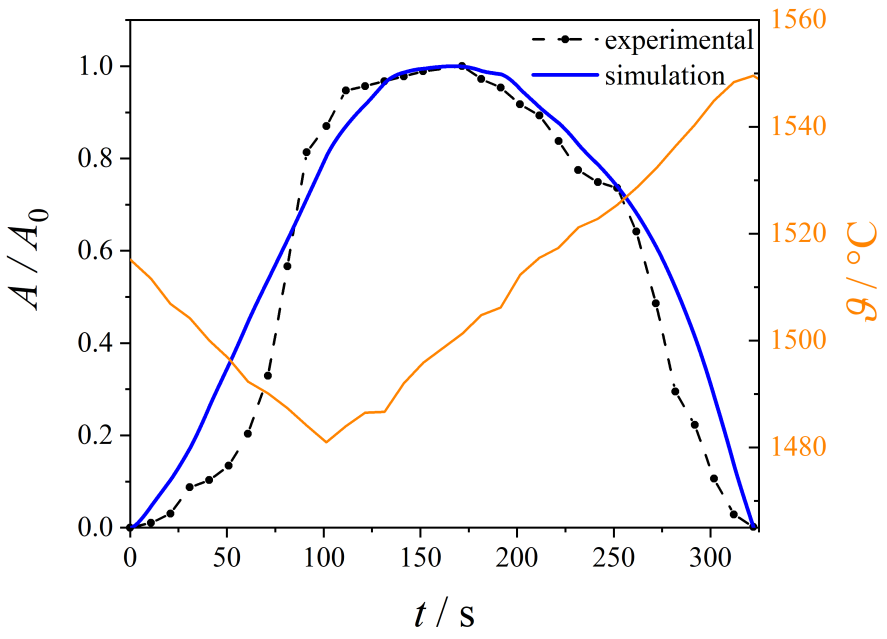

(a) incongruent case

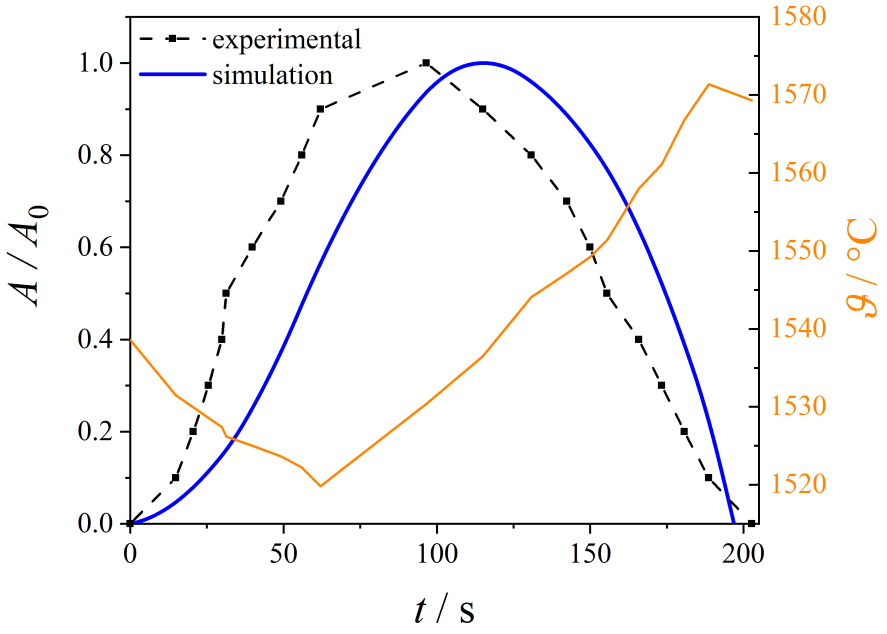

(b) congruent case

Figure 5.6: Evolution of normalized observed area of the solid phase (wollastonite) during a representative transformation cycle subject to the incongruent (a) and the congruent (b) regime [163]. The experimental data (black dots and dashed line) stemming from HT-CSLM observations is compared to numerical results (highlighted in blue). The evolution of the temperature during the transformation cycle is given via the orange line.

5.3 Dissolution of oxide particles in multi-component slags - model validation using experimental data from literature

5.3.1 Dissolution of lime

As stated in the introductory chapter, the dissolution of lime (CaO) plays a major role in slag formation during oxygen steelmaking. Various experimental investigations on the dissolution of lime are described in literature, e.g. [31–33, 37, 38, 164–168]. Generally, two different dissolution mechanisms are conceivable, direct dissolution and indirect dissolution. The direct dissolution reaction of lime can be expressed as

$$\mathrm{CaO(s)} \rightarrow \mathrm{(CaO)}\ , \tag{5.1}$$

where the solid lime is directly transferred into the liquid slag solution. The round brackets in (CaO) indicate the species in liquid slag. Indirect dissolution occurs when a solid product layer is formed around the dissolving particle. In the case of lime dissolution in silica containing slags, Ca_2SiO_4 together with Ca_3SiO_5 have been identified as the dominating phases in the product layer [31,38,47]. According to Sun et al. [47], the following reactions are thermodynamically important in the case of the indirect dissolution mechanism

$$3\mathrm{(CaO)} + \mathrm{(SiO_2)} \rightarrow \mathrm{Ca_3SiO_5(s)} \tag{5.2}$$

$$2\mathrm{Ca_3SiO_5(s)} + \mathrm{(SiO_2)} \rightarrow 3\mathrm{Ca_2SiO_4(s)} \tag{5.3}$$

$$2\mathrm{(CaO)} + \mathrm{(SiO_2)} \rightarrow \mathrm{Ca_2SiO_4(s)} \tag{5.4}$$

$$\mathrm{Ca_2SiO_4(s)} \rightarrow 2(\mathrm{Ca^{2+}}) + (\mathrm{Si^{4+}}) + 4(\mathrm{O^{2-}}) \tag{5.5}$$

In the case of lime dissolution during steelmaking operations, the direct mechanism is preferred. This is due to the relatively slow transformation kinetics that are observed during indirect dissolution [38]. Sun et al. [47] observed the dissolution of lime at 1480°C in a ternary $CaO\text{-}SiO_2\text{-}Al_2O_3$ (CAS) slag using HT-CSLM. The slag composition they used for their investigations is provided in Table 5.1. They observed a three-stage dissolution process:

1. The first stage is characterized by direct dissolution of lime into the liquid slag.
2. After a certain amount of time an intermediate boundary layer forms at the solid-liquid interface slowing down the shrinking rate of the lime particles.

3. The intermediate boundary layer dissolves rapidly at the end of the second stage and after its disappearance the solid-liquid transformation evolves rapidly again.

It is shown by Ogris and Gamsjäger [151] that the dissolution kinetics of lime for this case can be properly described by considering multi-component diffusion in the liquid only using the modelling approach and software described above. The three-stage process observed in experiment is handled in the following way: During the first stage multi-component diffusion in the liquid phase limits the kinetics of the dissolution process. The interdiffusivity matrix is estimated from Liang and Davis [169] and is provided in Table 5.2. During the second stage the multi-component diffusion is still the limiting process. However, the interdiffusivity matrix is multiplied by a retardation factor $\alpha_{\mathrm{ret}} = 0.3$ that restrains the kinetics. It is assumed that diffusion through the intermediate boundary layer limits the kinetics during this stage; however, the diffusivities to be applied are not known. In this sense, α_{ret} needs to be seen as a fitting parameter. After the intermediate boundary layer has dissolved, the kinetics accelerate again, this is accounted for by applying the original diffusivity values as in the first stage. The numerical results from the sharp-interface model are compared to the experimental observations of Sun et al. [47] Fig 5.7, see [151]. It is not clear when the second and third stages occur. The nucleation kinetics of the intermediate boundary layer is not considered explicitly in the model. The time span required for the formation of a nucleus with critical size can only be predicted to a limited extent from a theoretical perspective. Furthermore, it is not entirely clear how to predict the time span for the intermediate boundary phase to fully disappear (here at about 170 s). The timings for the second and third stages (indicated by the dashed lines in Fig 5.7) are thus fitting parameters that are only accessible through experimental observations.

Table 5.1: Chemical composition of Slag SM04 in weight fractions as reported by [47].

Slag	w_{CaO}	$w_{\mathrm{SiO_2}}$	$w_{\mathrm{Al_2O_3}}$
SM04	0.267	0.533	0.200

Table 5.2: The chemical diffusion coefficients for the simulation of lime dissolution in Slag SM04.

$\tilde{D}_{\mathrm{CaO\text{-}CaO}}/\mathrm{m^2s^{-1}}$	$\tilde{D}_{\mathrm{CaO\text{-}SiO_2}}/\mathrm{m^2s^{-1}}$	$\tilde{D}_{\mathrm{SiO_2\text{-}CaO}}/\mathrm{m^2s^{-1}}$	$\tilde{D}_{\mathrm{SiO_2\text{-}SiO_2}}/\mathrm{m^2s^{-1}}$
$3.9 \cdot 10^{-11}$	$0.36 \cdot 10^{-11}$	$-1.9 \cdot 10^{-11}$	$0.8 \cdot 10^{-11}$

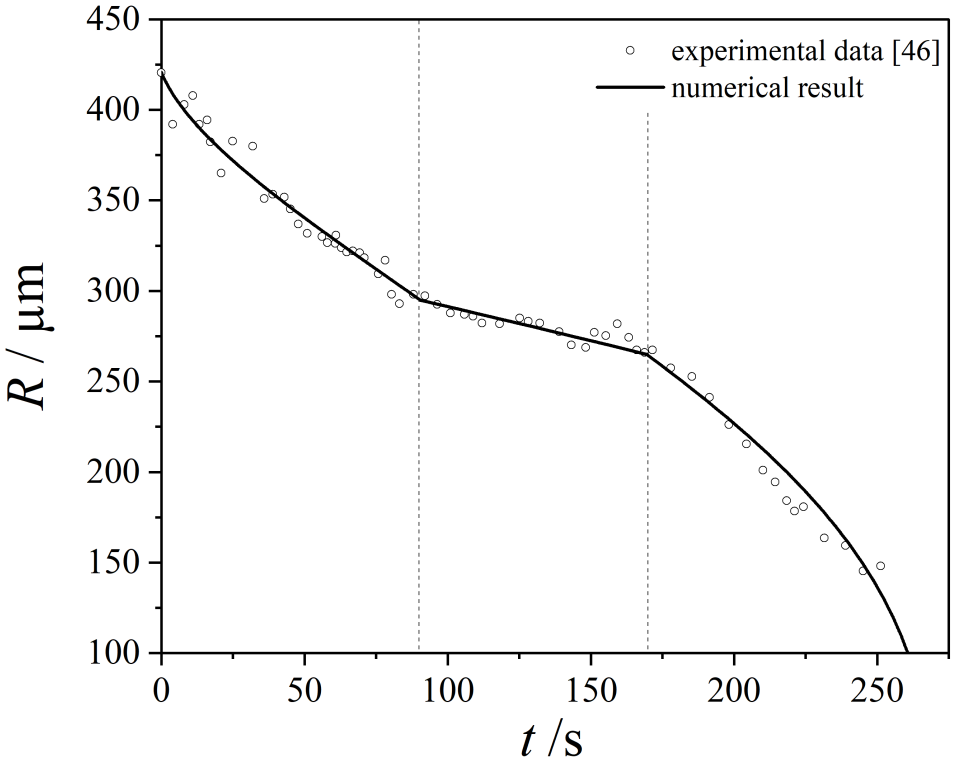

Figure 5.7: Lime dissolution at 1480°C in a ternary CaO-SiO_2-Al_2O_3 slag with a composition of w_{CaO}=0.267, w_{SiO_2}=0.53 and $w_{Al_2O_3}$=0.20 [151]. The experimental data is taken from [47]. The dashed lines indicate the presence of an intermediate boundary layer at the solid-liquid interface, i.e. Ca_2SiO_4.

5.3.2 Dissolution of silica

In the context of inclusion control and steel cleanliness, Michelic et al.[48] investigated the dissolution of silica (SiO_2) in CAS slags by means of HT-CSLM experiments. The composition of Slag 1.1 that was used for their silica dissolution investigations is provided in Table 5.3. In the case of dissolving silica particles, no intermediate boundary layers are reported to occur during the dissolution in CAS slags at 1450°C. Thus, in contrast to the dissolution of lime described above, the transformation kinetics of silica is subject only to direct dissolution. Adapting the quasi-static approximation of the Stefan problem (see section 2.4), Eq (2.25), Michelic et al. introduce an additional

correction parameter f to describe their observations by using

$$\frac{dR}{dt} = -\frac{c_R - c_S}{[[c]]} \left(\frac{D}{R} + f\sqrt{\frac{D}{\pi t}} \right) . \tag{5.6}$$

The correction factor f is a fitting-parameter without physical meaning and only corrects the oversimplifications in the quasi-stationary approximation. Thus, Eq (5.6) can not be used for predicting the dissolution kinetics of silica particles in steelmaking slags. However, it is shown by Ogris and Gamsjäger [151] that the transformation kinetics observed by Michelic et al. [48] can be described by solely considering diffusion in the liquid phase without the need to introduce additional fitting-parameters. To this end, the sharp interface model is applied to predict the dissolution kinetics of a silica particle in slag 1.1. The interdiffusivity matrix can be estimated from Liang and Davis [169] and is provided in Table 5.4. The numerical results of the sharp-interface model are compared with the experimental data from Michelic et al. [48] in Fig 5.8. It seems that by considering multi-component diffusion alone the kinetics of the dissolution process can be described sufficiently. Since the dissolution curves obtained through the numerical calculations closely resemble the experimentally derived dissolution kinetics, without requiring any additional fitting parameters, it is likely that the influence of convection on the dissolution process is negligible for the HT-CSLM experiments discussed so far. This conclusion is likely valid as long as the experimental investigations using HT-CSLM or other techniques do not involve external stirring, intense particle movement and high density differences in the melt do not occur.
The next section covers experimental and numerical investigations on alumina dissolution in CAS slags, where both convective contributions to mass transfer and mass transfer due to diffusion in the liquid need to be considered.

Table 5.3: Chemical composition of Slag 1.1 in weight fractions as reported by [48].

Slag	w_{CaO}	$w_{\mathrm{SiO_2}}$	$w_{\mathrm{Al_2O_3}}$
1.1	0.341	0.546	0.106

Table 5.4: The chemical diffusion coefficients for the simulation of silica dissolution in Slag 1.1.

$\tilde{D}_{\mathrm{CaO\text{-}CaO}}/\mathrm{m^2s^{-1}}$	$\tilde{D}_{\mathrm{CaO\text{-}SiO_2}}/\mathrm{m^2s^{-1}}$	$\tilde{D}_{\mathrm{SiO_2\text{-}CaO}}/\mathrm{m^2s^{-1}}$	$\tilde{D}_{\mathrm{SiO_2\text{-}SiO_2}}/\mathrm{m^2s^{-1}}$
$5.2 \cdot 10^{-11}$	$-0.14 \cdot 10^{-11}$	$-0.21 \cdot 10^{-11}$	$0.18 \cdot 10^{-11}$

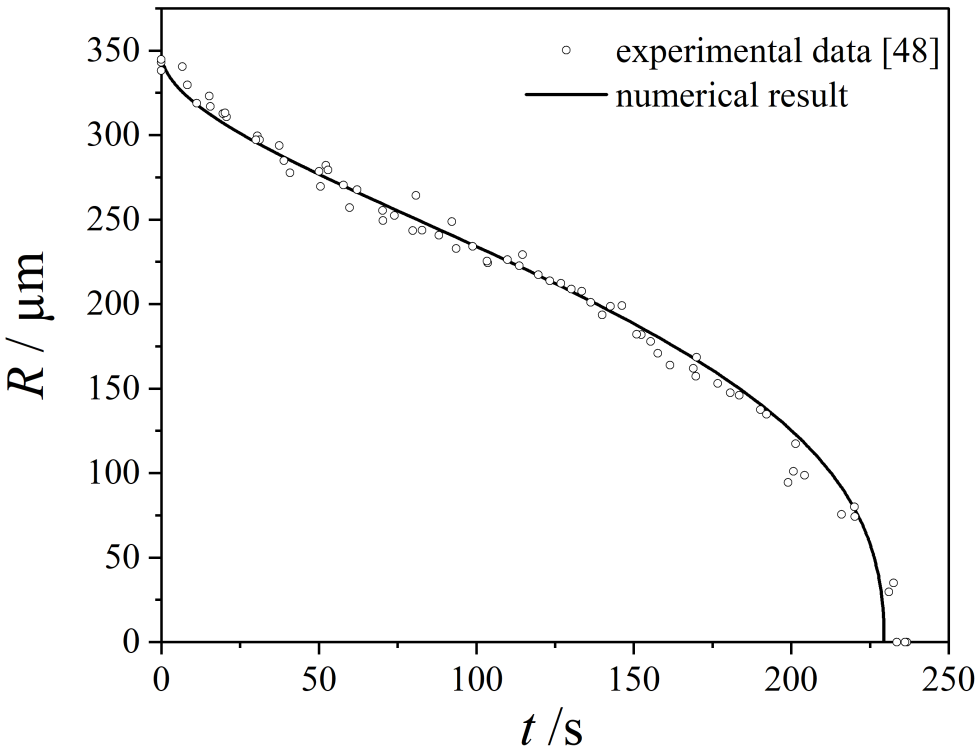

Figure 5.8: Silica dissolution in CaO-SiO_2-Al_2O_3 at 1480 °C [151]. The composition of the slag is w_{CaO}=0.341, w_{SiO_2}=0.546 and $w_{Al_2O_3}$=0.106 according to [48]. The slag composition is slightly corrected in the numerical model so that the sum of the mass fractions adds up to unity by distributing the missing mass fractions evenly among the individual constituents.

5.4 Dissolution of alumina - in-situ experiments

The dissolution of alumina particles in different CaO-SiO_2-Al_2O_3 slags is investigated by means of HT-CSLM experiments performed at the Chair of Ferrous Metallurgy at Montanuniversität Leoben; the experimental results are compared to predictions made using the sharp-interface model and assuming local equilibrium at the interface.

5.4.1 Sample preparation and temperature measurement

The slag samples are prepared by mixing the oxides (CaO-Al_2O_3-SiO_2) according to the desired slag composition and heating the material above 1500°C in a platinum crucible and holding for a minimum of 15 minutes; thus, melting and overheating the slag. After cooling, the sample is ground and eventually filled in the platinum crucible used in the HT-CSLM experiment. The pre-melting procedure ensures optimal homogenization of the slag samples before the start of the dissolution experiment. The slag is melted again before the actual experiment in the HT-CSLM furnace to prevent bubble formation during the experiment. The temperature in the furnace is measured by means of a thermocouple situated below the platinum crucible and deviates significantly from the actual temperature of the sample during the experiment. To determine the actual temperature in the sample, a thermocouple is placed at the center of the crucible during pre-melting in the HT-CSLM. The temperature is measured simultaneously by the two thermocouples in the furnace and in the crucible, respectively. In this way, a reference for the actual sample temperature during the performed dissolution experiments is established. This is done before each trial. A representative reference measurement is shown in Fig 5.9. It can be seen that the sample temperature lies significantly lower than the furnace temperature; this difference must be taken into account in the temperature control during the actual experiment where only the furnace thermocouple is used.

5.4.2 Experimental procedure

At the beginning of the actual experiment, before the platinum crucible is placed in the furnace, an spherical alumina particle with a radius of 250 µm (obtained from Sandoz Fils SA) is placed on top of the pre-melted slag. Then the platinum crucible is placed inside the HT-CSLM and is heated up to experimental temperature. The dissolution of the oxide particle can be observed in-situ and is video-recorded for later evaluation. The evolution of a spherical alumina particle during dissolution at 1500 °C in a CaO-SiO_2-Al_2O_3 slag is shown in Fig 5.10. The experimental temperature is maintained for the duration of the dissolution of the particle (isothermal holding). After the particle is fully dissolved, the furnace is cooled down to room temperature. The obtained video-recordings from the dissolution experiment are evaluated by means of the following steps:

1. A set of frames of the original video is extracted by means of the video processing software VirtualDub [170].

2. For each individual frame the area of the dissolving particle is measured manually using Jens Rüdig's image analyzing software [171].

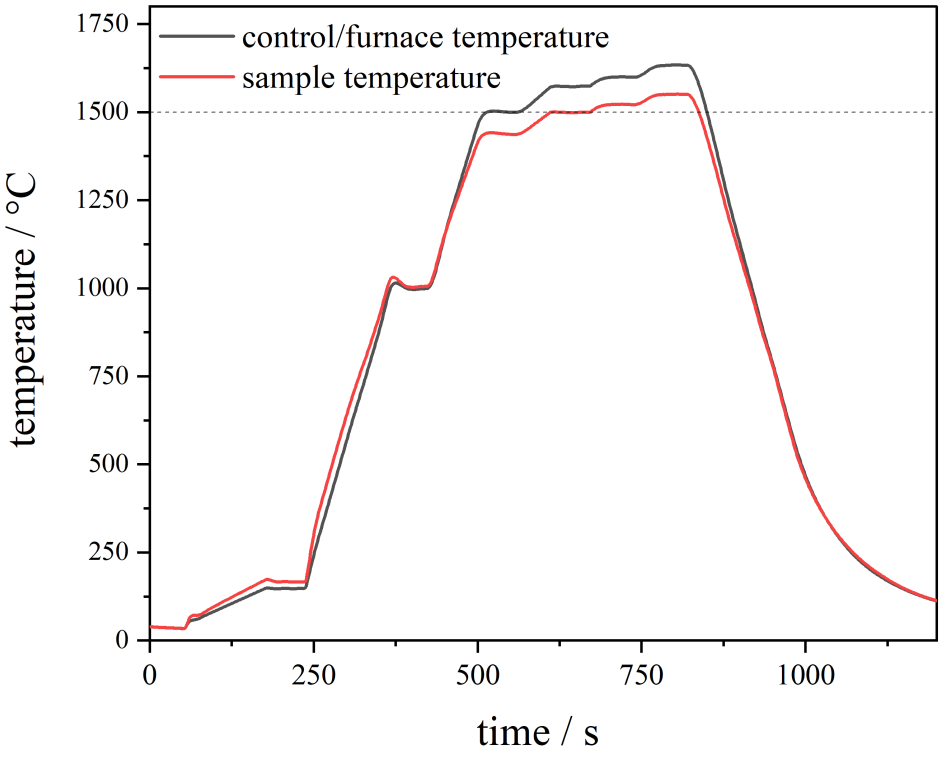

Figure 5.9: Representative reference measurement of the control/furnace temperature and sample temperature. The dashed line indicates the 1500°C mark where alumina dissolution experiments are performed.

3. The measurement of the area is repeated 3 times for each frame as there exists a certain error due to the manual measurement procedure. The standard deviations of these measurements allow to estimate the quality of the experimentally obtained image data.

The dissolution of the alumina particles is observed in-situ in three different slags. The compositions are chosen in such a way that interdiffusivities, molar volumes, thermal conductivities and viscosities can be directly obtained from literature. It is hoped that actual predictions are possible with the numerical model. In case that the model predictions agree well with experimental observations, then this supports the validity and usefulness of the modelling approach developed above, as no fitting parameters are used for simulating the transformation kinetics. The slag compositions

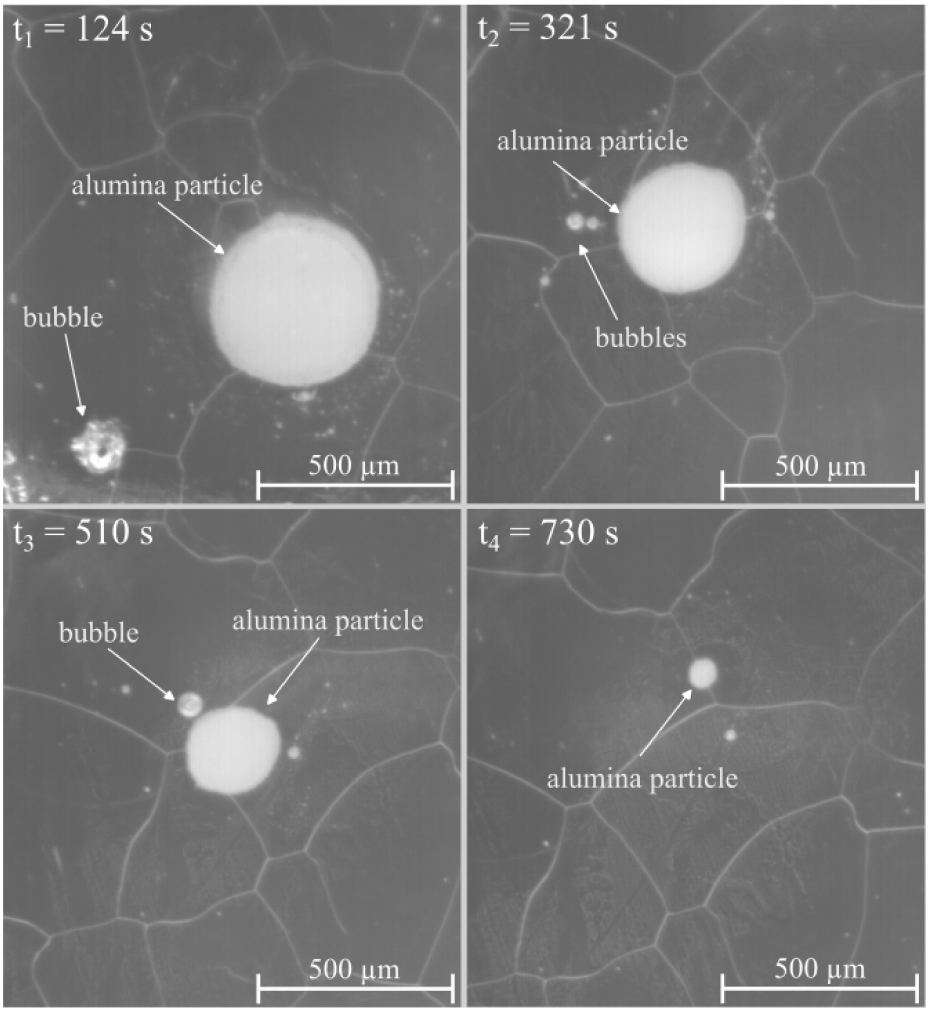

Figure 5.10: Alumina particle dissolving at 1500°C in a CaO-SiO_2-Al_2O_3 slag (Slag 2) at four different times, i.e. $t_1 = 124\,s$, $t_2 = 321\,s$,$t_3 = 510\,s$ and $t_4 = 730\,s$.

selected for the dissolution trials are presented in Table 5.5.

Table 5.5: Slag compositions for alumina dissolution experiments.

Slag	w_{CaO}	$w_{\mathrm{SiO_2}}$	$w_{\mathrm{Al_2O_3}}$
1	0.25	0.60	0.15
2	0.35	0.45	0.2
3	0.30	0.525	0.175

Alumina dissolution in Slag 1

The evolution of the radius of a shrinking alumina particle in Slag 1 (for composition see Table 5.5) with time is shown in Fig 5.11. The prediction from the sharp-interface model is indicated via the solid lines. The shrinking behavior of the alumina particles is predicted by means of the sharp-interface model using the interdiffusivities suggested by Liang et al. [172] with SiO_2 as the dependent species. The values of the diffusivities are listed in Table 5.6. The boundary conditions (equilibrium mole fractions) at the interface are calculated using the assessment of Eriksson and Pelton [173] and are listed in Table 5.7.

Table 5.6: Interdiffusivities in $\mathrm{m^2 s^{-1}}$ used in the dissolution simulations.

Slag	$\tilde{D}_{\mathrm{CaO\text{-}CaO}}$	$\tilde{D}_{\mathrm{CaO\text{-}Al_2O_3}}$	$\tilde{D}_{\mathrm{Al_2O_3\text{-}CaO}}$	$\tilde{D}_{\mathrm{Al_2O_3\text{-}Al_2O_3}}$	Reference
1	$4.22 \cdot 10^{-11}$	$-0.44 \cdot 10^{-11}$	$-0.54 \cdot 10^{-11}$	$1.44 \cdot 10^{-11}$	[172]
2	$14.6 \cdot 10^{-11}$	$2.26 \cdot 10^{-11}$	$-7.35 \cdot 10^{-11}$	$2.02 \cdot 10^{-11}$	[172]
3	$10.60 \cdot 10^{-11}$	$1.23 \cdot 10^{-11}$	$-4.76 \cdot 10^{-11}$	$1.62 \cdot 10^{-11}$	[172]

Table 5.7: Boundary conditions (i.e. mole fractions) at the solid-liquid interface calculated via Gibbs energy minimization.

Slag	$x_{R,\mathrm{CaO}}$	$x_{R,\mathrm{Al_2O_3}}$	$x_{R,\mathrm{SiO_2}}$
1	0.226	0.268	0.506
2	0.317	0.303	0.380
3	0.272	0.284	0.444

In addition to multi-component diffusion, convective mass transfer is considered. As discussed above, the influence of the density driven flow might be predicted using

the Rayleigh number Ra. First the maximum density difference $\Delta\rho$ in the melt must be calculated. This density difference $\Delta\rho$ is given by

$$\Delta\rho = \left(\frac{M_R}{V_R} - \frac{M_S}{V_S} \right) , \tag{5.7}$$

where M_R and M_S are the molar mass of the melt at the interface and in the liquid bulk, respectively; V_S and V_R are the molar volume of the melt at the interface and in the liquid bulk, respectively. For the calculation of the molar volumes V_S and V_R Courtial and Dingwell [174] suggest the following relation

$$V_{\text{liquid}} = x_1 x_2 \left(L_{12}^1 + L_{12}^2 (T - 1873) \right) + \sum_{i=1}^{3} x_i \left(L_i^1 + L_i^2 (T - 1873) \right) , \tag{5.8}$$

where L_{12}^1, L_{12}^2, L_i^1 and L_i^2 are parameters suggested in [174], see Table 5.8. The indices $i = 1, 2, 3$ correspond to $1 \equiv \text{CaO}$, $2 \equiv \text{SiO}_2$ and $3 \equiv \text{Al}_2\text{O}_3$, respectively. The viscosities η are estimated from the assessment provided by Tang et al. [175].

Table 5.8: Parameters suggested by Courtial and Dingwell [174] for the calculation of molar volumes from Eq (5.8).

i	L_i^1	L_i^2
CaO	20.843	$4.333 \cdot 10^{-3}$
SiO_2	27.611	$1.849 \cdot 10^{-3}$
Al_2O_3	36.361	$-2.055 \cdot 10^{-3}$
	L_{12}^1	L_{12}^1
CaO-SiO_2	-8.348	$-4.137 \cdot 10^{-3}$

The molar Volumes V_S and V_R are listed together with the molar mass M_S and the viscocities for the Slags 1-3 in Table 5.9.

From Fig 5.11 it can be seen that the dissolution kinetics during the first third ($\approx 1000\,\text{s}$) of the dissolution process can be adequately described by considering only multi-component diffusion (dashed line). After that, convective contributions need to be considered. This becomes clearer by comparing the evolution of the mole fraction profiles $x_{\text{Al}_2\text{O}_3}$ of alumina during the dissolution in Fig 5.12. At the beginning of the dissolution, i.e. $t = 0.5\,\text{s}$ the cut-off distance δ_c (indicated via dashed orange lines) is high relative to the diffusion penetration depth (DPD) into the melt. In this context, the DPD is the thickness of the part of a mole fraction profile where

Table 5.9: Molar masses, volumes and viscosities of selected slags at 1773 K.

Slag	$M_S/\mathrm{kg\,mol^{-1}}$	$V_S/\mathrm{m^3 mol^{-1}}$	$V_R/\mathrm{m^3 mol^{-1}}$	η/Pa s
1	0.063	$24.91 \cdot 10^{-6}$	$27.39 \cdot 10^{-6}$	8.3
2	0.0637	$24.27 \cdot 10^{-6}$	$27.02 \cdot 10^{-6}$	3.6
3	0.0633	$24.56 \cdot 10^{-6}$	$27.16 \cdot 10^{-6}$	5.94

its gradients are non-zero. As long as the cut-off distance is greater than the DPD, the mole fraction profile of alumina is unaffected by the density-driven flow, i.e. the mole fraction profile is equal to the case of a purely-diffusion driven transformation (dashed black lines). After a certain amount of time, the cut-off distance and the DPD intersect; from this time on the boundary condition Eq (4.54) applies and the mole fraction profiles can only evolve within the spherical-shell with thickness δ_c. At $t = 1000\,\mathrm{s}$ the mole fraction profile is significantly affected by the cut-off distance and the evolution of the radius $R(t)$ begins to deviate from the case $\delta_\mathrm{c} = \infty$. This deviation is considerably pronounced at At $t = 2500\,\mathrm{s}$, see Figs 5.11 and 5.12. The estimation of the cut-off distance δ_c depends to a large extent on the quality of the used models for calculating molar volumes and viscosities of the liquid phase. As reported by Tang et al.[175], experimental uncertainties with respect to the underlying viscosity measurements fall in the range of $\pm 25\%$. Other deviations may result from the non-ideal geometry of the alumina particles, as the spherical shape is not exactly maintained during dissolution. Also the size of the dissolving particle is evaluated from a 2D perspective; thus, possible rotation of the particles during the experiment might lead to scattering in the data. Additionally, there may be other significant factors influencing mass flow that are not considered in the current model, such as capillary effects. Taking these aspects into account, the numerical results agree reasonably well with the measurement. However, the kinetics of the dissolution process is predicted to be slightly too fast compared to the experimental data in the final stages of the dissolution.

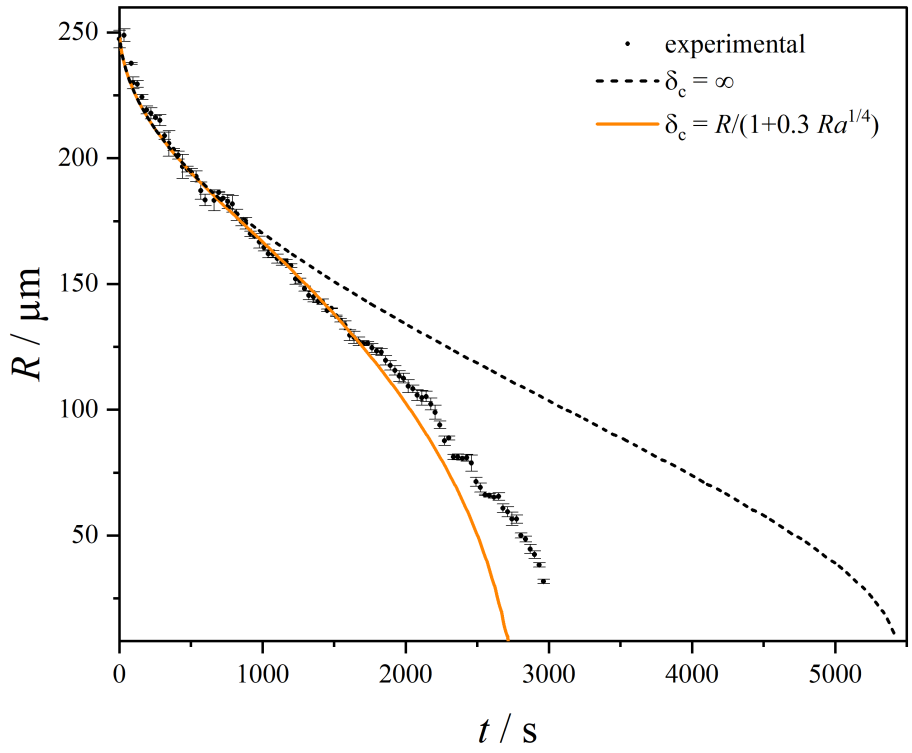

Figure 5.11: Dissolution profile of an alumina particle dissolving at 1500°C in Slag 1.

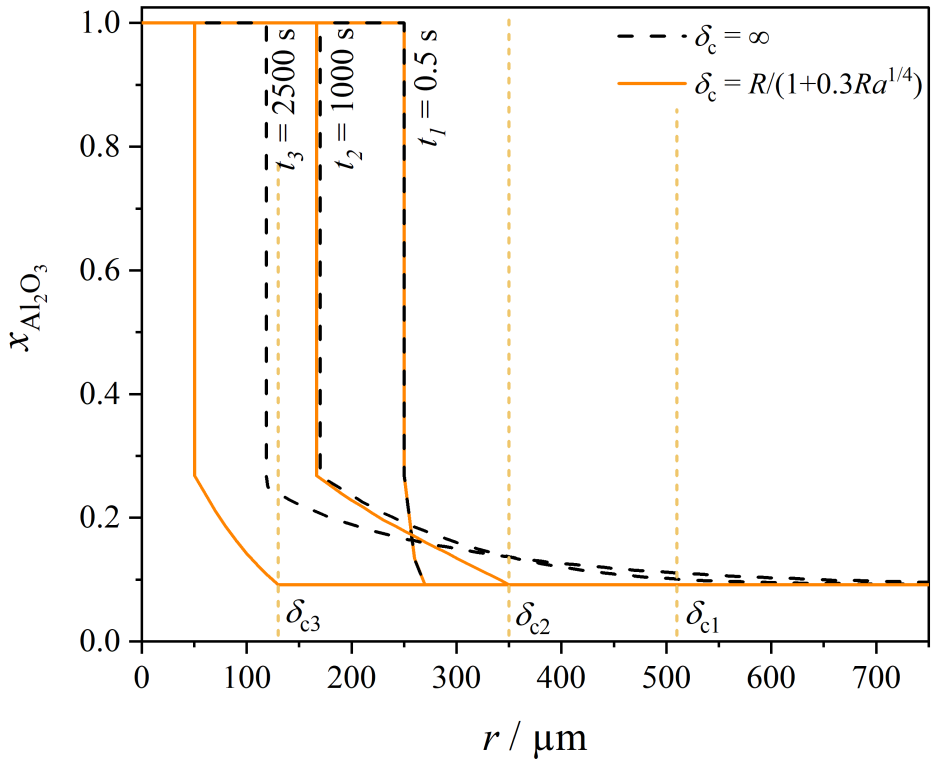

Figure 5.12: Simulated mole fraction profile of alumina during the dissolution of an alumina particle in Slag 1 at three different times, i.e. $t_1 = 0.5\,\mathrm{s}$, $t_2 = 1000\,\mathrm{s}$ and $t_3 = 2500\,\mathrm{s}$. The mole fraction profiles are shown for two cases: in orange, the mole fraction profiles in case of a density driven flow affecting the kinetics of the dissolution. The black dashed lines are the mole fraction profiles in case of a purely diffusion-driven phase transformation. The position $R + \delta_c$ is indicated by means of the orange dashed lines.

Alumina dissolution in Slag 2

Compared to Slag 1, Slag 2 contains much less silica (SiO_2), which functions as a network former in the slag. The composition of Slag 2 is provided in Table 5.5. The content of silica usually results in the formation of silica clusters and networks, which determine the structure of the slag, see e.g. [2, 3]. It seems to be reasonable that a significantly lower viscosity and also higher diffusivities prevails in Slag 2 compared to Slag 1 due to the diminished occurrence of silica clusters in Slag 2. This assumption is confirmed by the values for the interdiffusivities and viscosities provided in Tables 5.6 and 5.9. Consequently, it is expected that the dissolution of alumina in Slag 2 occurs at a faster rate compared to Slag 1. In fact, when observing the dissolution of alumina into Slag 2 through HT-CSLM, it is evident that it proceeds significantly faster, with a total dissolution time of approximately $\tilde{t} \approx 780\,\mathrm{s}$ compared to $\tilde{t} \approx 3100\,\mathrm{s}$ for Slag 1. Figure 5.13 illustrates the progression of the shrinking radius R of the alumina particle in Slag 2. The numerical prediction from the sharp-interface model is compared to the equivalent radius of the alumina particle estimated through image analysis. The values of the interdiffusivities used in the simulations are listed in Table 5.6. The mole fractions $x_{R,\mathrm{CaO}}$, $x_{R,\mathrm{Al_2O_3}}$ and $x_{R,\mathrm{SiO_2}}$, i.e. the boundary conditions at the solid-liquid interface, are presented in Table 5.7.

Similar to Slag 1, the beginning of the dissolution process ($t < 250\,\mathrm{s}$) in Slag 2 can be adequately described by considering multi-component diffusion only (dashed line in Fig 5.13). However, after about 250 s, convection in the liquid phase starts to influence the dissolution kinetics significantly. Similar to the previous case, the density-driven flow determines the cut-off distance δ_c. Initially, the cut-off distance is relatively large but gradually diminishes, eventually disturbing the mole fraction profiles obtained from bulk diffusion. This is shown in Fig 5.14, where the mole fraction profiles of alumina are shown for three different times. At the start of the dissolution, the mole fraction profile is unaffected by the cut-off distance, due to its high value. As δ_c diminishes, the mole fraction profile becomes steeper compared to the purely diffusion-driven case. At this point, convection starts to contribute to the dissolution kinetics. The evolution of the radius $R(t)$ of the particle starts to deviate for these two cases. At $t = 500\,\mathrm{s}$, the position of the solid-liquid interface (i.e. R) is considerably progressed compared to the diffusion-only case (dashed black lines in Fig 5.14). It seems worth mentioning that the flow field around the particle in slag 2 could be temporarily visualized with the HT-CSLM. As a representative example the convective flow is indicated via light orange arrows in Fig 5.15. From Fig 5.13 the prediction from the numerical model (orange line) agrees well with the data obtained from the HT-CSLM experiment.

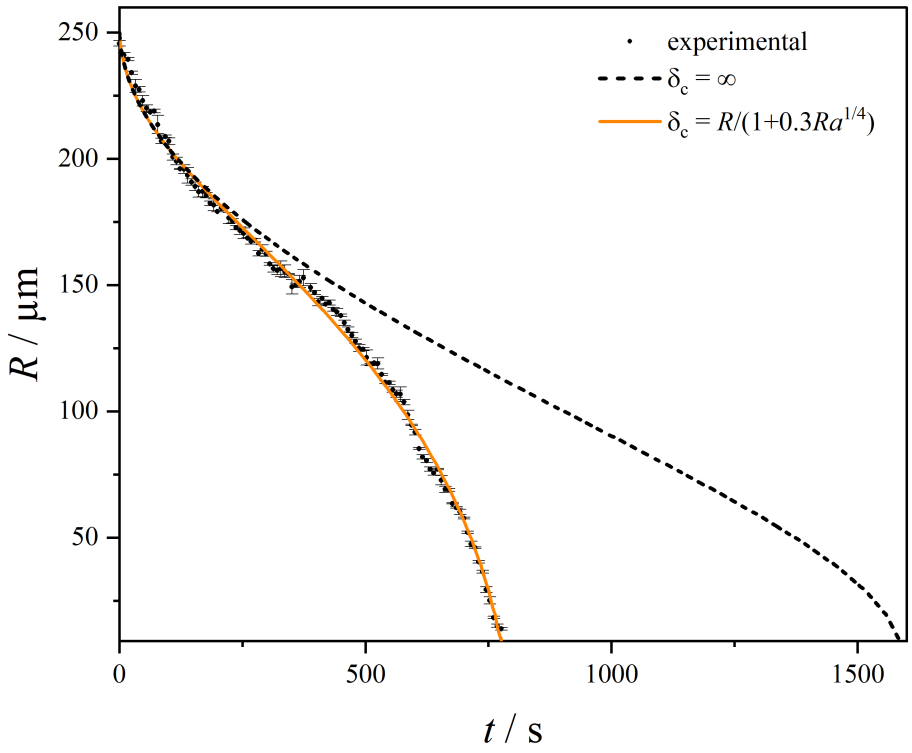

Figure 5.13: Dissolution profile of an alumina particle dissolving at 1500°C in Slag 2.

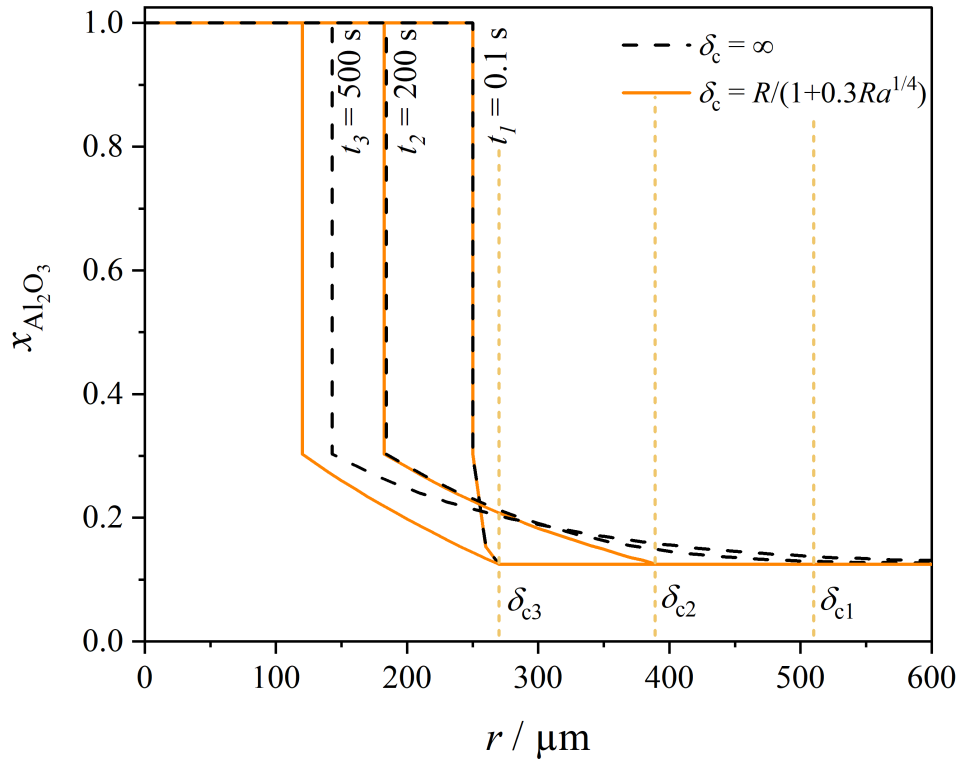

Figure 5.14: Simulated mole fraction profile of alumina during the dissolution of an alumina particle in Slag 2 at three different times, i.e. $t_1 = 0.1\,\mathrm{s}$, $t_2 = 200\,\mathrm{s}$ and $t_3 = 500\,\mathrm{s}$. The mole fraction profiles are shown for two cases: in orange, the mole fraction profiles in case of a density driven flow affecting the kinetics of the dissolution. The black dashed lines are the mole fraction profiles in case of a purely diffusion-driven phase transformation. The position $R + \delta_c$ is indicated by means of the orange dashed lines.

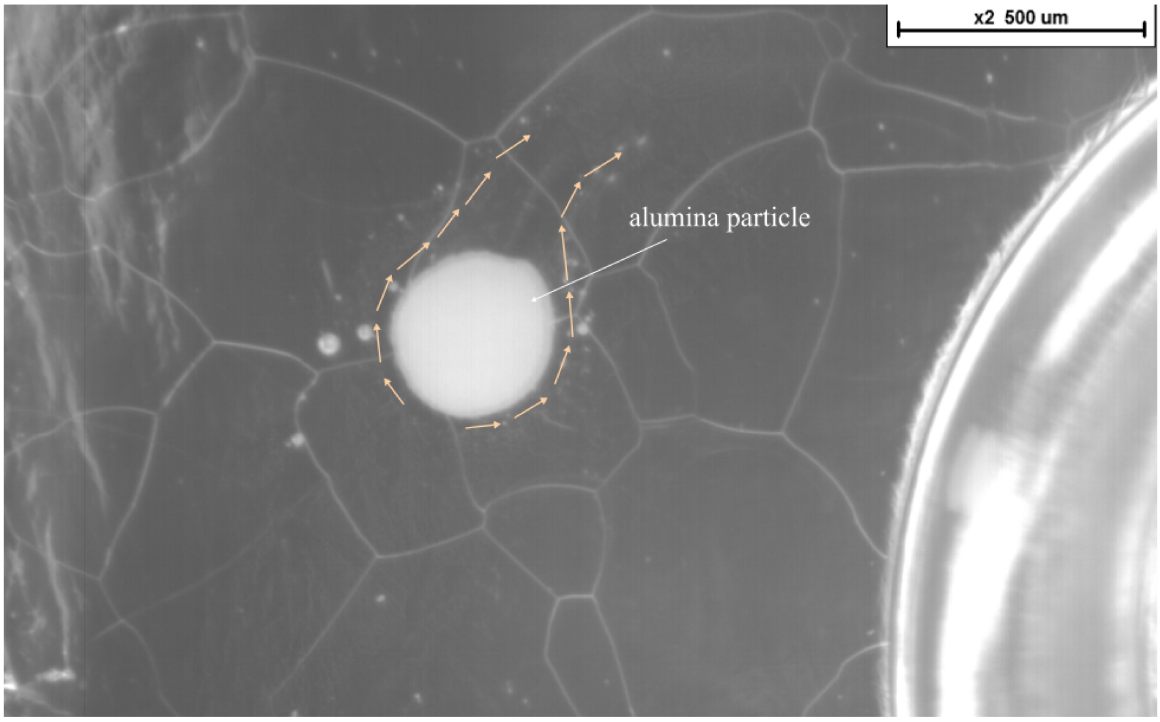

Figure 5.15: Alumina particle dissolving at 1500°C in Slag 2. The flow field around the particle is clearly visible and is indicated via orange arrows.

Alumina dissolution in Slag 3

The composition of Slag 3 is presented in Table 5.5. Looking at the composition of Slag 3, it might be assumed that the viscosity and diffusivities of the slag are between Slag 1 and Slag 2. The diffusivity matrix obtained from [172] and the viscosities calculated from using the relations given in [175] are presented in Table 5.6 and Table 5.9, respectively. Indeed, the above presumption seems to be justified when comparing the values given in these tables. The total dissolution time of Slag 3 is therefore likely to fall between that of Slag 1 and Slag 2. In fact, the total dissolution time for alumina in Slag 3 at 1500°C observed in the HT-CSLM experiment lies between those of Slag 1 and Slag 2 with about 2500 s. The experimentally observed equivalent radius R of the alumina particle in Slag 3 is shown in Fig 5.16 and is compared to results from the numerical model. The dissolution kinetics are simulated by means of multi-component diffusion only. Simulated mole fraction profiles of CaO, Al_2O_3 and SiO_2 at $t = 2400\,\mathrm{s}$ are shown in Fig 5.17. The contribution of natural convection in this case seems to be negligible. It is not entirely clear why convection does not appear to be involved in mass transfer in this case. However, the agreement of the experimental observation with the numerical results when considering only diffusion in the liquid phase seems to be convincing.

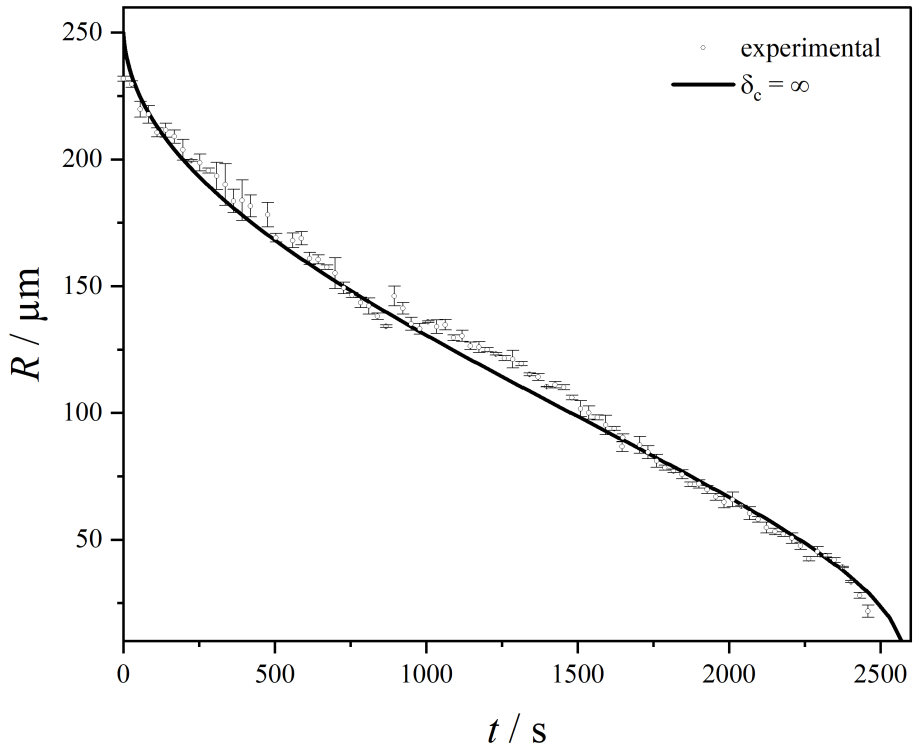

Figure 5.16: Dissolution profile of an alumina particle dissolving at 1500°C in slag 3.

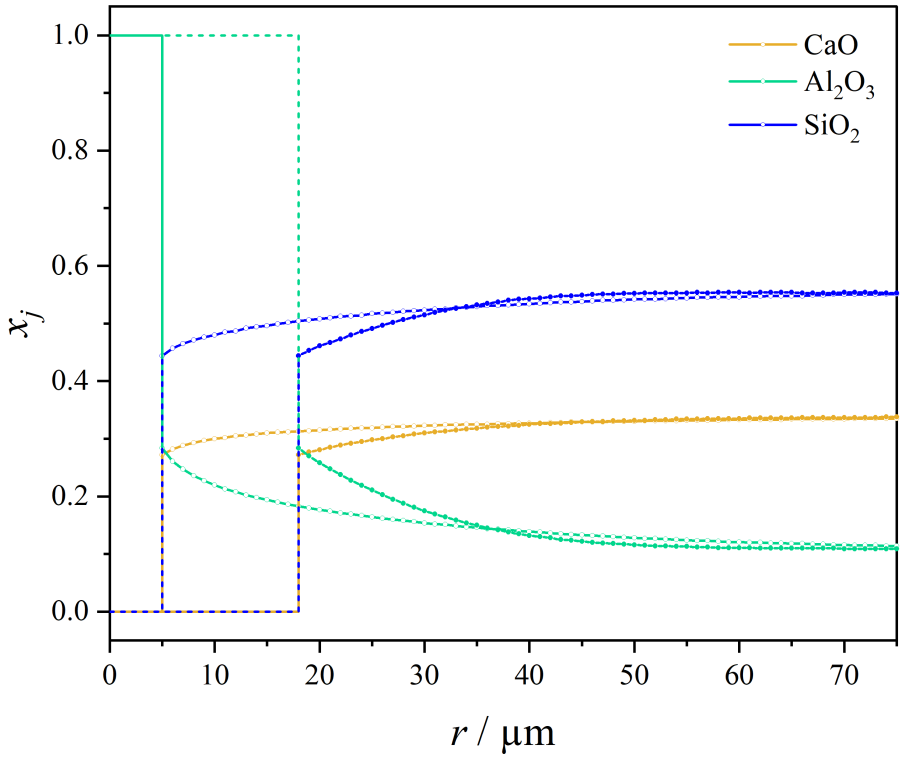

Figure 5.17: Simulated mole fraction profiles at $t = 400\,\mathrm{s}$ (indicated by filled circles) and $t = 2400\,\mathrm{s}$ (indicated by empty circles) during dissolution of an alumina particle in Slag 3 at 1500°C.

5.5 Validity of isothermal mass transport assumptions

The Rayleigh number may also be used to estimate the tendency for thermally induced convection. Thus, it can be used to assess wh the isothermal assumptions made for mass transport are valid. For that the Rayleigh number Ra_{T} is defined as

$$Ra_{\mathrm{T}} = \frac{g\Delta\rho_{\mathrm{T}}L^3}{\eta\alpha} \,, \tag{5.9}$$

where g is the acceleration due to gravity ($\approx 9.81\,\mathrm{ms}^{-2}$), L is the characteristic length and is taken to be the crucible height (4 mm) to account for the most extreme case, $\Delta\rho_{\mathrm{T}}$ is the maximal density difference in the melt that is induced from temperature differences in the melt, α is the thermal diffusivity and η is the viscosity of the melt. The thermal diffusivity α can be calculated from

$$\alpha = \frac{\lambda}{\rho c_P} \,, \tag{5.10}$$

where λ is the thermal conductivity and c_P is the specific heat capacity at constant pressure of the liquid and is calculated from FactSage 7.3 using the FToxid database. The thermal conductivity λ is estimated from Kang and Morita [176] and the values for the individual slags are listed in Table 5.10.

Table 5.10: Thermophysical properties and dimensionless numbers of selected slags at 1773 K. The Rayleigh numbers Ra_{T} are calculated by assuming a temperature difference of $\Delta T = 100\mathrm{K}$ in the melt.

Slag	λ/W m^{-1}K^{-1}	c_P/J kg^{-1}K^{-1}	$\Delta\rho_{\mathrm{T}}$/kg m^{-3}	Ra_{T}	Le
1	0.49	1197.39	15.1	4.4	$1.38 \cdot 10^4$
2	0.34	1190.47	17.2	12.1	$9.45 \cdot 10^2$
3	0.44	1192.71	15.6	6.1	$1.64 \cdot 10^3$

Even for high temperature differences in the melt ($\Delta T = 100\mathrm{K}$), the Rayleigh numbers ranging from 4.4 (for Slag 1) to 12.1 (for Slag 2) are well below the critical values of 650-1000, according to Chandrasekhar [177]. Moreover, the Lewis Le number, which relates the thermal diffusivity with the diffusivity of mass, can be used as an indicator to estimate if the isothermal conditions are fulfilled during experiment [178] and is defined as

$$Le = \alpha/D \,, \tag{5.11}$$

where D is the average diffusion coefficient. The Lewis numbers characterizing the conditions of the above experiments are given in Table 5.10. It can be seen that the thermal diffusivities exceed the average diffusivities for mass transport by 2 to 4 orders of magnitude, supporting the hypothesis of isothermal mass transport. Thus, by interpreting these simple values (Ra_{T} and Le), neglecting thermally induced convective contributions to mass transport seems physically reasonable.

6 | Conclusions and Outlook

A Gibbs energy minimization routine is developed for the calculation of multi-component and multi-phase equilibria in metallurgical slags. The software can be easily integrated into comprehensive metallurgical process models (i.e. the LD-model [27–30]) and in computer routines for simulating the kinetics of congruent and incongruent phase transformations. The software can be utilized to determine the thermodynamic contact conditions occurring at solid-liquid interfaces within multi-component slag systems and can be employed to calculate local equilibria in systems that are not in a state of equilibrium. With regard to oxygen steelmaking, a useful thermodynamic database is composed of openly available thermodynamic assessments to calculate thermodynamic functions and phase boundaries in the CaO-SiO_2-FeO-MgO-MnO-system. Additionally, a sharp-interface model for predicting the kinetics of solid-liquid phase transformations in multi-component, multi-phase slag systems is developed in this work. Numerical predictions of the dissolution kinetics of oxide particles in multi-component slags are assessed by comparing them to experimental observations obtained through the use of HT-CSLM. The following conclusions can be drawn:

- The numerical results of the Gibbs energy minimization routine developed in this work agree well with the calculations from established commercial codes, i.e. Factsage [63]. Moreover, the calculated phase diagrams in the CaO-SiO_2-FeO-MgO-MnO-system are compared to experimental data [137, 138] and to phase diagram data from other assessments [107, 141]. The collected data and calculations demonstrate a satisfactory level of agreement within the defined scope of its application as shown in Fig. 3.5.

- The thermodynamic model developed for the CaO-SiO_2-FeO-MgO-MnO-system presented in this work is applicable exclusively to slags that undergo LD-steelmaking conditions characterized by low oxygen partial pressures. To accurately predict equilibrium states at higher oxygen partial pressures, it is necessary to introduce higher oxidation states of iron and manganese (Fe^{3+}, Mn^{3+})

into the thermodynamic model in the form of additional constituents (Fe_2O_3, Mn_2O_3).

- For modelling dephosphorization reactions the modified quasi-chemical model used in this work requires expansion into a multi-sublattice model. This enhancement is necessary in order to incorporate second-nearest neighbor pair interactions between constituents located on separate sublattices. Moreover, solid solution phases would need to be introduced as the dephosphorization in the LD converter is largely based on the formation of silico-phosphate solid solutions.

- The rate-determining processes of congruent and incongruent solid-liquid phase transformations in metallurgical slags are investigated by comparing the experimentally obtained kinetics of growth and shrinkage of oxide crystals (i.e. wollastonite) in CaO-SiO_2-slags to numerical results using the sharp interface model presented in this work. It is shown that diffusion in the liquid suffices to describe the experimentally observed features of incongruent cyclic partial phase transformations in the CaO-SiO_2 system, whereas the characteristic features of the investigated congruent cyclic partial phase transformations can be described by modelling the kinetics of a reaction at the solid-liquid interface.

- For the dissolution of oxide particles (in the incongruent case) multi-component diffusion in the liquid is identified as the rate limiting step in the case of various oxide particles (i.e. CaO, SiO_2 and Al_2O_3). However, convection might contribute to mass transport and in such cases must be taken into account when predicting the total dissolution time. This is done by calculating the time-dependent thickness of a spherical shell (determined by the cut-off distance parameter δ_c) surrounding the particle. Inside this spherical shell multi-component diffusion occurs undisturbed while outside of it convection "cuts-off" the mole fraction profiles, resulting in homogenization of the melt.

- The major limiting factor in using the developed dissolution model remains the availability of interdiffusion coefficients for liquid slag systems. For some ternary slags interdiffusivities can be found in literature, see e.g. [169, 179]; however, interdiffusivity data remains scarce for multi-component slag systems. For this reason, there is a strong need for more complete interdiffusivity data for predicting the kinetics of diffusive phase transformations in multi-component slag systems. Similar statements can be made regarding viscosity and molar volume data.

- The modelling approach developed in this work might contribute to metallurgical process models for LD-steelmaking or secondary metallurgy. Furthermore,

it might contribute to steel cleanliness applications and improved refractory linings by predicting, e.g. dissolution times of inclusions at different slag compositions and simulating the corrosion of refractory materials in operation.

Appendix

Table 1: Thermodynamic data of unary systems as taken from the FactPS database. The standard enthalpies of formation $\Delta H^0_{298.15,f}$ are provided in $\mathrm{J\,mol^{-1}}$, the heat capacities C^0_p and entropies $S^0_{298.15}$ are given in $\mathrm{J\,mol^{-1}\,K^{-1}}$.

species	$\Delta H^0_{298.15,f}$	$S^0_{298.15}$	C^0_p	applicability range
CaO^{lime}	-635090	37.75	$58.791171 - 1147146\,T^{-2} - 133.904\,T^{-0.5} + 102978788\,T^{-3}$	298K - 2845K
SiO_2^{crist}	-906377	46.03	$83.513598 - 2455360\,T^{-2} - 374.693\,T^{-0.5} + 280072194\,T^{-3}$	298K - 1996K
$Ca_3SiO_5^{hatr}$	-2857015	235.65	$209.98832 - 504.60291\,T^{-0.5}$	298K - 2500K
$Ca_2SiO_4^{C2S\alpha'}$	-2273629	147.79	$210.48877 - 7989399.9\,T^{-2} + 1297479950\,T^{-3} - 701.9\,T^{-0.5}$	298K - 1750K
$Ca_2SiO_4^{C2S\alpha}$	-2307514	119.66	$243.66021 + 30758136\,T^{-3} - 2034.4214\,T^{-0.5}$	298K - 2500K
MgO^{peric}	-601500	26.95	$61.109650 - 621154\,T^{-2} - 296.199\,T^{-0.5} + 5844612\,T^{-3}$	298K - 3098K
MnO^{mang}	-384928	59.83	$46.484240 + 0.00811696\,T - 368192\,T^{-2}$	298K - 2115K
$Ca_2MgSi_2O_7^{aker}$	-3866291	212	$387.06396 - 2938.7690\,T^{-0.5} - 40790480\,T^{-3}$	298K - 2000K
$Ca_3MgSi_2O_8^{merw}$	-4555779	251.77	$453.62 - 3250\,T^{-0.5} - 344230000\,T^{-3}$	298K - 2500K
$Ca_3Si_2O_7^{rank}$	-3950432	205.56	$392.84876 - 10659996\,T^{-2} - 2200.0658\,T^{-0.5} + 1373589130\,T^{-3}$	298K - 5000K
$CaSiO_3^{woll}$	-1634676	79.81	$149.07266 - 3.659348.0\,T^{-2} - 690.29498\,T^{-0.5} + 484349421\,T^{-3}$	298K - 2000K
$CaSiO_3^{ps\text{-}woll}$	-1625507	86.94	$141.15611 - 5857595\,T^{-3}$	298K - 1813
$Mg_2SiO_4^{forst}$	-2177699	94.01	$238.64136 - 2001.261\,T^{-0.5} - 116243281\,T-3$	298K - 3000K
$MgSiO_3^{enst}$	-1545080	66.66	$107.64250 + 0.018582676\,T - 2575452\,T^{-2}$	298K - 2500K
SiO_2^{tridym}	-907045	45.52	$75.372668 - 5958095.1\,T^{-2} + 958246123\,T^{-3}$	298K - 1991K
$Mn_2SiO_4^{teph}$	-1724664	163.2	$512.52\,T - 0.18273\,T + 4602600\,T^{-2} + 0.0000520580016\,T^2 - 6640.4\,T^{-0.5}$	298K - 3000K
$MnSiO_3^{rhod}$	-1321491	102.5	$99.042999 + 0.0191449999\,T - 3040700\,T^{-2} + 274.47\,T^{-0.5}$	298K - 2500K
CaO^{liquid}	-555594	65.69	$58.791171 - 1147146\,T^{-2} - 133.904\,T^{-0.5} + 102978788\,T^{-3}$	298K - 2845K
SiO_2^{liquid}	-896796	50.83	$83.513598 - 2455360\,T^{-2} - 374.693\,T^{-0.5} + 280072194\,T^{-3}$	298K - 1996K
FeO^{liquid}	-234643	78.47	$-18.024474 + 0.0306080599\,T - 2533300\,T^{-2} + 1500.9\,T^{-0.5}$	298K - 1664K
			68.1992	1664K - 2000K
MgO^{liquid}	-545345	27	$72.795562 - 0.003142184\,T + 522751.6\,T^{-2} - 296.199\,T^{-0.5} + 5844612\,T^{-3}$	298K - 3098K
MnO^{liquid}	-330536	85.55	$46.484240 + 0.00811696\,T - 368192\,T^{-2}$	298K - 2115K

Table 2: Molar Gibbs energy functions of unary liquid systems as taken from the FactPS database.

species	$G_m(T)/\mathrm{J\,mol^{-1}}$	applicability range
$\mu^{\circ}_{\mathrm{liq,CaO}}$	$-571766.658 + 348.735802\,T + 573572.991\,T^{-1} - 535.615998\,T^{0.5} - 17163131.3\,T^{-2} - 58.7911706\,T\ln(T)$	298K - 2845K
$\mu^{\circ}_{\mathrm{liq,SiO_2}}$	$-915415.778 + 562.199392\,T + 1227679.99\,T^{-1} - 1498.77200\,T^{0.5} - 46678699.1\,T^{-2} - 83.5135981\,T\ln(T)$	298K - 1996K
$\mu^{\circ}_{\mathrm{liq,FeO}}$	$-290958.454 - 349.657168\,T - 0.01530402997\,T^2 + 1266650.00\,T^{-1} + 6003.60001\,T^{0.5} + 18.0244741\,T\ln(T)$	298K - 1664K
	$-268094.665 + 398.288735\,T - 68.1992000\,T\ln(T)$	1664K - 2000K
$\mu^{\circ}_{\mathrm{liq,MgO}}$	$-554894.205 + 490.908663\,T + 0.001571092\,T^2 - 261375.798\,T^{-1} - 1184.79600\,T^{0.5} - 974102.005\,T^{-2} - 72.7955625\,T\ln(T)$	298K - 3098K
$\mu^{\circ}_{\mathrm{liq,MnO}}$	$-345990.970 + 230.277102\,T - 0.004058480000\,T^2 + 184096.000\,T^{-1} - 46.4842400\,T\ln(T)$	298K - 2115K

Table 3: Molar Gibbs energy functions of unary solid systems taken from the FactPS database.

species	$G_m(T)/\mathrm{J\,mol^{-1}}$	applicability range
$\mu^{\circ}_{\mathrm{lime,CaO}}$	$-651262.658 + 376.676564\,T + 573572.991\,T^{-1} - 535.615998\,T^{0.5} - 17163131.3\,T^{-2} - 58.7911706\,T\ln(T)$	298K - 2845K
$\mu^{\circ}_{\mathrm{crist,SiO_2}}$	$-924997.138 + 566.999695\,T + 1227679.99\,T^{-1} - 1498.77200\,T^{0.5} - 46678699.1\,T^{-2} - 83.5135981\,T\ln(T)$	298K - 1996K
$\mu^{\circ}_{\mathrm{hatr,Ca_3SiO_5}}$	$-2902196.94 + 1229.21802\,T - 2018.41164\,T^{0.5} - 209.988320\,T\ln(T)$	298K - 2500K
$\mu^{\circ}_{\mathrm{C2S}\alpha',\mathrm{Ca_2SiO_4}}$	$-2331645.86 + 1371.89957\,T + 3994699.94\,T^{-1} - 216246659\,T^{-2} - 2807.60006\,T^{0.5} - 210.488764\,T\ln(T)$	298K - 1710K
$\mu^{\circ}_{\mathrm{C2S}\alpha,\mathrm{Ca_2SiO_4}}$	$-2241869.07 + 947.186107\,T + 3994699.94\,T^{-1} - 216246659.\,T^{-2} - 2807.60006\,T^{0.5} - 160.488767\,T\ln(T)$	298K - 5000K
$\mu^{\circ}_{\mathrm{peric,MgO}}$	$-611541.379 + 420.064762\,T + 310577.002\,T^{-1} - 1184.79600\,T^{0.5} - 974102.005\,T^{-2} - 61.1096505\,T\ln(T)$	298K - 3098K
$\mu^{\circ}_{\mathrm{mang,MnO}}$	$-400382.970 + 255.992539\,T - 0.00405848\,T^2 + 184096.000\,T^{-1} - 46.4842400\,T\ln(T)$	298K - 2115K
$\mu^{\circ}_{\mathrm{aker,Ca_2MgSi_2O_7}}$	$3880436.17 + 2721.30231\,T - 11755.0760\,T^{0.5} + 6798413.33\,T^{-2} - 387.063961\,T\ln(T)$	298K - 2000K
$\mu^{\circ}_{\mathrm{merw,Ca_3MgSi_2O_8}}$	$-4580726.46 + 3167.16334\,T - 13000\,T^{0.5} + 57371666.7\,T^{-2} - 453.620000\,T\ln(T)$	298K - 2500K
$\mu^{\circ}_{\mathrm{rank,Ca_3Si_2O_7}}$	$-4019610.62 + 2723.09959\,T + 5329997.77\,T^{-1} - 8800.26331\,T^{0.5} - 228931522.\,T^{-2} - 392.848756\,T\ln(T)$	298K - 5000K
$\mu^{\circ}_{\mathrm{woll,CaSiO_3}}$	$-1664832.94 + 1013.06077\,T + 1829673.99\,T^{-1} - 2761.17992\,T^{0.5} - 80724903.6\,T^{-2} - 149.072661\,T\ln(T)$	298K - 2000K
$\mu^{\circ}_{\mathrm{ps\text{-}woll,CaSiO_3}}$	$-1667538.65 + 927.913022\,T + 2928797.49\,T^{-1} - 1668.92799\,T^{0.5} - 156789159.\,T^{-2} - 141.156110\,T\ln(T)$	298K - 1813K
$\mu^{\circ}_{\mathrm{forst,Mg_2SiO_4}}$	$-2180392.41 + 1737.57718\,T - 8005.04402\,T^{0.5} + 19373880.2\,T^{-2} - 238.641360\,T\ln(T)$	298K - 3000K
$\mu^{\circ}_{\mathrm{enst,MgSiO_3}}$	$-1572754.95 + 615.004096\,T - 0.007528365500\,T^2 + 1287726.00\,T^{-1} - 101.189699\,T\ln(T)$	298K - 3000K
$\mu^{\circ}_{\mathrm{tridy,SiO_2}}$	$-944111.184 + 480.752826\,T + 2979047.54\,T^{-1} - 159707687\,T^{-2} - 75.3726680\,T\ln(T)$	298K - 1991K
$\mu^{\circ}_{\mathrm{teph,Mn_2SiO_4}}$	$-1625052.58 + 3960.53941\,T + 0.09136499966\,T^2 - 2301300.00\,T^{-1} - 8.676333604^{-6}T^3 - 26561.6002\,T^{0.5} - 512.52\,Tln(T)$	298K - 3000K
$\mu^{\circ}_{\mathrm{rhod,MnSiO_3}}$	$-1371548.39 + 551.869975\,T - 90.00572499962\,T^2 + 1520350\,T^{-1} + 1097.87999\,T^{0.5} - 99.0429995\,T\ln(T)$	298K - 2500K

Table 4: Binary interaction parameters for calculating the Gibbs energy of the liquid phase.

Parameter	Value / (J mol^{-1})	Reference
$\Delta g^{\circ}_{\mathrm{liq,CaO,SiO_2}}$	-158217.42 + 19.455475 T	[122]
$L^{01}_{\mathrm{liq,CaO,SiO_2}}$	- 37931.997	[122]
$L^{05}_{\mathrm{liq,CaO,SiO_2}}$	- 90147.924	[122]
$L^{07}_{\mathrm{liq,CaO,SiO_2}}$	439890.86 - 133.888 T	[122]
$\Delta g^{\circ}_{\mathrm{liq,SiO_2,FeO}}$	-30497.176 + 14.294163 T	[134] optimized
$L^{02}_{\mathrm{liq,SiO_2,FeO}}$	14154.472	[134] optimized
$L^{60}_{\mathrm{liq,SiO_2,FeO}}$	375706.46 - 140.58658 T	[134] optimized
$\Delta g^{\circ}_{\mathrm{liq,CaO,FeO}}$	-38074.4	[132]
$L^{01}_{\mathrm{liq,CaO,FeO}}$	-13807.2	[132]
$\Delta g^{\circ}_{\mathrm{liq,CaO,MgO}}$	45329	[140]
$L^{10}_{\mathrm{liq,CaO,MgO}}$	-30583	[140]
$\Delta g^{\circ}_{\mathrm{liq,CaO,MnO}}$	27006	[140]
$\Delta g^{\circ}_{\mathrm{liq,SiO_2,MgO}}$	-86090	[139]
$L^{10}_{\mathrm{liq,SiO_2,MgO}}$	-48974 + 37.656 T	[139]
$L^{70}_{\mathrm{liq,SiO_2,MgO}}$	328109 - 125.52 T	[139]
$\Delta g^{\circ}_{\mathrm{liq,SiO_2,MnO}}$	-79946 + 20.92 T	[122]
$L^{70}_{\mathrm{liq,SiO_2,MnO}}$	228819 - 62.76 T	[122]
$\Delta g^{\circ}_{\mathrm{liq,FeO,MgO}}$	10460	[123]
$\Delta g^{\circ}_{\mathrm{liq,MnO,MgO}}$	4184	[140]

Table 5: Ternary interaction parameters for calculating the Gibbs energy of the liquid phase.

Parameter	Value / (J mol^{-1})	Reference
$L^{003}_{\mathrm{liq,CaO,SiO_2,(FeO)}}$	3347.2	optimized
$L^{101}_{\mathrm{liq,SiO_2,FeO,(CaO)}}$	-59432.288	optimized
$L^{023}_{\mathrm{liq,SiO_2,FeO,(CaO)}}$	129704	optimized
$L^{102}_{\mathrm{liq,SiO_2MgO,(MnO)}}$	-10460	[130]
$L^{102}_{\mathrm{liq,SiO_2MnO,(MgO)}}$	8368	[130]
$L^{001}_{\mathrm{liq,CaOFeO,(MnO)}}$	-33472	[136]
$L^{101}_{\mathrm{liq,FeOMnO,(SiO_2)}}$	-8368	[135]
$L^{001}_{\mathrm{liq,MgO,SiO_2,(CaO)}}$	4184	[126]
$L^{001}_{\mathrm{liq,CaO,SiO_2,(MgO)}}$	8368	[126]
$L^{021}_{\mathrm{liq,CaO,SiO_2,(MgO)}}$	-29288	[126]
$L^{011}_{\mathrm{liq,CaO,SiO_2,(MnO)}}$	8368	[125]
$L^{101}_{\mathrm{liq,MgO,SiO_2,(FeO)}}$	20920	[127]

Table 6: Coordination numbers in the liquid phase.

Coordination number	Value
$Z^{\mathrm{CaO}}_{\mathrm{liq,CaO,CaO_2}}$	1.37744375
$Z^{\mathrm{FeO}}_{\mathrm{liq,FeO,FeO_2}}$	1.37744375
$Z^{\mathrm{SiO_2}}_{\mathrm{liq,SiO_2,SiO_2}}$	2.75448875
$Z^{\mathrm{MgO}}_{\mathrm{liq,MgO,MgO_2}}$	1.37744375
$Z^{\mathrm{MnO}}_{\mathrm{liq,MnO,MnO_2}}$	1.37744375

Bibliography

[1] K.-R. Hegemann and R. Guder. *Stahlerzeugung*. Springer Fachmedien Wiesbaden, Wiesbaden, 2020.

[2] R. J. Fruehan. *The making, shaping, and treating of steel*. AISE Steel Foundation, Pittsburgh PA, 11th edition, 1998.

[3] K. C. Mills, M. Hayashi, L. Wang, and T. Watanabe. The structure and properties of silicate slags. In S. Seetharaman, A. McLean, R. Guthrie, and S. Sridhar, editors, *Treatise on process metallurgy*, pages 149–286. Elsevier, Amsterdam, 2013.

[4] K. Koch and D. Janke. *Schlacken in der Metallurgie*. Verlag Stahleisen, Düsseldorf, 1984.

[5] H. Burghardt, G. Neuhof, and S. Krauß. *Stahlerzeugung*. VEB Deutscher Verlag für Grundstoffindustrie, Leipzig, 1982.

[6] R. Baciocchi, G. Costa, E. Di Bartolomeo, A. Polettini, and R. Pomi. Carbonation of stainless steel slag as a process for CO_2 storage and slag valorization. *Waste Biomass Valor*, 1(4):467–477, 2010.

[7] G. Li and M. Guo. Current development of slag valorisation in China. *Waste Biomass Valor*, 5(3):317–325, 2014.

[8] M. Morone, G. Costa, A. Polettini, R. Pomi, and R. Baciocchi. Valorization of steel slag by a combined carbonation and granulation treatment. *Miner Eng*, 59:82–90, 2014.

[9] C. Liu, S. Huang, P. Wollants, B. Blanpain, and M. Guo. Valorization of BOF steel slag by reduction and phase modification: Metal recovery and slag valorization. *Metall Mater Trans B*, 48(3):1602–1612, 2017.

[10] S. M. Andrés-Vizán, J. M. Villanueva-Balsera, J. V. Álvarez-Cabal, and G. M. Martínez-Huerta. Classification of BOF slag by data mining techniques according to chemical composition. *Sustainability*, 12(8):3301, 2020.

[11] P. Das, S. Upadhyay, S. Dubey, and K. K. Singh. Waste to wealth: Recovery of value-added products from steel slag. *J Environ Chem Eng*, 9(4):105640, 2021.

[12] Z. Liu, H. Zeng, and F. Wang. Development of high performance carbonatable concrete for steel slag valorization. *Constr Build Mater*, 291:123317, 2021.

[13] R. Ragipani, S. Bhattacharya, and A. K. Suresh. A review on steel slag valorisation via mineral carbonation. *React Chem Eng*, 6(7):1152–1178, 2021.

[14] A. Piemonti, A. Conforti, L. Cominoli, A. Luciano, G. Plizzari, and S. Sorlini. Exploring the potential for steel slags valorisation in an industrial symbiosis perspective at meso-scale level. *Waste Biomass Valorization*, pages 1–21, 2022.

[15] T. Vert. *Refractory Material Selection for Steelmaking*. John Wiley & Sons, Hoboken, New Jersey, 2016.

[16] E. T. Turkdogan. *Fundamentals of Steelmaking*. The Inst of Materials, London, 1996.

[17] W. M. Haynes and D. R. Lide, editors. *CRC handbook of chemistry and physics: A ready-reference book of chemical and physical data*. CRC Press and Taylor & Francis, Boca Raton, Fla. and London, 92nd edition, 2011.

[18] M. Valdez, G. S. Shannon, and S. Sridhar. The ability of slags to absorb solid oxide inclusions. *ISIJ Int*, 46(3):450–457, 2006.

[19] L. E. K. Holappa and A. S. Helle. Inclusion control in high-performance steels. *J Mater Process Technol*, 53:177–186, 1995.

[20] W. D. Cho and P. Fan. Diffusional dissolution of alumina in various steelmaking slags. *ISIJ Int*, 44(2):229–234, 2004.

[21] B. J. Monaghan, L. Chen, and J. Sorbe. Comparative study of oxide inclusion dissolution in CaO–SiO_2–Al_2O_3 slag. *Ironmaking Steelmaking*, 32(3):258–264, 2005.

[22] Y. Sahai and T. Emi. *Tundish technology for clean steel production*. World Scientific, Hackensack NJ, 2008.

[23] Y.-J. Park, Y.-M. Cho, W.-Y. Cha, and Y.-B. Kang. Dissolution kinetics of alumina in molten CaO–Al_2O_3 –FetO–MgO–SiO_2 oxide representing the RH slag in steelmaking process. *J Am Ceram Soc*, 103(3):2210–2224, 2020.

[24] B. A. Webler and P. C. Pistorius. A review of steel processing considerations for oxide cleanliness. *Metall Mater Trans B*, 51(6):2437–2452, 2020.

[25] J. H. Shin, Y. Chung, and J. H. Park. Refractory–slag–metal–inclusion multiphase reactions modeling using computational thermodynamics: Kinetic model for prediction of inclusion evolution in molten steel. *Metall Mater Trans B*, 48(1):46–59, 2017.

[26] C. Liu, D. Kumar, B. A. Webler, and P. C. Pistorius. Calcium modification of inclusions via slag/metal reactions. *Metall Mater Trans B*, 51(2):529–542, 2020.

[27] Y. Lytvynyuk. *Thermodynamic and kinetic modeling of metallurgical reactions*. PhD thesis Montanuniversität Leoben, Austria, 2013.

[28] Y. Lytvynyuk, J. Schenk, M. Hiebler, and A. Sormann. Thermodynamic and kinetic model of the converter steelmaking process. part 1: The description of the BOF model. *steel res int*, 85(4):537–543, 2014.

[29] Y. Lytvynyuk, J. Schenk, M. Hiebler, and A. Sormann. Thermodynamic and kinetic model of the converter steelmaking process. part 2: The model validation. *steel res int*, 85(4):544–563, 2014.

[30] P. Bundschuh. *Thermodynamische und kinetische Modellierung von LD-Konvertern*. PhD thesis Montanuniversität Leoben, Leoben, Austria, 2017.

[31] M. Matsushima, S. Yadoomaru, K. Mori, and Y. Kawai. A fundamental study on the dissolution rate of solid lime into liquid slag. *Trans ISIJ*, 17:442–449, 1977.

[32] N. Maruoka, A. Ishikawa, H. Shibata, and S.-y. Kitamura. Dissolution rate of various limes into steelmaking slag. *High Temp Mater Proc*, 32(1):15–24, 2013.

[33] E. Cheremisina, J. Schenk, L. Nocke, A. Paul, and G. Wimmer. Influence of magnesium oxide content on kinetics of lime dissolution in steelmaking slags. *ISIJ Int*, 57(2):304–313, 2017.

[34] E. Cheremisina, J. Schenk, L. Nocke, A. Paul, and G. Wimmer. Kinetics and mechanisms of dolime dissolution in steelmaking slag. *Metall Mater Trans B*, 50(3):1269–1276, 2019.

[35] N. Lindman and D. Simonsson. On the application of the shrinking core model to liquid-solid reactions. *Chem Eng Sci*, 34:31–35, 1979.

[36] S. Sridhar and A. W. Cramb. Kinetics of Al_2O_3 dissolution in CaO-MgO-SiO_2-Al_2O_3 slags: In situ observations and analysis. *Metall Mater Trans B*, 31:406–410, 2000.

[37] L. K. Elliott, J. A. Lucas, J. Happ, J. Patterson, H. Hurst, and T. F. Wall. Rate limitations of lime dissolution into coal ash slag. *Energy Fuels*, 22(6):3626–3630, 2008.

[38] X. Guo, Z. H. I. Sun, J. van Dyck, M. Guo, and B. Blanpain. In situ observation on lime dissolution in molten metallurgical slags – kinetic aspects. *Ind Eng Chem Res*, 53(15):6325–6333, 2014.

[39] K. Miao, A. Haas, M. Sharma, W. Mu, and N. Dogan. In situ observation of calcium aluminate inclusions dissolution into steelmaking slag. *Metall Mater Trans B*, 49(4):1612–1623, 2018.

[40] C. Xuan and W. Mu. A mechanism theory of dissolution profile of oxide particles in oxide melt. *J Am Ceram Soc*, 104(1):57–75, 2021.

[41] O. Levenspiel. *Chemical Reaction Engineering*. John Wiley & Sons, New York, 3rd edition, 1999.

[42] S. Feichtinger, S. K. Michelic, Y.-B. Kang, and C. Bernhard. In situ observation of the dissolution of SiO_2 particles in CaO-Al_2O_3-SiO_2 slags and mathematical analysis of its dissolution pattern. *J Am Ceram Soc*, 97(1):316–325, 2014.

[43] R. Sarkar, R. Ushasi, and D. Gosh. A model for dissolution of lime in steelmaking slags. *Metall Mater Trans B*, 47(4):2651–2665, 2016.

[44] M. E. Glicksman. *Diffusion in Solids: Field Theory, Solid-State Principles, and Applications*. John Wiley & Sons, New York, 2000.

[45] K. W. Yi, C. Tse, J.-H. Park, M. Valdez, A. W. Cramb, and S. Sridhar. Determination of dissolution time of Al_2O_3 and MgO inclusions in synthetic Al_2O_3-CaO-MgO slags. *Scand J Metall*, 32:177–184, 2003.

[46] J. Liu, F. Verhaeghe, M. Guo, B. Blanpain, and P. Wollants. In situ observation of the dissolution of spherical alumina particles in CaO-Al_2O_3-SiO_2 melts. *J Am Ceram Soc*, 90(12):3818–3824, 2007.

[47] Z. H. I. Sun, X. Guo, J. van Dyck, M. Guo, and B. Blanpain. Phase evolution and nature of oxide dissolution in metallurgical slags. *AIChE J*, 59(8):2907–2916, 2013.

[48] S. Michelic, J. Goriupp, S. Feichtinger, Y.-B. Kang, C. Bernhard, and J. Schenk. Study on oxide inclusion dissolution in secondary steelmaking slags using high temperature confocal scanning laser microscopy. *steel res int*, 87(1):57–67, 2016.

[49] M. J. Whelan. On the kinetics of precipitate dissolution. *Met Sci J*, 3:95–97, 1969.

[50] X. Guo, J. Sietsma, Y. Yang, Z. Sun, and M. Guo. Diffusion-limited dissolution of spherical particles: A critical evaluation and applications of approximate solutions. *AIChE J*, 63(7):2926–2934, 2017.

[51] F. Verhaeghe, S. Arnout, B. Blanpain, and P. Wollants. Lattice boltzmann model for diffusion-controlled dissolution of solid structures in multicomponent liquids. *Phys Rev E*, 72(3 Pt 2):036308, 2005.

[52] F. Verhaeghe, S. Arnout, B. Blanpain, and P. Wollants. Lattice-boltzmann modeling of dissolution phenomena. *Phys Rev E*, 73(3 Pt 2):036316, 2006.

[53] F. Verhaeghe, J. Liu, M. Guo, S. Arnout, B. Blanpain, and P. Wollants. Dissolution and diffusion behavior of Al_2O_3 in a CaO–Al_2O_3–SiO_2 liquid: An experimental-numerical approach. *Appl Phys Lett*, 91(12):124104, 2007.

[54] F. Verhaeghe, J. Liu, M. Guo, S. Arnout, B. Blanpain, and P. Wollants. Determination of the dissolution mechanism of Al_2O_3 in CaO-Al_2O_3-SiO_2 liquids using a combined experimental-numerical approach. *J Appl Phys*, 103(2):023506, 2008.

[55] T. Krüger, H. Kusumaatmaja, A. Kuzmin, O. Shardt, G. Silva, and E. M. Viggen. *The Lattice Boltzmann Method*. Springer International Publishing, Cham, 2017.

[56] L.-S. Luo and S. S. Girimaji. Theory of the lattice boltzmann method: two-fluid model for binary mixtures. *Phys Rev E*, 67:036302, 2003.

[57] S. Chapman and T.G Cowling. *The Mathematical Theory of Non-uniform Gases: An Account of the Kinetic Theory of Viscosity, Thermal Conduction and Diffusion in Gases*. Cambridge University Press, Cambridge, 3rd edition, 1970.

[58] A. A. Mohamad. *Lattice Boltzmann Method*. Springer London, London, 2019.

[59] G. Tripathi, A. Malfliet, B. Blanpain, and M. Guo. Dissolution behavior and phase evolution during aluminum oxide dissolution in BOF slag. *Metall Mater Trans B*, 50(4):1782–1790, 2019.

[60] J. Heulens, B. Blanpain, and N. Moelans. A phase field model for isothermal crystallization of oxide melts. *Acta Mater*, 59(5):2156–2165, 2011.

[61] J. Liu, J. Zou, M. Guo, and N. Moelans. Phase field simulation study of the dissolution behavior of Al_2O_3 into CaO–Al_2O_3–SiO_2 slags. *Comput Mater Sci*, 119:9–18, 2016.

[62] S. Petersen and K. Hack. The thermochemistry library ChemApp and its applications. *Int J Mat Res*, 98(10):935–945, 2007.

[63] C. W. Bale, E. Bélisle, P. Chartrand, S. A. Decterov, G. Eriksson, K. Hack, I.-H. Jung, Y.-B. Kang, J. Melançon, A. D. Pelton, C. Robelin, and S. Petersen. FactSage thermochemical software and databases — recent developments. *Calphad*, 33(2):295–311, 2009.

[64] K. Hack, editor. *The SGTE casebook: Thermodynamics at work*. Woodhead publishing in materials. CRC Press, New York, 2nd edition, 2008.

[65] W. R. Smith and R. W. Missen. *Chemical Reaction Equilibrium Analysis: Theory and Algorithms*. Wiley, New York, 1982.

[66] G. Wedler. *Lehrbuch der Physikalischen Chemie*. Weinheim, 5th edition, 2004.

[67] Leonard M. Naphtali. Complex chemical equilibria by minimizing free energy. *J Chem Phys*, 31(1):263–264, 1959.

[68] Leonard M. Naphtali. Calculate complex chemical equilibria. *Ind Eng Chem*, 53(5):387–388, 1961.

[69] W. R. Smith and R. W. Missen. Calculating complex chemical equilibria by an improved reaction-adjustment method. *Can J Chem Eng*, 46:269–272, 1968.

[70] F. C. H. Wong. *Chemical equilibrium analysis of combustion products at constant volume*. PhD thesis University of Toronto, Toronto, Canada, 2001.

[71] J. M. Paz-García, B. Johannesson, L. M. Ottosen, A. B. Ribeiro, and J. M. Rodríguez-Maroto. Computing multi-species chemical equilibrium with an algorithm based on the reaction extents. *Comput Chem Eng*, 58:135–143, 2013.

[72] J. J. Baeza-Baeza, F. F. Pérez-Pla, and M. C. García-Álvarez-Coque. Teaching chemical equilibria using open source software OCTAVE. *World J Chem Educ*, 3(6):127–133, 2015.

[73] J. Snider, I. Griva, X. Sun, and M. Emelianenko. Set based framework for gibbs energy minimization. *Calphad*, 48:18–26, 2015.

[74] A. M. M. Leal, D. A. Kulik, W. R. Smith, and M. O. Saar. An overview of computational methods for chemical equilibrium and kinetic calculations for geochemical and reactive transport modeling. *Pure Appl Chem*, 89(5):597–643, 2017.

[75] G. Eriksson. Thermodynamic studies of high temperature equilibria: Iii. solgas, a computer program for calculating the composition and heat condition of an equilibrium mixture. *Acta Chem Scand*, 25(7):2651–2658, 1971.

[76] M. Hillert. Some viewpoints on the use of a computer for calculating phase diagrams. *Physica B*, 103:31–40, 1981.

[77] H. L. Lukas, J. Weiss, and E.-T. Henig. Strategies for the calculation of phase diagrams. *Calphad*, 6(3):229–251, 1982.

[78] C. E. Harvie, J. P. Greenberg, and J. H. Weare. A chemical equilibrium algorithm for highly non-ideal multiphase systems: Free energy minimization. *Geochim Cosmochim Acta*, 51:1045–1057, 1987.

[79] C. A. Meyer. *Calculation of chemical and phase equilibria*. PhD thesis at University of Cape Town, Cape Town, South Africa, 1996.

[80] J.-P. Harvey, G. Eriksson, D. Orban, and P. Chartrand. Global minimization of the gibbs energy of multicomponent systems involving the presence of order/disorder phase transitions. *Am J Sci*, 313(3):199–241, 2013.

[81] M. H. A. Piro, S. Simunovic, T. M. Besmann, B. J. Lewis, and W. T. Thompson. The thermochemistry library Thermochimica. *Comput Mater Sci*, 67:266–272, 2013.

[82] B. Sundman, X.-G. Lu, and H. Ohtani. The implementation of an algorithm to calculate thermodynamic equilibria for multi-component systems with non-ideal phases in a free software. *Comput Mater Sci*, 101:127–137, 2015.

[83] M. Hülsmann, B. Klaassen, A. Krämer, O. Krämer-Fuhrmann, T. Pangalela, D. Reith, K. Hack, and J. Linden. Calculation of chemical equilibria in multiphase: Multicomponent systems. In M. Griebel, A. Schüller, and M. A.

Schweitzer, editors, *Scientific Computing and Algorithms in Industrial Simulations*, pages 3–24. Springer International Publishing, Cham, 2017.

[84] B. Sundman, N. Dupin, and B. Hallstedt. Algorithms useful for calculating multi-component equilibria, phase diagrams and other kinds of diagrams. *Calphad*, 75:102330, 2021.

[85] S.-L. Chen, S. Daniel, F. Zhang, Y. A. Chang, X.-Y. Yan, F.-Y. Xie, R. Schmid-Fetzer, and W. A. Oates. The PANDAT software package and its applications. *Calphad*, 26(2):175–188, 2002.

[86] J.-O. Andersson, T. Helander, L. Höglund, P. Shi, and B. Sundman. THERMO-CALC & DICTRA, computational tools for materials science. *Calphad*, 26(2):273–312, 2002.

[87] C. W. Bale, E. Bélisle, P. Chartrand, S. A. Decterov, G. Eriksson, A. E. Gheribi, K. Hack, I.-H. Jung, Y.-B. Kang, J. Melançon, A. D. Pelton, S. Petersen, C. Robelin, J. Sangster, P. Spencer, and M-A. van Ende. FactSage thermochemical software and databases, 2010–2016. *Calphad*, 54:35–53, 2016.

[88] H. L. Lukas, S. G. Fries, and B. Sundman. *Computational thermodynamics: The CALPHAD method*. Cambridge University Press, Cambridge and New York, 2007.

[89] R. Gautam and W. D. Seider. Computation of phase and chemical equilibrium: Part I. local and constrained minima in gibbs free energy. *AIChE J*, 25(6):991–999, 1979.

[90] F. C. Weber. Convergence of the equilibrium code SOLGASMIX. *J Comput Phys*, (145):655–670, 1998.

[91] G. Eriksson and K. Hack. ChemSage - a computer program for the calculation of complex chemical equilibria. *Metall Trans B*, 21:1013–1023, 1990.

[92] M. H. A. Piro. Updating the estimated assemblage of stable phases in a gibbs energy minimizer. *Calphad*, 58:115–121, 2017.

[93] M. H. A. Piro and S. Simunovic. Global optimization algorithms to compute thermodynamic equilibria in large complex systems with performance considerations. *Comput Mater Sci*, 118:87–96, 2016.

[94] G. Eriksson and W. T. Thompson. A procedure to estimate equilibrium concentrations in multicomponent systems and related applications. *Calphad*, 13(4):389–400, 1989.

[95] M.H.A. Piro and S. Simunovic. Performance enhancing algorithms for computing thermodynamic equilibria. *Calphad*, 39:104–110, 2012.

[96] E. Anderson, Z. Bai, C. Bischof, L. S. Blackford, J. Demmel, J. Dongarra, J. Du Croz, A. Greenbaum, S. Hammarling, A. McKenney, and D. Sorensen. *LAPACK users' guide*, volume 9 of *Software, environments, tools*. SIAM Soc. for Industrial and Applied Mathematics, Philadelphia, Pa., 3rd edition, 1999.

[97] C. R. Harris, K. J. Millman, S. J. van der Walt, R. Gommers, P. Virtanen, D. Cournapeau, E. Wieser, J. Taylor, S. Berg, N. J. Smith, R. Kern, M. Picus, S. Hoyer, M. H. van Kerkwijk, M. Brett, A. Haldane, J. F. Del Río, M. Wiebe, P. Peterson, P. Gérard-Marchant, K. Sheppard, T. Reddy, W. Weckesser, H. Abbasi, C. Gohlke, and T. E. Oliphant. Array programming with NumPy. *Nature*, 585(7825):357–362, 2020.

[98] A. D. Pelton, S. A. Decterov, Gunnar Eriksson, and Y. Dessureault. The modified quasichemical model I - binary solutions. *Metall Mater Trans B*, 31:651–659, 2000.

[99] A. D. Pelton and P. Chartrand. The modified quasi-chemical model: part II. multicomponent solutions. *Metall Mater Trans A*, 32:1355–1360, 2001.

[100] P. Chartrand and A. D. Pelton. The modified quasi-chemical model: part III. Two sublattices. *Metall Mater Trans A*, 32:1397–1407, 2001.

[101] A. D. Pelton, P. Chartrand, and Gunnar Eriksson. The modified quasi-chemical model: part IV. two-sublattice quadruplet approximation. *Metall Mater Trans A*, 32:1409–1416, 2001.

[102] B. Sundman and J. Ågren. The sublattice model. *Mat Res Soc Symp Proc*, 19:115–127, 1983.

[103] M. Hillert, B. Jansson, B. Sundman, and J. Ågren. A two-sublattice model for molten solutions with different tendency for ionization. *Metall Mater Trans A*, 16:261–266, 1985.

[104] B. Sundman. Modification of the two-sublattice model for liquids. *Calphad*, 15(2):109–119, 1991.

[105] R. Lück, U. Gerling, and B. Predel. Associate entropy paradox of the association model. *Z Metallkde*, 80(4):270–275, 1989.

[106] T. M. Besmann and K. E. Spear. Thermochemical modeling of oxide glasses. *J Am Ceram Soc*, 85(12):2887–2894, 2002.

[107] S. Khadhraoui, K. Hack, T. Jantzen, and H.-J. Odenthal. Study of the state of industrial P_2O_5 –containing slags relevant to steelmaking processes based on a new thermodynamic database developed for CaO–FeOx–P_2O_5–SiO_2–MnO–MgO–Al_2O_3 slags – part I: Ternary and lower order systems. *steel res int*, 90(8):1900085, 2019.

[108] A. D. Pelton. *Phase diagrams and thermodynamic modeling of solutions*. Elsevier, Amsterdam, Netherlands and Cambridge, MA, 2019.

[109] M. Poschmann, P. Bajpai, B. W. N. Fitzpatrick, and M. H. A. Piro. Recent developments for molten salt systems in thermochimica. *Calphad*, 75:102341, 2021.

[110] A. D. Pelton and Milton Blander. Thermodynamic analysis of ordered liquid solutions by a modified quasichemical approach - application to silicate slags. *Metall Mater Trans B*, 17:805–815, 1986.

[111] M. J. D. Powell. A hybrid method for nonlinear equations. In P. Rabinowitz, editor, *Numerical methods for nonlinear algebraic equations*. Gordon and Breach Science Publishers, London, New York, Paris, 1970.

[112] L. S. Darken and W. Gurry. The system iron-oxygen. I. the wüstite field and related equilibria. *J Am Chem Soc*, 67(8):1398–1412, 1945.

[113] L. S. Darken and W. Gurry. The system iron-oxygen. II. equilibrium and thermodynamics of liquid oxide and other phases. *J Am Chem Soc*, 68(5):798–816, 1946.

[114] M. Timucin and A. E. Morris. Phase equilibria and thermodynamic studies in the system $CaO-FeO-Fe_2O_3-SiO_2$. *Metall Trans*, 1:3193–3201, 1970.

[115] E. Schürmann, K.-H. Obst, L. Fiege, and H.-P. Kaiser. Effect of bottom stirring and post stirring on the oxygen distribution between metal and slag at the end of the LD process. *Steel Res*, 56(8):425–431, 1985.

[116] G. Ottonello, R. Moretti, L. Marini, and M. V. Zuccolini. Oxidation state of iron in silicate glasses and melts: a thermochemical model. *Chem Geol*, 174:157–179, 2001.

[117] J. M. Park. Iron redox equilibria in BOF slag equilibrated with ambient air. *Steel Res*, 73(2):39–43, 2002.

[118] H. Kimura, S. Endo, K. Yajima, and F. Tsukihashi. Effect of oxygen partial pressure on liquidus for the CaO–SiO_2–FeOx system at 1573 K. *ISIJ Int*, 44(12):2040–2045, 2004.

[119] H. Kimura, T. Ogawa, M. Kakiki, A. Matsumoto, and F. Tsukihashi. Effect of Al_2O_3 and MgO additions on liquidus for the CaO-SiO_2-FeOx system at 1573 K. *ISIJ Int*, 45(4):506–512, 2005.

[120] S. Nikolic, P. C. Hayes, and E. Jak. Phase equilibria in ferrous calcium silicate slags: Part I. intermediate oxygen partial pressures in the temperature range 1200 °C to 1350 °C. *Metall Mater Trans B*, 39(2):179–188, 2008.

[121] S. Wright and L. Zhang. The influence of $Fe2^{+}/Fe3^{+}$ ration on the viscosity of iron silicate slags. *VII International Conference on Molten Slags Fluxes and Salts; South African Institute of Mining and Metallurgy: Cape Town, South Africa*, pages 231–236, 2004.

[122] G. Eriksson, P. Wu, M. Blander, and A. D. Pelton. Critical evaluation and optimization of the thermodynamic properties and phase diagrams of the MnO–SiO_2 and CaO–SiO_2 systems. *Can Metall Q*, 33(1):13–21, 1994.

[123] S. A. Decterov, In-Ho Jung, and A. D. Pelton. Thermodynamic modeling of the FeO–Fe_2O_3–MgO–SiO_2 system. *J Am Ceram Soc*, 85(12):2903–2910, 2002.

[124] I.-H. Jung, S. A. Decterov, and A. D. Pelton. Critical thermodynamic evaluation and optimization of the Fe–Mg–O system. *J Phys Chem Solids*, 65(10):1683–1695, 2004.

[125] Y-B Kang, S. A. Decterov, A. D. Pelton, and H.-G. Lee. Critical thermodynamic evaluation and optimization of the CaO–MnO–SiO_2 and CaO–MnO–Al_2O_3 systems. *ISIJ Int*, 44(6):965–974, 2004.

[126] I.-H. Jung, S. A. Decterov, and A. D. Pelton. Critical thermodynamic evaluation and optimization of the CaO–MgO-SiO_2 system. *J Eur Ceram Soc*, 25(4):313–333, 2005.

[127] I.-H. Jung, S. A. Decterov, and A. D. Pelton. Critical thermodynamic evaluation and optimization of the FeO-Fe_2O_3-MgO-SiO_2 system. *Metall Mater Trans B*, 35:877–889, 2004.

[128] E. Jak, P. Hayes, A. Pelton, and S. Decterov. Thermodynamic optimisation of the FeO–Fe_2O_3–SiO_2 (Fe–O–Si) system with FactSage. *Int J Mat Res*, 98(9):847–854, 2007.

[129] S. K. Panda and I.-H. Jung. Critical evaluation and thermodynamic modeling of the Mg-Mn-O (MgO-MnO-MnO_2) system. *J Am Ceram Soc*, 97(10):3328–3340, 2014.

[130] S. K. Panda, Z. Cao, and I.-H. Jung. Critical evaluation and thermodynamic modeling of the MgO-MnO-Mn_2O_3-SiO_2 system. *J Am Ceram Soc*, 98(9):2921–2930, 2015.

[131] T. Hidayat, D. Shishin, E. Jak, and S. A. Decterov. Thermodynamic reevaluation of the Fe–O system. *Calphad*, 48:131–144, 2015.

[132] T. Hidayat, D. Shishin, S. A. Decterov, and E. Jak. Thermodynamic optimization of the Ca-Fe-O system. *Metall Mater Trans B*, 47(1):256–281, 2016.

[133] T. Hidayat, D. Shishin, S. A. Decterov, and E. Jak. Critical thermodynamic re-evaluation and re-optimization of the CaO–FeO–Fe_2O_3–SiO_2 system. *Calphad*, 56:58–71, 2017.

[134] T. Hidayat, D. Shishin, S. A. Decterov, and E. Jak. Experimental study and thermodynamic re-optimization of the FeO-Fe_2O_3-SiO_2 system. *J Phase Equilib Diffus*, 38(4):477–492, 2017.

[135] Y.-B. Kang and I.-H. Jung. Critical evaluations and thermodynamic optimizations of the MnO-Mn_2O_3-SiO_2 and FeO-Fe_2O_3-MnO-Mn_2O_3-SiO_2 systems. *Metall Mater Trans B*, 48(3):1721–1735, 2017.

[136] S. K. Panda. *Coupled experimental and thermodynamic modeling of Al_2O_3-CaO-FeO-Fe_2O_3-MgO-MnO-Mn_2O_3-SiO_2-Ti_2O_3-TiO_2 system.* PhD thesis, McGill University, Montreal, Quebec, Canada, 2019.

[137] G. Trömel, Klaus Koch, W. Fix, and N. Großkurth. Der Einfluß des Magnesiumoxyds auf die Gleichgewichte im System Fe–CaO–FeOn–SiO_2 und auf die Schwefelverteilung bei 1600 °C. *Archiv für Eisenhüttenwesen*, 40(12):969–978, 1969.

[138] E. Görl, R. Klages, R. Scheel, and G. Trömel. Gleichgewichte zwischen flüssigem Eisen und gesättigten Schlacken des Systems CaO–FeO–MnO–SiO_2 bei 1600 °C unter Berücksichtigung der Schwefelverteilung. *Archiv für Eisenhüttenwesen*, 40(12):959–967, 1969.

[139] P. Wu, G. Eriksson, A. D. Pelton, and M. Blander. Prediction of the thermodynamic properties and phase diagrams of silicate systems - evaluation of the FeO-MgO-SiO_2 system. *ISIJ Int*, 33(1):26–35, 1993.

[140] P. Wu, G. Eriksson, and A. D. Pelton. Critical evaluation and optimization of the thermodynamic properties and phase diagrams of the CaO–FeO, CaO–MgO, CaO–MnO, FeO–MgO, FeO–MnO, and MgO–MnO systems. *J Am Ceram Soc*, 76(8):2065–2075, 1993.

[141] S. Khadhraoui. *A Contribution to Modeling and Control of Dephosphorization in the Oxygen Steelmaking Process*. PhD thesis Universität Duisburg-Essen, Germany, 2021.

[142] M. Hillert. *Phase equilibria, phase diagrams and phase transformations: Their thermodynamic basis*. Cambridge University Press, Cambridge and New York, 2nd edition, 2008.

[143] M. Hillert. Diffusion and interface control of reactions in alloys. *Metall Mater Trans A*, 6:5–19, 1975.

[144] J. Svoboda, E. Gamsjäger, F.D Fischer, and P. Fratzl. Application of the thermodynamic extremal principle to the diffusional phase transformations. *Acta Mater*, 52(4):959–967, 2004.

[145] E. Gamsjäger. A concise derivation of the contact conditions at a migrating sharp interface. *Philos Mag Lett*, 88(5):363–369, 2008.

[146] F. D. Fischer, J. Svoboda, and H. Petryk. Thermodynamic extremal principles for irreversible processes in materials science. *Acta Mater*, 67:1–20, 2014.

[147] D. Kondepudi. *Introduction to modern thermodynamics*. Wiley, Chichester, 2008.

[148] S. R. deGroot and P. Mazur. *Non-equilibrium thermodynamics*. Dover Publications, New York, 1984.

[149] R. W. Balluffi, S. M. Allen, and W. C. Carter. *Kinetics of Materials*. John Wiley & Sons, Hoboken, New Jersey, 2005.

[150] Y. Liang. Multicomponent diffusion in molten silicates: Theory, experiments, and geological applications. *Rev Mineral Geochem*, 72(1):409–446, 2010.

[151] D. M. Ogris and E. Gamsjäger. Numerical treatment of oxide particle dissolution in multicomponent slags with local gibbs energy minimization. *steel res int*, 93:2200056, 2022.

[152] T. H. Cohen and M. E. Glicksman. Multicomponent diffusion: implementation of the square-root diffusivity method via the Profiler computer program. *Modell Simul Mater Sci Eng*, 3:585–596, 1995.

[153] M. E. Glicksman and A. O. Lupulescu. Dynamics of multicomponent diffusion with zero flux planes. *Acta Materialia*, 51(4):1181–1193, 2003.

[154] H. Trenkler and W. Krieger. *Gmellin-Durrer Metallurgie des Eisens. Band 5. Theorie der Stahlerzeugung 1.* Springer, Berlin, 1978.

[155] L. Ratke and P. W. Vorhees. *Growth and Coarsening: Ostwald Ripening in Material Processing.* Springer, Berlin, Heidelberg, New York, 2002.

[156] R. C. Kerr. Convective crystal dissolution. *Contrib Mineral Petrol*, 121:237–246, 1995.

[157] D. Martin and R. Nokes. A fluid-dynamical study of crystal settling in convecting magmas. *J Petrol*, 30(6):1471–1500, 1989.

[158] Y. Zhang and Z. Xu. Kinetics of convective crystal dissolution and melting, with applications to methane hydrate dissolution and dissociation in seawater. *Earth Planet Sci Lett*, 213(1-2):133–148, 2003.

[159] H. Chen and S. van der Zwaag. Application of the cyclic phase transformation concept for investigating growth kinetics of solid-state partitioning phase transformations. *Comput. Mater. Sci.*, 49(4):801–813, 2010.

[160] H. Chen, B. Appolaire, and S. van der Zwaag. Application of cyclic partial phase transformations for identifying kinetic transitions during solid-state phase transformations: Experiments and modeling. *Acta Mater.*, 59(17):6751–6760, 2011.

[161] H. Chen, E. Gamsjäger, S. Schider, H. Khanbareh, and S. van der Zwaag. In situ observation of austenite–ferrite interface migration in a lean Mn steel during cyclic partial phase transformations. *Acta Mater.*, 61(7):2414–2424, 2013.

[162] E. Gamsjäger, H. Chen, and S. van der Zwaag. Application of the cyclic phase transformation concept for determining the effective austenite/ferrite interface mobility. *Comput. Mater. Sci.*, 83:92–100, 2014.

[163] D. M. Ogris, V. Kircher, and E. Gamsjäger. Cyclic solid-liquid phase transformations in the CaO-SiO_2 system - experiments and modelling. *Metall Mater Trans B*, 54:1555–1564, 2023.

[164] T. Deng and D. Sichen. Study of lime dissolution under forced convection. *Metall Mater Trans B*, 43(3):578–586, 2012.

[165] T. Deng, B. Glaser, and D. Sichen. Experimental design for the mechanism study of lime dissolution in liquid slag. *steel res int*, 83(3):259–268, 2012.

[166] S.-y. Kitamura. Dissolution behavior of lime into steelmaking slag. *ISIJ Int*, 57(10):1670–1676, 2017.

[167] Z. S. Li, M. Whitwood, S. Millman, and J. van Boggelen. Dissolution of lime in BOS slag: from laboratory experiment to industrial converter. *Ironmaking Steelmaking*, 41(2):112–120, 2014.

[168] J. Martinsson, B. Glaser, and D. Sichen. Lime dissolution in foaming BOF slag. *Metall Mater Trans B*, 49(6):3164–3170, 2018.

[169] Y. Liang and A. M. Davis. Energetics of multicomponent diffusion in molten CaO-Al_2O_3-SiO_2. *Geochim Cosmochim Acta*, 66(4):635–646, 2002.

[170] A. Lee. VirtualDub, version 1.9.10.

[171] J. Rüdig. https://ruedig.de/tmp/messprogramm.htm. Accessed 25 Jun. 2023.

[172] Y. Liang, Frank M. Richter, and E. Bruce Watson. Diffusion in silicate melts: II. multicomponent diffusion in CaO-Al_2O_3-SiO_2 at 1500°C and 1 GPa. *Geochim Cosmochim Acta*, 60(24):5021–5035, 1996.

[173] G. Eriksson and A. D. Pelton. Critical evaluation and optimization of the thermodynamic properties and phase diagrams of the CaO-Al_2O_3 , Al_2O_3-SiO_2, and CaO-Al_2O_3-SiO_2 systems. *Metall Trans B*, 24:807–816, 1993.

[174] P. Courtial and D. B. Dingwell. Nonlinear composition dependence of molar volume of melts in the CaO-Al_2O_3-SiO_2 system. *Geochim Cosmochim Acta*, 59(18):3685–3695, 1995.

[175] K. Tang, C. van der Eijk, S. Gouttebroze, Q. Du, J. Safarian, and G. Tranell. Rheological properties of Al_2O_3–CaO–SiO_2 slags. *Calphad*, 77:102421, 2022.

[176] Y. Kang and K. Morita. Thermal conductivity of the CaO-Al_2O_3-SiO_2 system. *ISIJ Int*, 46(3):420–426, 2006.

[177] S. Chandrasekhar. *Hydrodynamic and Hydromagnetic Stability*. Dover Publications, New York, 1981.

[178] R. B. Bird and W. E. Stewart. *Transport Phenomena*. Wiley, New York, 2nd edition, 2001.

[179] M. Allibert, H. Gaye, J. Geiseler, D. Janke, B. J. Keene, D. Kirner, M. Kowalski, J. Lehmann, K. C. Mills, D. Neuschütz, R. Parra, C. Saint-Jours, P. J. Spencer, M. Susa, M. Tmar, and E. Woermann. *Slag Atlas*. Verlag Stahleisen, Düsseldorf, 2nd edition, 1995.